

# **Dissertation**

submitted to the

Combined Faculty of Natural Sciences and Mathematics  
at the Ruprecht-Karls University of Heidelberg, Germany

for the degree of

Doctor of Natural Sciences (Dr. rer. nat.)

Presented by

**Dipl.-Chem. Christof Christophis**

**Born in Gießen, Germany**

Oral examination: July 20<sup>th</sup>, 2011



# **Quantification of cell adhesion strength on artificial surfaces with a microfluidic shear force device**

This dissertation was carried out at the  
**Department of Applied Physical Chemistry**  
**University of Heidelberg**

Referees:

Prof. Dr. Michael Grunze

Prof. Dr. Joachim P. Spatz



## Abstract

Adhesion strength is a measure to determine the interaction between cells and their environment. Numerous types of devices and coatings are developed in order to meet medical and non medical issues and surface properties can be tuned in order to evoke specific cell response.

In this work various properties of solid surfaces were investigated towards their impact on adhesion process and adhesion strength of mammalian cells, which both give information on the cell interaction with the substrate. Therefore a sophisticated assay to observe cell adhesion and measure cell adhesion strength on artificial surfaces was developed. Its capability to measure cell adhesion strength in the order of five magnitudes with a high reliability and quantitative output was applied to synthetic surfaces with different degree of hydration, anisotropic topography, bioactivity and different polarizations.

Investigation of fibroblast adhesion on ethylene glycol self assembled monolayers showed that cell adhesion strength is reduced by increasing degree of hydration. At the same time it was found that cell adhesion strength was independent of cell spreading area, in particular when a certain spreading size was reached. This finding may strengthen the zipper detachment mechanism by which the cell detachment occurs after distinct bonds are broken. Another study on hydrogel like polysaccharides confirmed the inability of fibroblasts to attach to hydrated surfaces. At the same time it was found that hematopoietic progenitor cells expressing CD44 receptors overcome the inertness and attach to the coating by shear force induction through a hydrodynamic flow. This finding may explain the fact that the presence of hyaluronan is a prerequisite in the stem cell homing and engraftment process into the bone marrow.

Besides receptor ligand interactions more basic surface polarity effects were studied, which have been reported to have a minor impact towards cell adhesion. Here it was shown by investigation of fibroblast adhesion on periodically poled ferroelectric lithium tantalite crystals, that the gradient between two opposite polarities can be sensed by cells but not the polarity itself. The cells do not distinguish the overall polarity of a surface, but avoid placing the nucleus in proximity to the sharp borders in between to inverse polarities as the cells start to spread. Even though this astonishing reaction is unexpected it is not contradictive to the absence of polarity sensing because sensing of a polarity gradient is different from a distinct polarization spread over a large area.

Instead of a gradient, anisotropic surface properties can be achieved by directional surface texture. Anisotropically textured poly(*p*-xylylene) surfaces, which consist of dense packed tilted nanorods, revealed a force directional dependence of fibroblast cell adhesion strength. The hydrodynamic shear force applied with the direction of nanorod tilting revealed a reduced cell adhesion strength compared to force application perpendicular and

against the tilting. This finding could be explained by a model which accounts for cell filopodia attaching between nanorods of the surface.

In order to prove the filopodia attachment theory more sophisticated imaging, which reveals ultrastructural components, was needed. Therefore, cell preparation protocols were established with special attention to preserve cellular structure to image via X-ray holography under ultrahigh vacuum conditions. The imaging project was conducted in a consortium of researchers and first successful imaging was demonstrated.

## Kurzfassung

Zellhaftstärke ist ein Maß um die Wechselwirkungen zwischen Zellen und ihrer Umgebung zu bestimmen. Unzählige Geräte und Beschichtungen werden für medizinische und nichtmedizinische Zwecke entwickelt und Oberflächeneigenschaften können gezielt modifiziert werden, um spezifische Reaktionen von Zellen hervorzurufen.

In der vorliegenden Arbeit werden unterschiedliche Oberflächeneigenschaften bezüglich ihres Einflusses auf den Adhäsionsprozess und die Haftstärke von Säugetierzellen untersucht. Beide Messgrößen geben Aufschluss auf die Wechselwirkung zwischen Zelle und Oberfläche. Zur Durchführung der Messungen musste ein technisch ausgefeilter mikrofluidischer Aufbau entwickelt werden. Die Realisierung des Systems ermöglichte es Zellhaftstärke in einem Bereich von fünf Größenordnungen mit hoher Verlässlichkeit zu bestimmen und wurde anschließend auf synthetische Oberflächen mit unterschiedlicher Hydratation, anisotropischer Topographie, Bioaktivität und Polarisierung angewendet.

Untersuchungen von Fibroblasten auf selbst organisierten Monolagen zeigten, dass die Zellhaftstärke mit steigender Hydratation abnimmt. Dabei konnte auch gezeigt werden, dass die Zelladhäsionsstärke oberhalb einer bestimmten Zellausbreitung unabhängig von der Ausbreitungsfläche ist. Dieses Resultat stellt ein weiteres Indiz zum Reißverschluss Abrissmechanismus dar, welcher besagt dass der komplette Zellabriss stattfindet, nachdem bestimmte Einzelbindungen gebrochen wurden. Eine andere Studie wurde auf hydrogelähnlichen Polysacchariden durchgeführt und bestätigt das fehlende Haftvermögen von Fibroblasten auf hydratisierten Oberflächen. Im Gegensatz dazu waren CD44 exprimierende hematopoetische Vorläuferzellen aus Nabelschnurblut dazu befähigt unter Einwirkung eines hydrodynamischen Flusses an das Polysaccharid Hyaluron zu binden. Diese Erkenntnis könnte erklären warum die Anwesenheit von Hyaluron im Knochenmark eine Grundnotwendigkeit für das *Homing* von Stammzellen darstellt.

Abgesehen von spezifischen Rezeptor-Ligand Wechselwirkungen wurden auch die Auswirkung grundlegender Oberflächeneigenschaften wie Polarität auf die Zelladhäsion hin untersucht. In der vorgestellten Studie wurde die Zelladhäsion auf periodisch abwechselnd gepolten ferroelektrischen Lithium-Tantalat Kristallen bestimmt. Hierbei zeigte sich, dass Fibroblasten nicht auf die positive oder negative Polarität selbst reagieren wohl aber auf den Gradienten, der sich auf der Grenze zwischen zwei entgegengesetzt polarisierten Domänen bildet. Sobald der Zell-Ausbreitungsprozess beginnt vermeiden es die Zellen sich so zu positionieren, dass der Zellkern auf den Grenzen liegt. Auch wenn diese Beobachtung unerwartet scheint, so ist sie dennoch nicht widersprüchlich zur fehlenden Reaktion auf durchgehend gleich polarisierten Oberflächen, weil im Falle eines Polarisationsgradienten die Zellen nur auf eine Änderung der Oberflächeneigenschaften reagieren müssen.

Anstelle von Polarisationsgradienten können anisotrope Oberflächeneigenschaften auch durch gerichtete Oberflächenstrukturierung erhalten werden. Hierfür wurden Nanostäbchen aus poly(*p*-xylylene) verwendet, welche dicht gepackt in einem definierten Kippwinkel auf der Oberfläche stehen. Es konnte gezeigt werden, dass Fibroblasten eine richtungsabhängige Haftstärke auf diesen Oberflächen aufweisen. Wurde die hydrodynamische Scherkraft in Kipprichtung der Stäbe angelegt, resultierte eine vergleichsweise geringere Haftstärke als im Falle von hydrodynamischer Scherkraft gegen und quer zur Kipprichtung der Stäbe. Dieses Resultat konnte durch ein Modell erklärt werden, welches ein Eindringen der Zellfortsätze in die Lücken zwischen den Stäben für die Unterschiede verantwortlich macht.

Da mit den kommerziellen Methoden nur im Ansatz gezeigt werden konnte, dass die Fortsätze zwischen die Stäbe penetrieren, wurde eine Technik benötigt welche ultrastrukturelle Komponenten abbilden kann. Zellproben, welche unter speziell entwickelten Präparationsmethoden hergestellt wurden, konnten mittels Röntgenstrahlen Holography unter Ultrahochvakuum Bedingungen gemessen werden. Dieses Projekt würde von einem Zusammenschuss von Forschern realisiert und erste erfolgreiche Bilddarstellung von Zellen wurde gezeigt.

# Contents

Abstract.....	V
Kurzfassung.....	VII
Contents.....	IX
1 Introduction .....	1
2 Background.....	3
2.1 Cell Adhesion .....	3
2.2 Cell rolling.....	4
2.3 Surface properties relevant for cell adhesion.....	5
2.3.1 Influence of hydration .....	5
2.3.2 Influence of bioactivity – the receptor-ligand interactions.....	7
2.3.3 Influence of topography.....	8
2.3.4 Influence of charge and polarity.....	10
2.4 High resolution imaging for cellular adhesion .....	10
2.5 Measurement of cell adhesion strength.....	12
2.5.1 Centrifugal force assays.....	12
2.5.2 Micromanipulation based detachment techniques.....	13
2.5.3 Hydrodynamic shear force assays for cell detachment .....	14
3 Materials and Methods .....	19
3.1 Preparation techniques .....	19
3.1.1 Preparation of self assembled monolayers on gold .....	19
3.1.2 Protein adsorption assay .....	20
3.1.3 Preparation of nanotextured PPX-films on glass.....	20
3.1.4 Preparation of Polysaccharides on glass.....	21
3.1.5 Preparation of single poled and periodically poled LiTaO <sub>3</sub> .....	23
3.1.6 Cell culture .....	23
3.1.7 Sample preparation for ultrahigh vacuum applications.....	24
3.2 Analytical techniques.....	25
3.2.1 Contact angle goniometry.....	25
3.2.2 Spectral ellipsometry .....	27
3.2.3 X-ray photoelectron spectroscopy .....	29

3.2.4	Light Microscopy .....	30
3.2.5	Scanning electron microscopy .....	32
4	Microfluidic shear force setup.....	35
4.1	Demands on the setup.....	35
4.2	Microfluidic device.....	36
4.2.1	The parallel plate flow channel .....	37
4.2.2	Flow control .....	38
4.3	Microfluidic shear force assay.....	40
4.3.1	Preparation of the channel system.....	41
4.3.2	Conduction of the experiment.....	42
4.3.3	Evaluation of the experiment .....	43
4.4	Performance of the shear force assay .....	46
4.4.1	Flow characterization .....	46
4.4.2	Polystyrene microspheres on dodecanethiol SAMs.....	47
4.4.3	Streptavidin microspheres on biotinylated SAMs.....	48
4.5	Parameter optimization for adherent mammalian cells .....	51
4.5.1	Harvesting protocol .....	51
4.5.2	Influence of in channel incubation time on cell adhesion strength .....	53
4.5.3	Influence of detachment assay time on cell adhesion strength .....	54
5	Cell adhesion strength on hydrated ethylene glycol terminated SAMs .....	57
5.1	Surface characterization of EG-SAMs .....	57
5.2	Cell adhesion strength decreases with increasing OEG chain length.....	58
5.3	Correlation of cell morphology and adhesion strength .....	60
5.4	Discussion.....	61
6	Cell adhesion strength on Polysaccharide Coatings.....	63
6.1	Characterization of hyaluronan and alginate thin films.....	63
6.2	Adhesion of fibroblasts on polysaccharides HA and AA.....	64
6.3	Adhesion of leukemia cells to polysaccharides HA and AA.....	65
6.4	Flow mediated binding of KG-1a cells to hyaluronan .....	67
6.5	CD44 dependent binding of leukemic cells to hyaluronan.....	69
6.6	Binding of hematopoietic progenitor cells to hyaluronan .....	71

6.7	Discussion.....	73
7	Cell adhesion on polarized LiTaO <sub>3</sub> substrates.....	75
7.1	Characterization of poled LiTaO <sub>3</sub> substrates.....	75
7.2	Cell adhesion on (+) and (-) and periodically poled LiTaO <sub>3</sub> .....	76
7.3	Cell response to polarization of periodically poled LiTaO <sub>3</sub> .....	78
7.4	Discussion.....	82
8	Cell adhesion strength on nanotextured PPX-films.....	83
8.1	Characterization of nanotextured PPX-films.....	83
8.2	Microsphere adhesion strength measurements on nanotextured PPX-films.....	84
8.3	Cell adhesion strength measurements on nanotextured PPX-films.....	85
8.4	Cell adhesion and morphology on nanotextured PPX-films.....	87
8.5	Discussion.....	89
9	Visualization of cells using high resolution imaging.....	91
9.1	Preparation of adherent cells for X-ray holography studies.....	91
9.2	Digital in-line holography using pinholes.....	92
9.3	Digital in-line holography using zone plates.....	93
9.4	Discussion.....	95
10	Summary and Outlook.....	97
11	Appendix.....	101
11.1	List of Parameters.....	101
11.2	Name Abbreviations.....	102
11.3	Chemicals & Reagents.....	103
11.4	Materials.....	105
11.5	Bibliography.....	106
11.6	Financial Support.....	125
11.7	List of publications related to this work.....	126



# 1 Introduction

Adhesion is the essential step for a cell to connect to a surface or to other cells in order to maintain a multicellular structure. Cell adhesion can regulate the cells shape, growth, differentiation, motility or survival. The surface is one important stimulus for its control. Structural, mechanical, chemical and polarity properties [1] have been suggested to influence adhesion to artificial surfaces. The adhesion bond is established via adhesion molecules such as integrins, cadherins or selectins. The adhesion sites are involved in signal transduction and thus carry external stimuli which trigger cellular processes.

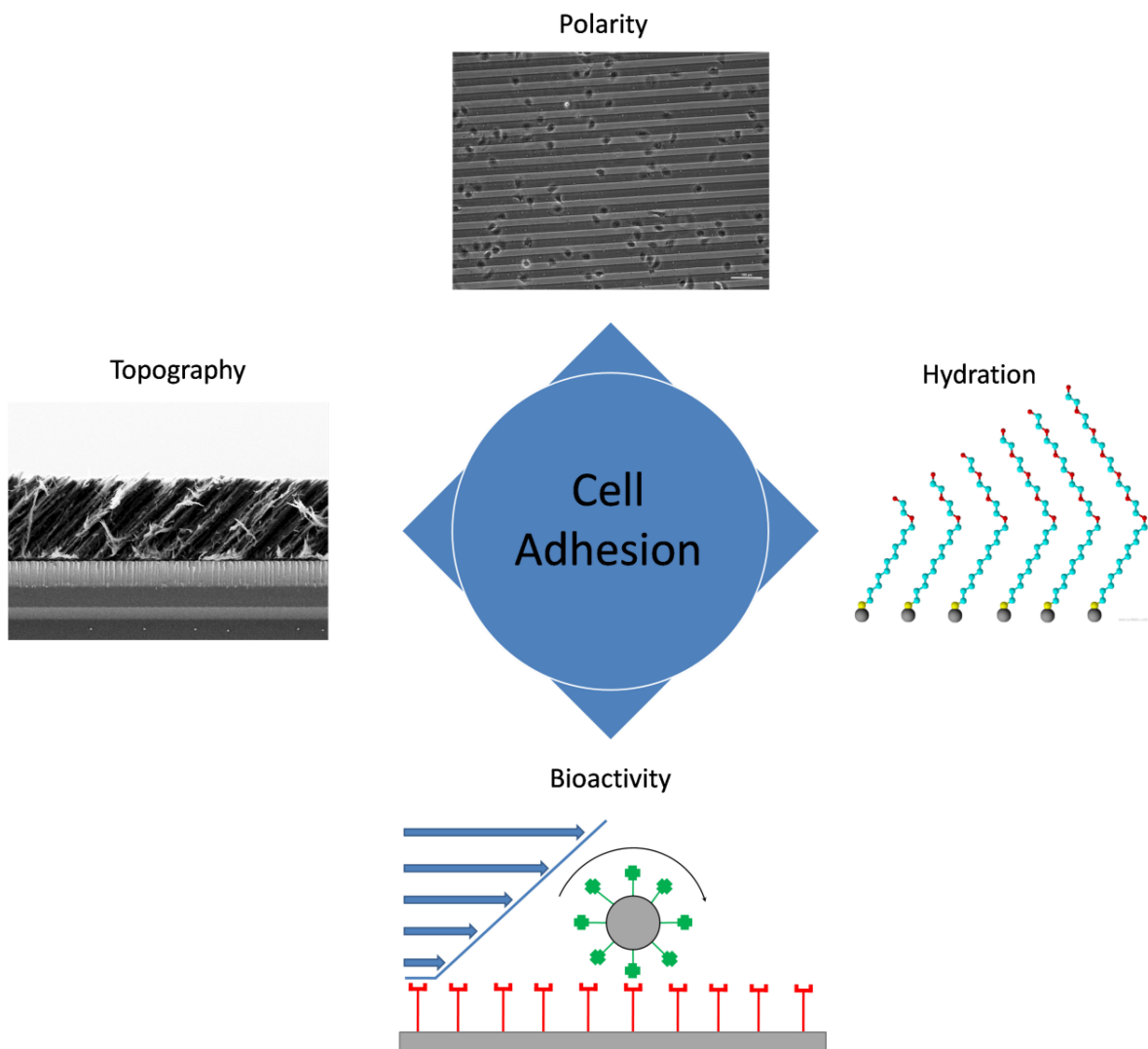


Figure 1: Surface properties which trigger cell adhesion.

For adherent cells especially mechanical properties of the surface have a major relevance. That is due to use of focal contacts to probe the biochemical and mechanical properties of their environment and to regulate the organization of the cytoskeleton. The stiffness of an elastic substrate effects focal contact formation, cell elasticity, cell migration and cell

differentiation [2 - 5]. Also the absolute contact area and adhesion site distribution is important for cell adhesion as it can stimulate differentiation [6], controls the formation of focal contacts [7; 8] and therefore the control of cell life and death [9].

The above mentioned findings encourage scientists to investigate cell adhesion and its control by surface stimuli using a wide variety of approaches. The quantification of interaction between the cell and a surface are achieved by probing the system with forces to disturb the system equilibrium and measure the reaction.

The aim of the work is to develop a versatile and reliable method based on the microfluidic concept to apply hydrodynamic shear forces, which lead to the breaking of adhesion bonds between the cell and surface. This way the adhesion strength of mammalian cells on a variety of different surfaces can be determined quantitatively. This thesis focuses on the impact of four surface property aspects namely topography, polarity, hydration and bioactivity towards cell adhesion (Figure 1).

## 2 Background

### 2.1 Cell Adhesion

In the connective tissue of mammals, cell adhesion is established via the extracellular matrix (ECM) [10]. The ECM consists mainly of glycoproteins and binds via the RGD sequence of the protein fibronectin to the integrins of the cell [11]. Integrins are transmembrane proteins, which bind to the actin microfilament network of the cytoskeleton (Figure 2) via many different proteins, including paxillin [12]. Furthermore, the cytoskeleton is composed of a microtubule network and an intermediate filament network [13]. The cytoskeleton maintains the structural integrity of the cell. It determines the cell shape, controls organelle positioning and allows cell movement.

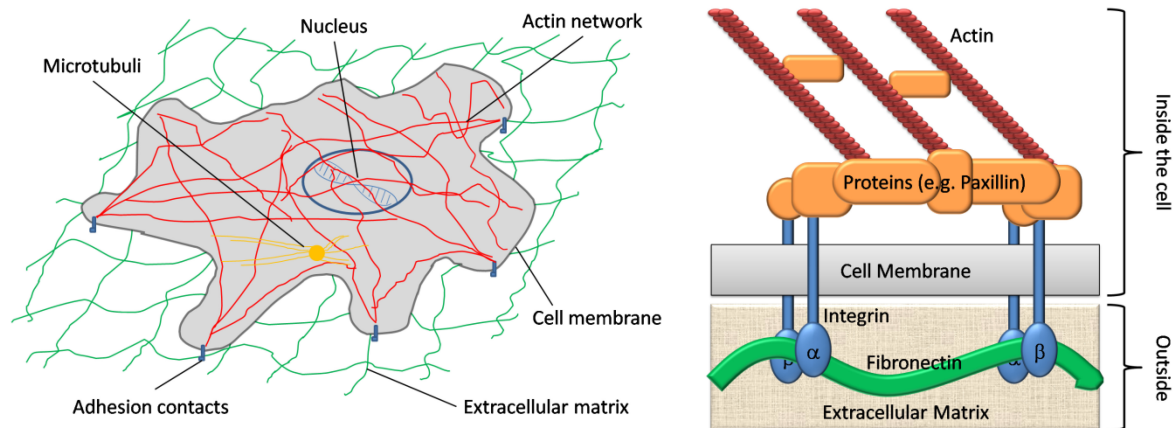


Figure 2: Left: Scheme of a cell displaying the main cytoskeleton and main components for cell adhesion. Right: For focal adhesion transmembrane integrins mediate the bond between the cytoskeleton and the ECM.

The cells strongest adhesion type is the focal contact. Focal adhesion contacts are prominent cell-matrix adhesion structures [14] and consist of large patches of transmembrane adhesion receptors from the integrin-family [15] which can reach lateral sizes of several micrometers. The connection to the cytoskeleton occurs often in the form of stress fibers. These are myosin driven, bundled actin filaments which allow force transmission between cells and the ECM through the focal contacts. Cells use focal contacts to probe biochemical and mechanical information about their environment and to regulate the organization of the cytoskeleton. The formation of focal adhesion contacts for a newly adhering cell takes time (Figure 3). First a weak hyaluronan mediated cell attachment takes place [16]. While the cell is spreading, focal complexes are formed within minutes and focal adhesions are established within hours [17]. The adhesion process takes longer if the cell has to build up its own ECM. Via the interaction of the cell with the ECM and its interaction with the surface, adhesion can regulate cell shape, growth, motility or cell life and death.

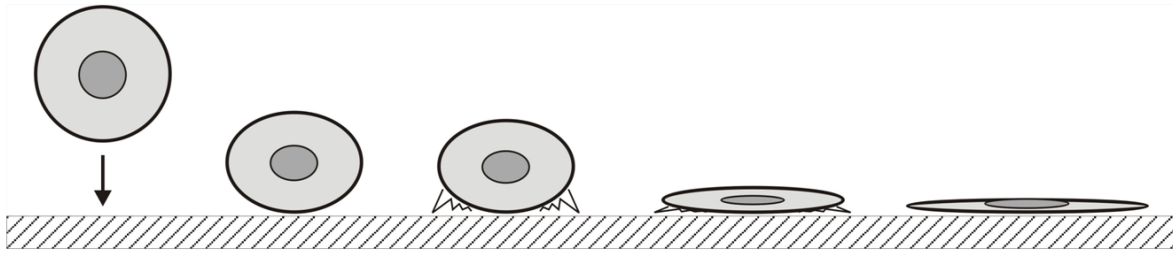


Figure 3: Mechanism of cell adhesion of adherent cells forming focal contacts. First the cell sinks down onto the surface and deforms. Then the cell spreads and first contact is established via hyaluronan. During flattening focal complexes and later focal adhesions are established.

Cell adhesion is not only important in connective tissue but also healing, growth and immune defense processes. For example blood cells have to escape from the blood stream via adhesion to the vessel wall to perform wound repair and to engage pathogens.

## 2.2 Cell rolling

Besides focal contacts there are other types of cell attachment strategies which allow weak to moderate adhesion. Cell rolling is such a type of adhesion. It is found in the blood circuit and is an optimal for reversible, dynamic binding strategy which allows mobile cells to escape from the blood stream by rolling and attachment on the vessel wall. These cells can then fulfill their metabolic tasks as e.g. inflammatory response and finally return to the blood flow.

The process of cell rolling is driven by the interaction of selectins with glycosylated ligands. Leukocytes expressing glycoprotein ligand 1 (PSGL1) [18] interact with the E- and P-selectins expressed by the inflammatory endothelial cells (Figure 4). Vice versa leukocytes express L-selectins to capture other leukocytes via PSGL1 inside a lymphoid organ. These interactions enable leukocytes to adhere to inflamed endothelium under conditions of blood flow because the binding occurs with exceptionally high on- and off-rates [19]. The binding of L-selectin and P-selectin requires shear stress [20; 21] to support adhesion and thus leukocytes detach when the flow is stopped. This phenomenon is related to the catch bond character of selectins [22]. The bond is strengthened as shear stress is applied. Besides that, shear stress also mediates the transport of selectins to the periphery of the cells. This brings the selectins closer to their ligands by the rolling motion of the cell which then allows to form new bonds before the old ones are broken [23].

Integrins also participate in rolling and mediate firm leukocyte adhesion. For instance lymphocytes can roll on immobilized vascular cell-adhesion molecule 1 by engaging their cell-surface ligand very late antigen 4 (VLA4;  $\alpha 4\beta 1$ -integrin) [24]. VLA4 mediates rapid adhesion alone [25] or in conjunction with P-selectin [26].

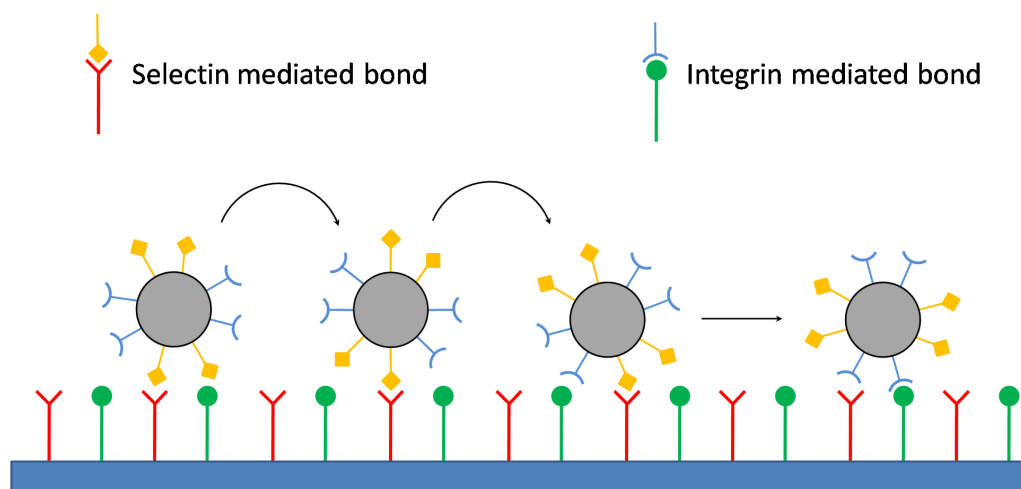


Figure 4: Mechanism of leukocyte cell rolling. Rolling is mediated by selectin based bonds, firm adhesion towards arrest by the following integrin mediated bond. Scheme is inspired by [27].

## 2.3 Surface properties relevant for cell adhesion

### 2.3.1 Influence of hydration

Surface hydration is found to be a prerequisite for a resistant surface to prevent protein and cell adhesion [28]. The mechanism is based on the hypothesis that water has to be displaced from the interface on a substrate so that glue proteins secreted by the cell may adsorb tightly and hence cell adhesion can take place.

The highly hydrated polymer polyethylene glycol (PEG) is one of the chemistries showing highest resistance towards biological matter but the material lacks long term stability. It has been used in the biomedical field [29; 30] and has been investigated towards its antifouling potential [31 - 35] for numerous years. The first systematic attempts to clarify the effects have been carried out on self assembled monolayers (SAMs) with varying number of the monomer ethylene glycol (EG) [36]. It was found that proteins do not adsorb on a surface if there is more than one EG unit presented on top of the surface. Recent studies confirmed this result for the adhesion of living marine algae spores [37].

It has been concluded by the Whitesides group that all hydrogen bridge bond acceptors promote non-adherent properties [38]. Furthermore it was shown in a steric repulsion model that protein adsorption would be energetically unfavorable for long EG chains [30]. The reason why also short EG chains prevent protein adsorption, even though the entropy is smaller compared to PEG [39], is due the high hydration energy. Performance of *ab initio* quantum mechanical and statistical calculations revealed that chains with three EG units can make multiple binding to a water molecule in different chain configurations [40; 41]. That is still true for EG chains with at least two units but not for a single ethylene glycol unit which has thus too low hydration energy to prevent protein adsorption. For short EG chains also the lateral packing density plays a crucial role as adsorption of

proteins for very high packing densities [42] which is counterintuitive. Monte Carlo simulations showed that at high packing densities water molecules barely penetrate the EG chains [43] which leads to decreased hydration.

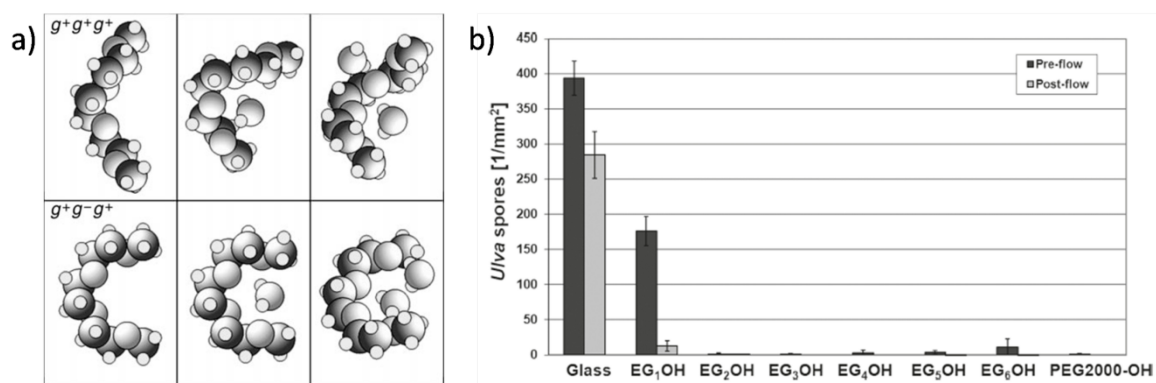


Figure 5: (a) Two conformational examples for a three units EG chain binding zero to two water molecules, taken and modified from [40]. (b) Attachment of algae spores *ulva* onto a series of SAMs with an increasing EG chain length. No spores adhere on SAMs with two EG units or more, taken from [37].

Other hydrogel polymers, e.g. hydrophilic polysaccharides have a high water binding affinity and are regarded as biological lubricants [44; 45]. Therefore they also have been considered as resistant towards biological material [46]. Morra *et al.* showed that coatings of polysaccharides hyaluronan (HA) and alginate (AA) resist the adhesion of fibroblasts *in vitro* (Figure 6) and *in vivo*. Also the adhesion of bacteria is reduced significantly [47,48]. Studies in our group showed protein resistance of HA, AA and pectinate (PA) and that adhesion of blood related leukemia cells is also inhibited [49]. Contrary marine organisms were able to settle on the polysaccharides, which has been attributed to the complexation of bivalent ions from solution by the film causing the hydrated film to collapse [49]. Also, the polysaccharide HA has been found to undergo receptor-ligand interactions with receptors expressed by cells from the blood system which will be described detailed in the second part of the following chapter.

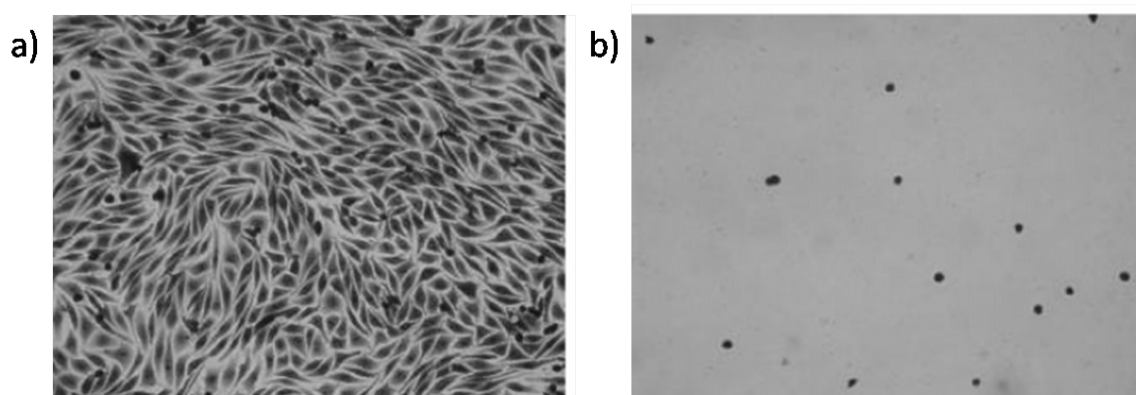


Figure 6: Microscopy images of L929 fibroblast adhesion experiments, after 72 h incubation on (a) polyethylenimine coated glass and (b) covalently coupled HA. Images taken from [46].

### 2.3.2 Influence of bioactivity – the receptor-ligand interactions

Bioactivity describes the reversible interaction of at least one protein with a ligand molecule due to their functional groups. One of the most prominent is the interplay of biotin (vitamin B7) with streptavidin. This receptor-ligand interaction is supposed to have the highest affinity constant and one of the strongest non covalent binding found in nature [50]. It is highly resistant towards environmental changes like pH, temperature and solvents. The streptavidin/biotin binding often serves as a model system for “proof of principle” concerning the potential role of protein ligand interactions. Numerous studies on the biotin/streptavidin complex e.g. using biomembrane force probe [5152] or atomic force microscopy [53; 54] have shown that the strength of receptor-ligand interactions depend on the conditions the bond breaking force is applied, so that the bond breaking energy is higher the faster the bond is stretched.

More direct implication towards biomedical applications are found for immobilized peptides containing the RGD-sequence as described in chapter 2.1 or in the receptor-ligand interaction of the receptor CD44 with the polysaccharide hyaluronan (HA). Hyaluronan is one of the major components found in the ECM. Beside its function as cellular material e.g. in osteoblasts, or endothelial cells, it is important in the regulation of self-renewal, maintenance and differentiation of hematopoietic progenitor cells (HPC) and leukemic stem cells in the stem cell niche [55; 56]. As discussed in the previous chapter (2.3.1) HA prevents adhesion of fibroblast cells, bacteria, algae and barnacle cyprids [47; 49]. HA is applied as a coating to prevent post surgery adhesion of microorganisms and inflammation as it has been shown in animal studies [46]. The binding of HA to hyaladherins is involved in many processes like wound healing, inflammation, growth of tumors and the proliferation of cells [46; 57 - 59]. Hyaladherins comprise many proteins capable of binding to HA, but CD44 remains the best investigated and pivotal binding partner [60 - 64]. CD44 is a multifunctional, ubiquitously expressed transmembrane protein [65 - 67]. The specific binding of CD44 to HA arises from a binding region – the link module – which is common for many hyaladherins [68]. It was found that lymphocyte rolling (chapter 2.2) is mediated by CD44 and its binding to HA which is present on the surface of endothelial cells [69; 70]. Inhibition of CD44 with monoclonal antibodies, soluble HA and hyaluronidase treatment of the substrate reduces adhesion and rolling [69]. However, specific CD44 functionalities as post-translational carbohydrate modifications of CD44 [68; 71] and other cell receptors like integrin VLA-4 [72] or size of the HA binding partner [73] may play a major role in the binding of CD44 to HA. The mechanism of CD44 mediated rolling on HA seems to be complementary to the well known function of integrins and selectins in lymphocyte homing [27; 74 - 77]. The homing of leukemic stem cells and their engraftment to their niche is CD44-dependent [78]. Even more, Avigdor *et al.* could show that CD44 and HA are essential for the homing and engraftment of HPCs into the bone marrow and spleen of NOD/SCID mice [79].

Despite those findings, which point out the high relevance of CD44/HA interaction towards the homing process (Figure 7), there is still a lack of quantitative data to describe the interaction of CD44 positive blood related cells with HA under flow.

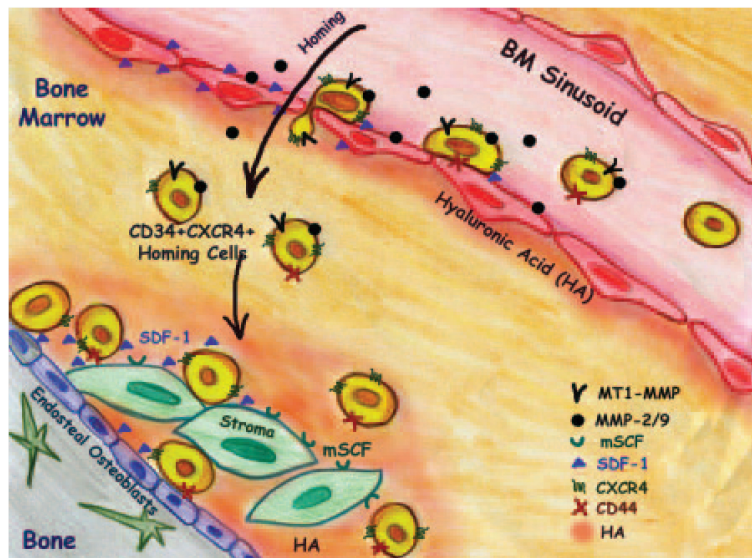


Figure 7: Sketch of stem cell homing to the endosteum. Recent reported key molecules involved in the process among the depicted are: LFA-1, VLA-4, VLA-5, selectins and their ligands [80].

### 2.3.3 Influence of topography

Surface topography is a widely used strategy in nature to control environmental interactions. The Lotus-Effect is the probably most prominent example. The hierarchical structure combined with wax secreted by the lotus leaf minimizes the contact of water to the surface (Figure 8A) mainly due to the air trapped in between the structural topography [81]. This results in a water repellent surface and has a self cleaning effect for the leaf (Figure 8B). As a consequence this principle has now been transferred to commercially available wall paints [82].

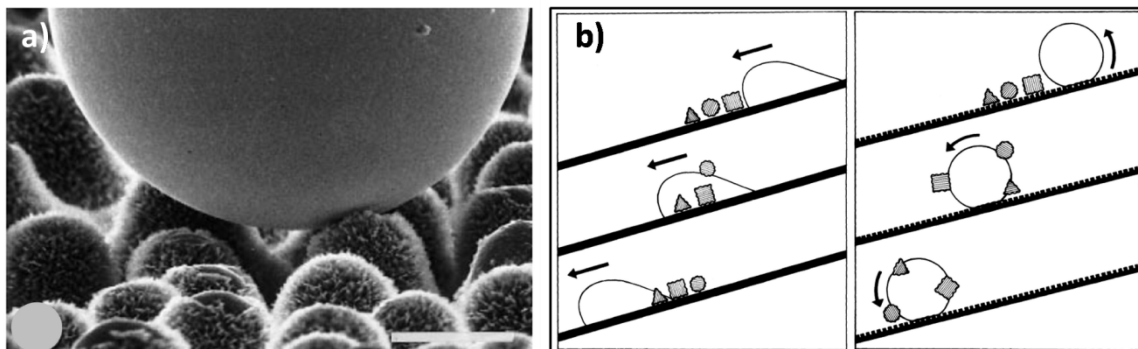


Figure 8: (a) Mercury drop on the rough epidermal surface of *Colocasia esculenta*. Air trapped between the features results in a water repellent surface (scalebar: 20μm). (b) Highly water repellent surfaces show a self cleaning effect. Both figures were taken from [81].

In the marine environment a lot of organisms found alternative strategies to defend themselves against the settlement of fouling organisms. Surface texture seem to be important as e.g. found for the ever clean shark skin [83] (Figure 9A,C). Its texture was first considered as an aerodynamically efficient coating in aviation [84] and was later applied successfully as a bio-inspired artificial coating (Figure 9B) against biofouling by marine organisms [85 - 87]. Despite the fact that attached organisms were sheared off easier from these structured elastomers also less organisms adhere. These outstanding properties of the textured coating was correlated with a nanoforce gradient in between the topographical features [88].

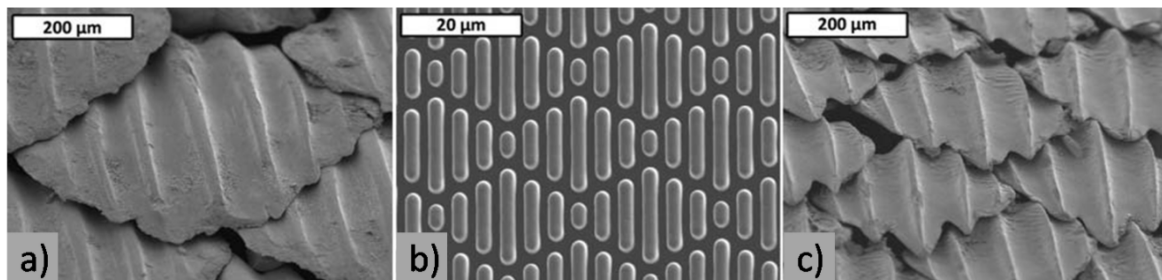


Figure 9: (a, c) The riblets of sharkskin scales from the spinner shark and the Galapagos shark. (b) Photolithography based elastomer structure Sharklet™. Figure was taken from [83].

Nature also provides topographies which have anisotropic textures. Butterfly wings for instance, allow water droplets to pin or to roll off from the surface in dependence of tilting direction [89] despite external gravity. Recently, anisotropically nanotextured poly(*p*-xylylene) surfaces (PPX) based on dense packed nanorods have been manufactured which are mimicking this effect [90] (Figure 10). The directional adhesion is believed to appear due to a ratchet mechanism justified by anisotropic friction which is caused by the tilted nanorods [91]. Directional dependence of surface friction for nano sized features has also been discussed for the walking mechanism of gecko [92], where control of toe attachment and detachment is crucial. Although efforts were taken to adapt gecko-inspired principles to medical applications as wound sealing [93] no studies have been performed to reveal the impact of anisotropic friction on nanotextured PPX-films towards the adhesion of cellular material.

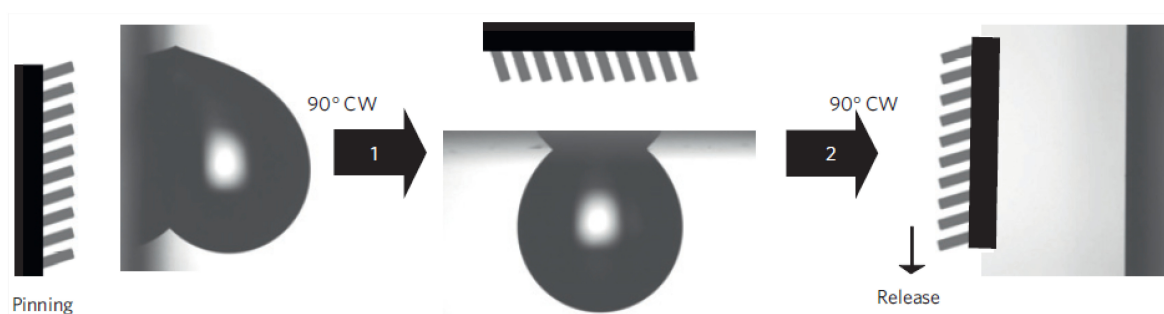


Figure 10: The pinning and release on nanotextured PPX-surfaces is dependent on the tilting of the substrate. If the nanorod tilting perpendicular to the gravity force the water droplet is pinned. If the nanorod tilting is in gravity direction the droplet is released. Figure was taken from [90].

### 2.3.4 Influence of charge and polarity

When a particle, cell or microorganism approaches a surface, the first interaction it will encounter will be electrostatic. The effect of surface charge towards adhesion of microorganisms is often discussed in the context of surface energy because tuning of the surface charge mostly changes chemical functionality and thus surface tension. In order to disentangle the two effects studies with two differently charged mixed COOH/CH<sub>3</sub> and OH/CH<sub>3</sub> terminated SAMs have been performed and attachment of *Ulva* zoospores was less on COOH/CH<sub>3</sub> at the same contact angle (surface energy) as on stronger positively charged OH/CH<sub>3</sub> SAM (Figure 11) [94]. The difference might be due to electrostatic repulsion of the terminal COOH groups but also a chemical response cannot be excluded. Studies by Ostuni *et al.* suggest that overall electrically neutral surfaces prevent the adsorption of proteins best [95]. In order to circumvent surface energy or chemical contributions towards cell adhesion, quasi-permanently positively or negatively charged chemically similar polytetrafluoroethylene electrets were investigated towards attachment of *Ulva* zoospores [96]. The *Ulva* zoospores have a negative zeta potential and spores settle less and weaker on negatively charged electrets (Figure 11), indicating electrostatic repulsion. Furthermore, calculations on the interaction of EG3 (three EG units) with water suggest that as charge contributes to inertness of EG-SAMs (see 2.3.1) because EG-SAMs might encapsulate hydronium ions, leaving hydroxyl ions at the water interface for charge compensation [97]. The effective surface charge was estimated to be as high as 1  $\mu\text{C}/\text{cm}^2$  which is in good agreement with electrokinetic measurements [98].

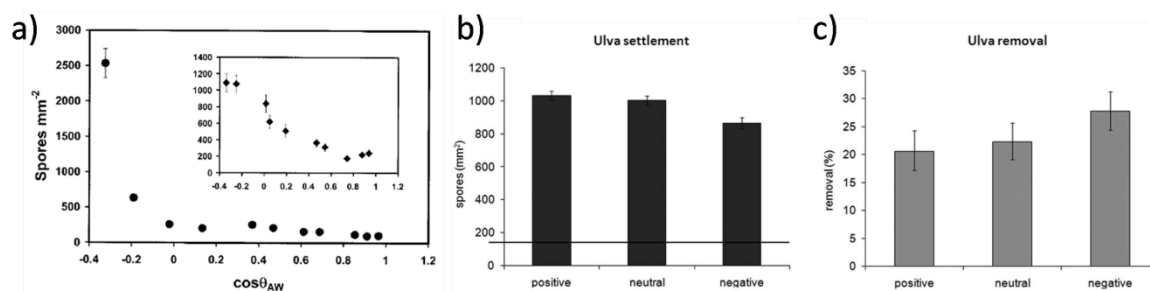


Figure 11: (a) *Ulva* zoospores settle less on COOH/CH<sub>3</sub> than on OH/CH<sub>3</sub> terminated mixed SAMs at comparable surface energy (contact angle) especially between  $\theta = 45^\circ$  to  $90^\circ$  ( $\cos\theta = 0$  to 1) [94]. Less *Ulva* zoospores settle on negatively charged electrets (b) and the spores are also released easier (c) [96].

## 2.4 High resolution imaging for cellular adhesion

In order to study cell-surface interactions the visual impression of the cell shape and the cell-surface contacts can be helpful. Apart from transmission light microscopy, which reveals the general condition of a cell attached to a surface, high resolution imaging of ultrastructural features is demanded in order to reveal the cell response to the surface. A common approach is the application of fluorescence microscopy using a variety of

techniques. The disadvantage of these techniques is the necessity of prelabeling the specimens with fluorophores as probes, which are supposed to bind to the desired cell location. A more desirable approach would be label-free imaging of sub micrometer structures. Imaging with X-rays provides this alternative by utilizing the intrinsic material contrast, due to the photoelectric effect. All elements show absorption edges at characteristic photon energies. By using X-rays of different energies within the so called water window, the absorption edges of biologically relevant elements in hydrated biological specimen can be addressed separately. The resulting material contrast can then reveal structures which are not accessible using other techniques.

Soft X-ray microscopy of intact frozen hydrated cells has already been shown to be a promising method to visualize ultrastructural features (Figure 12). Features such as nuclear membranes, pores and channels, mitochondrial cristae and lysosomal inclusions have been imaged in 3D [99]. Generally the use of partially coherent light can increase the image contrast strongly. The coherence of X-rays is prerequisite for techniques related to X-ray microscopy techniques such as X-ray diffraction microscopy for the phase retrieval [100; 101] or X-ray holography [102]. Suitable coherent sources for X-rays are synchrotrons, free-electron lasers [103] and high harmonic generation table top setups [104].

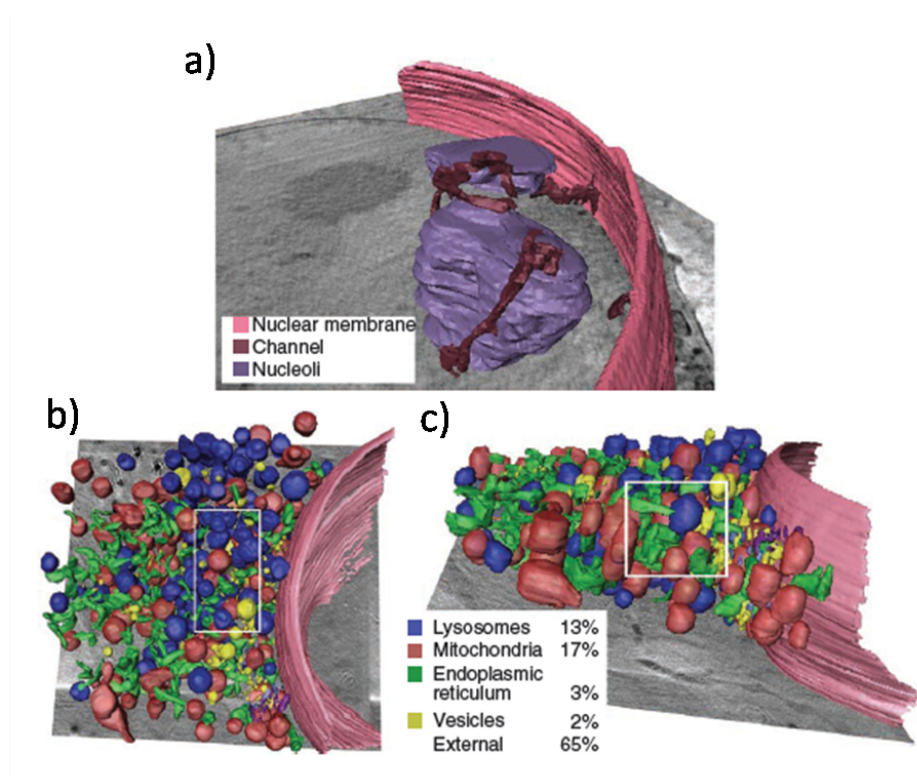


Figure 12: The volumetric rendering of the cell cytoplasm. Different ultrastructural features such as channels or organelles are imaged in 3D using tomographic X-ray microscopy. Figure was taken from [99].

## 2.5 Measurement of cell adhesion strength

Besides cell shape and structure the cell/surface interaction is characterized by the cells adhesion strength. Methods to measure the cell adhesion strength have nicely been reviewed by Christ and Turner [105]. The methods are divided into the three general categories centrifugal force assays, micromanipulation based techniques and hydrodynamic shear force assays which are all covered in the following section.

### 2.5.1 Centrifugal force assays

Centrifugal force assay is the simplest technique and is frequently used to perform high throughput screening. A common table centrifuge is modified for take-up of multiwell plates. Cells are plated inside each well, exposed to different conditions for each well (surface, reagent or cell type). Then the multiwell plate is placed vertically into the centrifuge and spun. The cells are thus exerted to a centrifugal force (Figure 13) which appears orthogonal to the substrate.

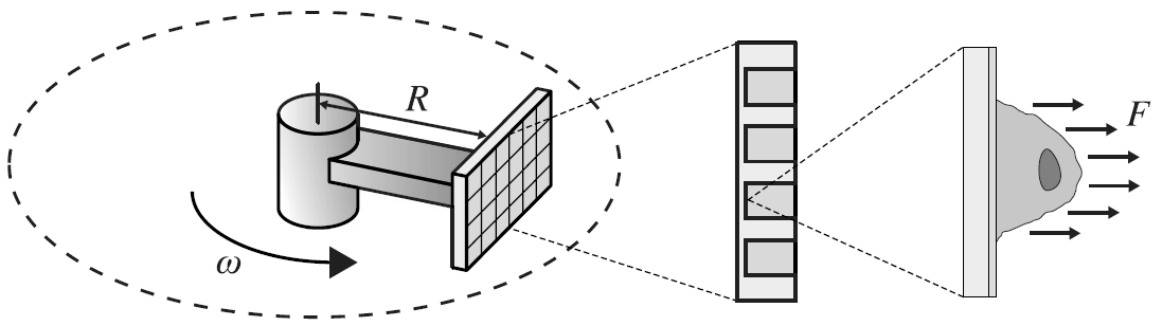


Figure 13: Scheme of a centrifuge assay. Adhesive cells inside a multiwell plate are exerted to centrifugal force orthogonal to the substrate. The force depends on the spinning speed and the distance to the centrifuge center. Figure was taken from [105].

The applied load depends on the difference in density between the cell  $\rho_{cell}$  and the medium  $\rho_{medium}$ , the cell volume  $V_{cell}$  and the relative centrifugal force  $RCF$  (1). The relative centrifugal force is dependent on the distance of the cell relative to the rotor center  $R$ , the angular rotor speed  $\omega$  and the gravitational acceleration  $g$  (2).

$$F = (\rho_{cell} - \rho_{medium}) \cdot V_{cell} \cdot RCF \quad (1)$$

$$RCF = \frac{R\omega^2}{g} \quad (2)$$

In each run, typically between 5 min and 10 min, only one force is applied. Common forces exerted on single cells range between 1 pN and 2000 pN [106; 107]. Converted to normal stress applied on the cell-substrate interface ( $\sigma = F / A$ ) the range is between about

1 mPa and 2000 mPa. These  $\sigma$  values are just sufficient to detach cells which are weakly adhered. Therefore the assay may be applied on short term cell adhesion studies only, where adhesion time is typically less than one hour. Secondly, the assay has to be performed at different forces to find the characteristic force necessary to detach 50 % of the adhered cells from the substrate. In order to determine the fraction of adherent cells fluorescence labeling [108], radiolabeling [109] techniques and quantification of genetic cellular material [110] are used.

As examples for its diversity the centrifugal force assay has been utilized to investigate the cell adhesion strengthening process on fibronectin and tenascin coated substrates [111], cell integrin binding on SAMs [107; 112 - 114] or osteoblast adhesion on peptide grafted polymer networks [115].

### 2.5.2 Micromanipulation based detachment techniques

Micromanipulation techniques directly exert force to individual cells. The most common ones are cantilever based apparatus like modified atomic force microscopes (AFM) and microaspiration, but also microplates [116], optical tweezers [117] and magnetic tweezers [118] have been used.

In cytodetachment based on cantilever technique, usually combined with microscopy, the tip of the cantilever is brought in direct proximity to the cell. Then the cell is pushed (Figure 14), dragged or lifted with the tip till the cell detaches and the AFM typical force-distance curve is recorded. The applied force  $F$  calculates from the cantilever stiffness  $k$  and the measured displacement  $x$  (3).

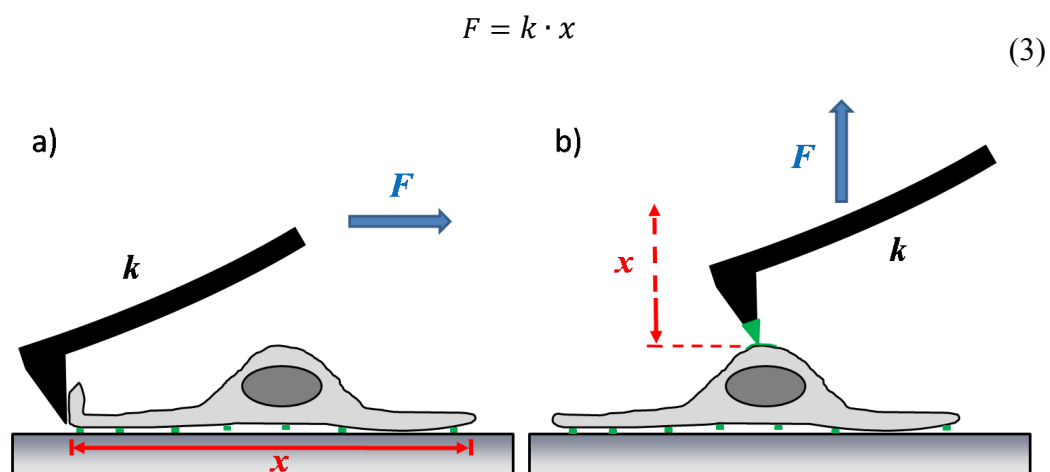


Figure 14: Scheme of cytodetachment. The tip is pushed against the cell (a) or the cell is lifted off with a “glue” functionalized tip (b). The force applied on the cell increases with pushing distance till the cell detaches. The force is measured by the deflection of the cantilever.

With this technique forces up to 1  $\mu$ N may be applied onto the cell [119] so that adhesion strength of long term incubated cells may be determined. Another advantage is the wide

range and easy tuning of the loading rate, so that the nature of single binding events may be revealed [120] as already predicted by the Bell model [121].

Different kind of tips and also tipless cantilevers and fibers were used to measure the cell adhesion strength. Examples include fibroblast adhesion on fibronectin and collagen [122], chondrocytes on various polymer surfaces [123], fibroblasts on SAMs [124] or titanium alloys [125] or fibroblast adhesion on nano patterned RGD revealing also the binding strength of single integrin-receptor clusters [120].

### 2.5.3 Hydrodynamic shear force assays for cell detachment

There are three main techniques to apply well defined laminar flow to generate hydrodynamic shear force onto cells: the spinning disk, radial flow chamber and parallel plate flow chamber [105].

In the **spinning disk setup** cells are seeded onto a circular substrate which was placed onto a spinning table inside a medium, usually phosphate buffer solution (PBS), filled chamber (Figure 15) [126; 127]. The cells adhere on the substrate. The substrate is spun to generate shear stress  $\tau$  onto the cells depending on fluid density  $\rho$ , fluid viscosity  $\mu$ , the angular speed of the disk  $\omega$  and the distance of each cell to the center of the spinning disk  $d_r$  (4).

$$\tau = 0.800d_r \cdot (\rho\mu\omega^3) \quad (4)$$

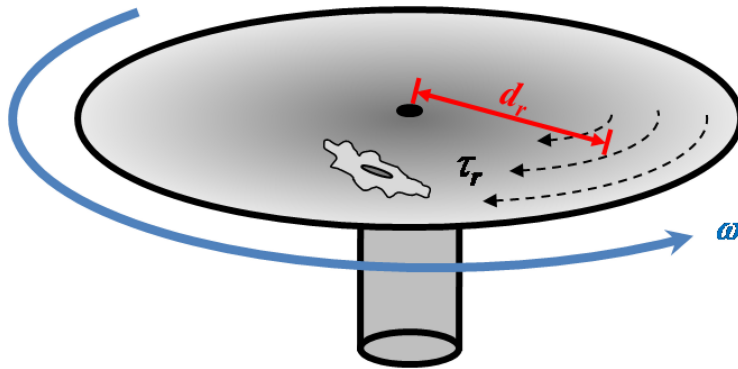


Figure 15: Scheme of spinning disk assay. A disk with adhered cells is spun inside a medium filled chamber. Shear stress depends linearly on the distance of the cell to the spinning center. Figure was inspired by [105].

In this experiment the force exerted on the cells depends on their position on the disk and thus a range of two orders of magnitude in shear stress is measured within a single experiment. Spinning times are in the order of 10 min and shear stresses of 1 dyn/cm<sup>2</sup> to 2000 dyn/cm<sup>2</sup> have been applied so far [128; 129]. The remaining adherent cell fraction is commonly quantified by microscopy. The cell adhesion strength has been measured in various systems, e.g. osteosarcoma cells on bioactive glass [127], pre-osteoblast cells on

RGD functionalized SAMs [130], integrin binding activation of cells on fibronectin [131] or human bone marrow cells on hydroxyapatite [132].

In **the radial flow chamber** the shear stress results from active liquid flow. The flow enters the circular substrate from the center and spreads over the surface (Figure 16). The flow velocity decreases with increasing radial distance and hence the shear stress  $\tau$  on the cells attached to the substrate decreases with increasing distance  $d_r$  to the inlet (5) [133]. In this equation  $Q$  is the volumetric flow rate,  $\mu$  the medium viscosity,  $\rho$  the density of the medium and  $h$  the chamber height. Cell detachment assays in radial flow chambers are usually performed within 10 min. For transparent substrates the detachment can be followed by time lapse microscopy. However, the maximum applied shear stress is below  $200 \text{ dyn/cm}^2$  and thus the setup is mostly restricted to short time adhesion studies. Studies with this setup include adhesion of osteoblast on RGDs [134; 135], CHO cell adhesion on modified silicon oxide substrates [136] or fibroblast adhesion on fibronectin coated glass [133; 137].

$$\tau = \frac{3\mu Q}{\pi h^2 d_r} - \frac{3\rho Q^2}{70\pi^2 h d_r^3} \quad (5)$$

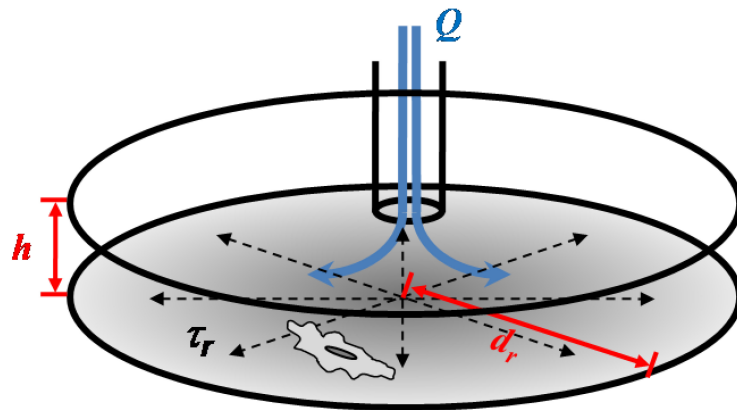


Figure 16: Scheme of radial flow assay. The flow enters from the center of a circular disk. The shear stress exerted onto the cells is decreasing with radial distance to the inlet.

**The parallel plate flow chamber** follows the same principle of active flow as the radial flow chamber. The chamber or channel consists of two flat plates sandwiching the gasket consisting of a polymer. On the upper plate two holes serve as inlet and outlet for the liquid flow. Cells are injected into the channel and adhere to the bottom substrate till the flow for cell detachment is started. Hydrostatic pressure [138] or pumps [139] are used to control the volumetric flow  $Q$ . The applied shear stress  $\tau$  onto the cells, which is caused by the parabolic flow profile, is uniform within the main parts of the channel if the aspect ratio between channel width  $w$  and channel height  $h$  is high enough ( $w > 10 h$ ). The shear stress,

which is here also dependent on the medium viscosity  $\mu$  is given by equation (6), see also Figure 17.

$$\tau = \frac{6Q\mu}{h^2w} \quad (6)$$

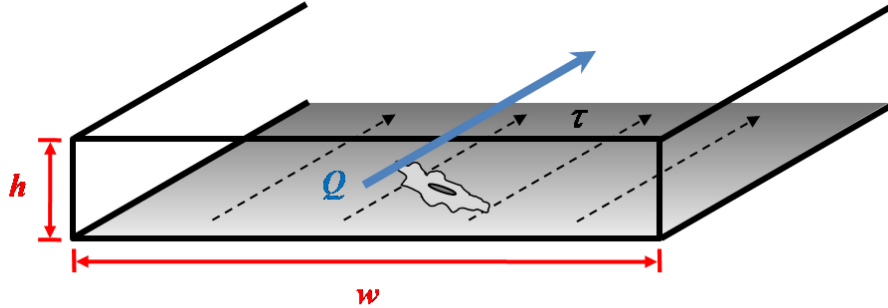


Figure 17: Scheme of a parallel plate flow chamber. The wall shear stress is uniform throughout the channel bottom. It depends only on the fixed channel geometry and the applied volume flow.

With this setup shear stress higher than 6000 dyn/cm<sup>2</sup> has been achieved [140]. To stay in the laminar flow regime, the Reynolds number for this geometry (7) should not exceed 2300.

$$Re = \frac{2Q\rho}{\mu(h+w)} \approx \frac{2Q\rho}{\mu \cdot w} \quad (7)$$

Inserting equation (7) in equation (6) reveals the direct correlation between  $\tau$  and  $Re$ , which depends mainly on the channel height  $h$  (8).

$$\tau \sim \frac{Re}{h^2} \quad (8)$$

Therefore relatively flat channels (less than 100  $\mu\text{m}$ ) are used to achieve high shear stresses while keeping the flow laminar. Also, by variation of the channel height along the length of a channel, different stresses may be accessed within on experimental run [141; 142]. Instead of that, also the channel width can be varied [143].

Special care has also to be taken for the channel length. The flow coming from the tubing has to develop along the length  $L_e$  to full homogeneity inside the channel because of the high pressure drop at the connection point (9) [144]. Thus, the channel length should be greater than  $L_e$ .

$$L_e \approx 0.05 \cdot \frac{2hw}{h+w} \cdot Re \quad (9)$$

Parallel plate flow channels have been used to measure weakly adhered cells on rigid substrates as glass [139], polymers with wettability gradients [145], poly(L-lactic acid) films [146] or SAMs [147]. More recently, cell adhesion of strongly adhered long term incubated cells has been studied using channel heights well below 100 $\mu\text{m}$  [140; 144]. In a

detailed study special attention was paid to relationship between cell morphological characteristics and cell adhesion [144]. Detailed analysis revealed that the three cell membrane deformations edge delamination, membrane stretching, membrane deformation and rupture occur before cell detachment (Figure 18). The probability for a specific mode scales with the collagen density on a substrate.

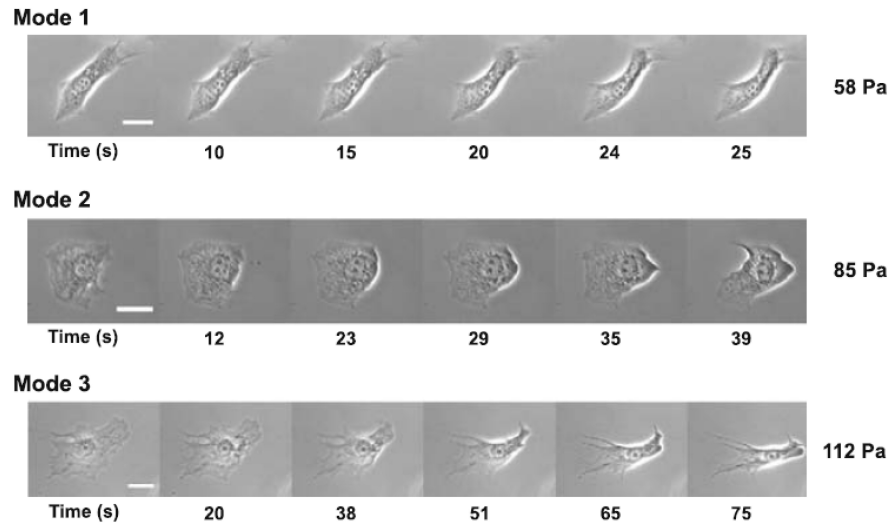


Figure 18: Deformation modes of long term adhered fibroblast cells before detachment. Mode 1 shows edge delamination, mode 2 membrane stretching and mode 3 membrane deformation and rupture. Image taken from [144].



## 3 Materials and Methods

### 3.1 Preparation techniques

#### 3.1.1 Preparation of self assembled monolayers on gold

Self-assembled monolayers give access to surfaces with well defined and tuneable properties [148; 149]. SAMs have been extensively studied as protein resistant materials [150], with respect to their bio-compatibility for medical applications [151], and for developing anti-fouling surfaces [6; 152; 153] (see also chapter 2.3.1). The most frequent used strategies to obtain highly ordered SAMs are assemblies from organosilanes on silicon oxide and alkanethiols on gold.

Gold substrates were purchased from Georg Albert (PVD-Beschichtungen, Germany). Thin polycrystalline gold films were prepared by thermal vapor deposition of 30 nm gold (99.99 % purity) onto polished float glass slides (Nexterion B®) predeposited with a 5 nm titanium adhesive layer. Evaporation was performed at a pressure of  $2 \times 10^{-7}$  bar and a deposition rate of 0.5 nm/s to result a root-mean-square roughness of about 1 nm [154]. Gold substrates were kept in argon atmosphere until used. Before SAM synthesis the gold substrates were cut into 25 mm x 25 mm pieces, cleaned under UV radiation for 2 h. Afterwards the substrates were rinsed with abs. ethanol, treated in an ultrasonic bath for 1 min and rinsed again. Each substrate was measured by ellipsometry. The substrates were then put into 1 mmol freshly prepared ethanolic dodecane thiol (C12), oligo ethylene glycol thiol (EGXOH) or amino terminated undecane thiol (AUDT) with 3 mmol triethylamine solutions. The most reproducible SAMs were obtained from solutions which were older than one week and pre immersed with a “dummy” substrate which is supposed to adsorb impurities from the fresh solution. After 24 h immersion the substrates were rinsed with ethanol, treated in an ultrasonic bath for 1min to remove non chemisorbed thiols and rinsed again. The samples were blown dry with argon and were used instantly or kept under argon atmosphere until used.

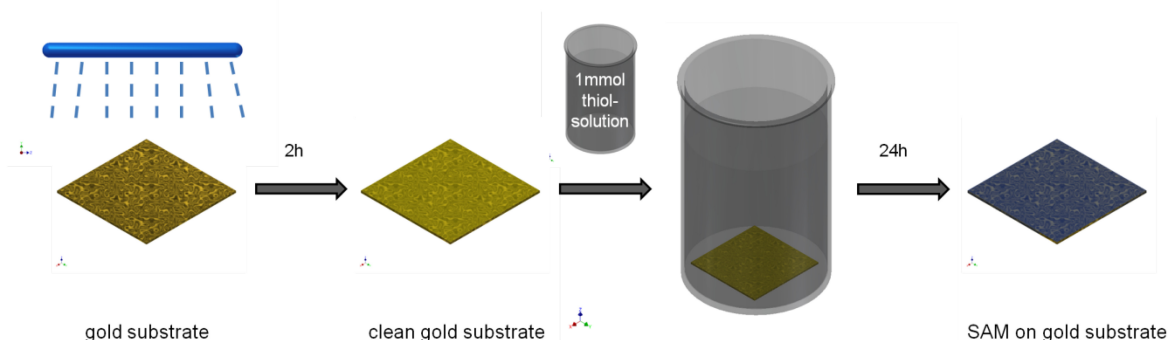


Figure 19: Scheme of SAM preparation protocol. First the substrate is cleaned by UV light, rinsed with ethanol and subsequent immersed in thiol solution for 24 h.

### 3.1.2 Protein adsorption assay

Protein adsorption assays on SAMs are frequently used to test surfaces towards their capability to prevent cell adhesion because resistance of cell adhesion often correlates with the repellence of proteins [37; 155] (see chapter 2.3.1). Still, cell adhesion seems to be possible, even if the adsorption of proteins fails [38].

Fibrinogen, a protein located in the ECM secreted by adhesive mammalian cells, is used for the adsorption assays (Figure 20). Following established protocols [37] 20 mg fibrinogen was dissolved in 10 mL filtered PBS using an ultrasonic bath. The samples were pre-immersed in 10 mL filtered PBS for 10 min and fibrinogen solution was added to result a 1 mg/mL fibrinogen solution. After 60 min at room temperature the solution was continuously diluted by 3 L deionized water and 500 mL Milli-Q® water to avoid a Langmuir-Blodgett film formation during pulling the sample through the water/air interface. The samples were dried under argon stream and measured with ellipsometry.

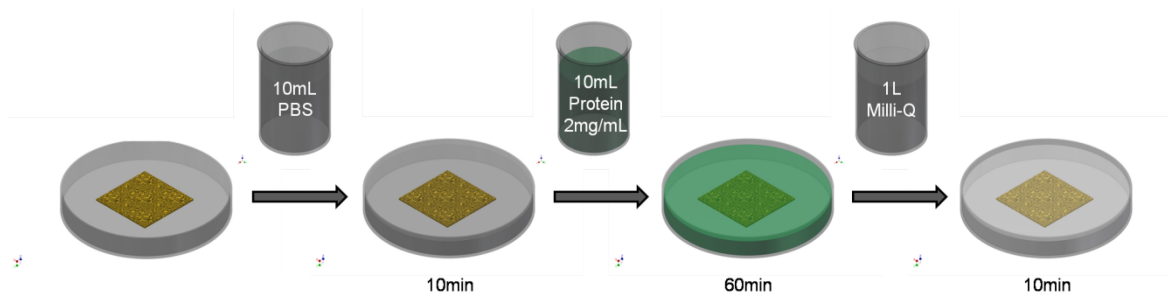


Figure 20: Scheme of protein adsorption assay. The substrate is immersed in pure buffer and protein solution is added. After 60 min the solution is carefully diluted with Milli-Q® water before taking out the sample.

### 3.1.3 Preparation of nanotextured PPX-films on glass

PPX films are capable to present an anisotropic surface (see chapter 2.3.3) by taking advantage of the oblique angle chemical vapor deposition (CVD) technique. Due to self shadowing effect the pyrolysed paracyclophane the nanorods grow at a controlled incident angle.

Nanotextured poly(chloro-*p*-xylylene) (PPX-Cl) films on glass slides were kindly provided by collaboration with the lab of Prof. Melik Demirel (Pennsylvania State University, USA). The synthesis was performed as follows [91; 156]:

Nexterion B® glass slides were cleaned by successive immersion in HCl/CH<sub>3</sub>OH (1:1 v/v), deionized water, and concentrated H<sub>2</sub>SO<sub>4</sub>. Afterwards styrylethyltrimethoxysilane was used to form a self-assembled organosilane monolayer [157] to enhance the adherence of the PPX-Cl film to the glass substrate. The substrate was baked on a hotplate at 120 °C for 4min to complete the dehydration reaction that forms the siloxane bond between the organosilane and the glass substrate.

PPX-Cl deposition (Figure 21) was performed using a Parylene Deposition System PDS 2010 (SCS, Indianapolis, IN, USA) modified by using a glass bell jar (BOC Edwards, Wilmington, MA, USA) for the vacuum chamber. (2,2)-Dichloroparacyclophane in powder form used as a source material was heated to produce a vapor flux and directed onto a substrate through a nozzle. The substrate was mounted on a holder at a fixed deposition angle [158]. Deposition was performed at vapor-flux angles of  $< 35^\circ$  with respect to the substrate surface resulting in columnar thin-film coatings of various nanorod tilt angles (i.e.  $57^\circ - 63^\circ$ ). Planar films were deposited by operating the coating system in normal configuration using a baffle to disperse the entering PPX-Cl vapor. Deposition parameters such as sublimation temperature, pyrolysis temperature and chamber vacuum were kept the same for both the planar and columnar film deposition and were set to  $175^\circ\text{C}$ ,  $690^\circ\text{C}$  and 32 torr, respectively. Morphology and topography of the films were characterized using a scanning electron microscope. For that purpose the substrates were sputter coated twice with carbon prior imaging to reduce charging effects. Film thickness and nanorod tilting angles were determined by imaging the cross-sections of cleaved PPX substrates with the scanning electron microscope.

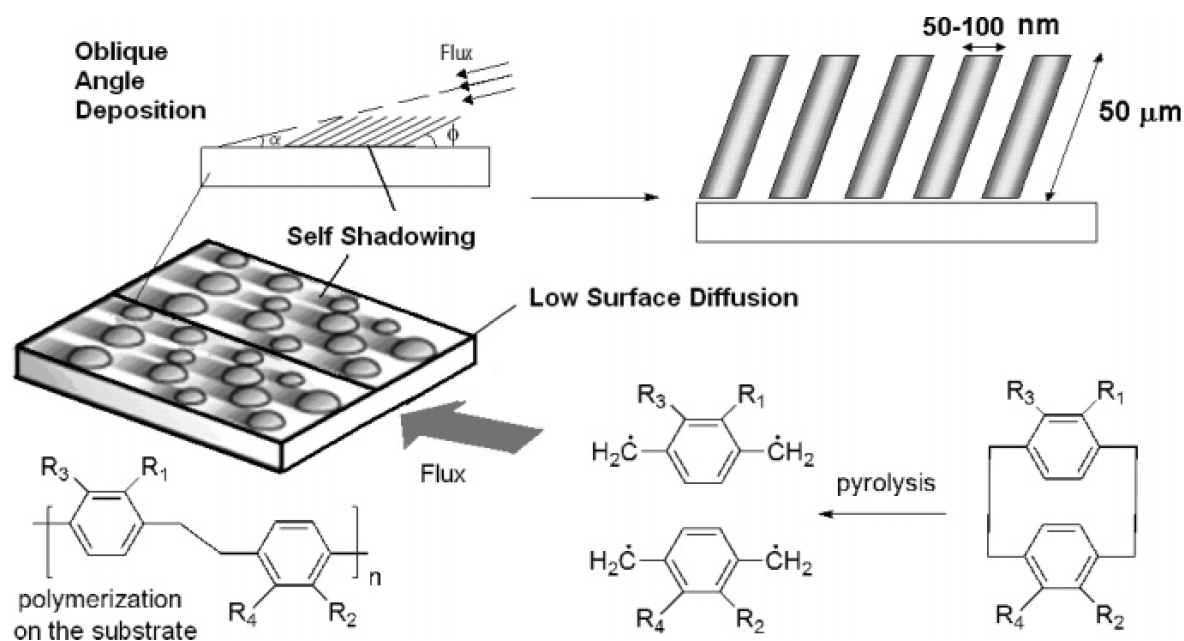


Figure 21: Flow chart of the deposition of nanostructured poly(*p*-xylylene) (PPX) thin films showing the paracyclophane chemistry together with the vapor deposition technique. Nanorods grow at an inclined angle  $\phi$  when the vapor flux is directed at an angle  $\alpha \leq \phi$ . Side groups for PPX-Cl are  $R_1 = \text{Cl}$ ,  $R_2 = \text{H}$ ,  $R_3 = \text{H}$ , and  $R_4 = \text{Cl}$ . Figure is taken from [158].

### 3.1.4 Preparation of Polysaccharides on glass

Compared to the highly ordered molecular small SAMs, polysaccharides consist of long, partially branched, carbohydrate chains with circular sugar subunits. Grafted on surfaces

these macromolecules form rather a randomly distributed network than an ordered monolayer. The surfaces have a hydrogel nature and are thus considered as bio repellent materials (see chapter 2.3.1). On the other hand these materials show a broad variety of functions in the body (see chapter 2.3.2).

Thin films of two polysaccharides, hyaluronic acid (HA) and alginic acid (AA), on glass slides were prepared in our group by Georg Meseck [159] following published protocols [49; 160163] (Figure 22).

Nexterion B® glass slides were subjected to an oxygen plasma device (TePla 100E PS, PVA TePla AG, Wettenberg, Germany) at 0.5 mbar partial pressure and 150 W for 3 min. Together with a beaker containing 0.6 mL of 3-aminopropyltriethoxysilane (APTES) the cleaned and activated substrates were put into a desiccator. After evacuation to 50 mbar the chemical vapor deposition was carried out in an oven at 150 °C within 1h to form an amino functional surface. The samples were rinsed and ultrasonicated with ethanol *p.a.*, blown dry in a stream of nitrogen and stored under argon until use. HA and AA were coupled to the amino functionalized surfaces by EDC/NHS chemistry. Under vigorous stirring, 1 mg/mL of the respective sodium salt of the polysaccharide was dissolved in 10 mM HEPES buffer. The carboxylic groups in the polysaccharide were subsequently activated by adding NHS (0.05 M) and EDC (0.1 M) under further stirring for 20 min. Coupling to the surface was achieved by immersion of the amino functionalized glass slides into the activated polysaccharide solution. After 18 h on a vibrating table the reaction was terminated by dilution with 2 L of Millipore®-water. Further immersion in daily exchanged Millipore®-water for 3 days removed uncoupled polysaccharides and EDC/NHS residues. The substrates were blown dry in a stream of nitrogen and stored under argon until use. After each step the films were characterized by contact angle goniometry, spectral ellipsometry and X-ray photoelectron spectroscopy using Scofield photoionization cross-sections [164].

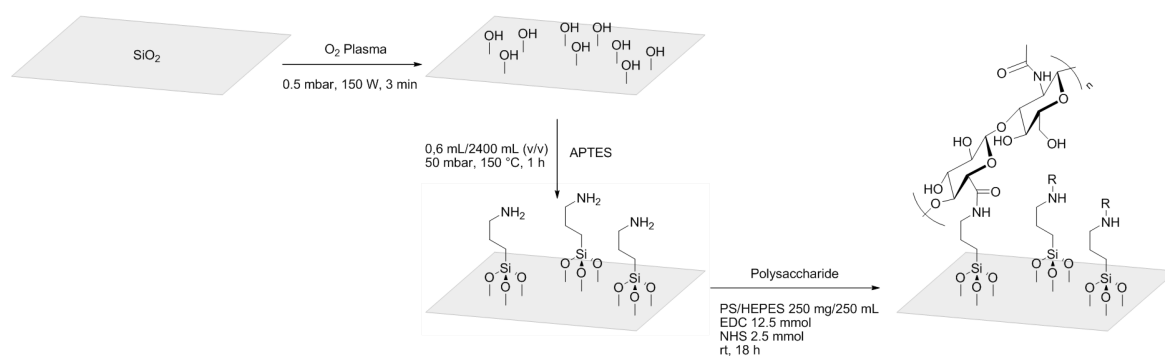


Figure 22: Scheme of polysaccharide preparation. A silicon oxide surface was activated by oxygen plasma and reactive amino groups were introduced by CVD with APTES. Polysaccharides were coupled via EDC to the amino functionalized surface. Picture was taken from [159].

### 3.1.5 Preparation of single poled and periodically poled LiTaO<sub>3</sub>

Ferroelectric materials are capable of permanent polarization which is especially useful in studies where a set of different surface charges is desired without changing the chemical composition of the substrate (see chapter 2.3.4).

Single (+), (-) poled and periodically (+)/(-) poled ferroelectric lithium tantalite (LiTaO<sub>3</sub>) were kindly provided by our collaborator Prof. Peter Dowben (University of Nebraska-Lincoln, USA). The preparation was performed by the group of Prof. Kenji Kitamura (National Institute for Materials Science, Japan) following established protocols for the preparation of poled LiNbO<sub>3</sub> [165; 166].

Periodically poled LiTaO<sub>3</sub> of congruent composition with a domain pattern width of 22 μm have been fabricated via photochemical reaction. A photoresist mask was deposited onto the face of the c-axis (three fold rotational symmetry) of a parallel plane cut LiTaO<sub>3</sub> crystal (~5 x 5 x 0.5 mm<sup>3</sup>) and a voltage of 10 kV was applied through a fixture with an electrolyte solution. After the poling process the photoresist was removed by chemical-mechanical polishing. The ferroelectric properties of the domain patterns were characterized using piezoresponse force microscopy [167].

### 3.1.6 Cell culture

In this thesis different cell lines and primary cells were used (Table 1 and Figure 23). Adherent cells lines were REF52 and H1299. Suspension cells were the lines KG-1a, HL-60, K-562, Jurkat and Kasumi-1. Primary HPC cells were collected from umbilical cord blood and purified following established protocols [168] by our collaborators in the group of Prof. Ho (Department of Medicine V, University of Heidelberg).

The cells were cultured in a humidified incubator with 5 % to 8 % CO<sub>2</sub> at 37 °C. The initial culture medium used was supplemented with 10 % fetal bovine serum, 1 mM L-glutamine, and 100 units/mL penicillin/streptomycin solution. The adherent cell lines were harvested at full confluence from T-25 tissue culture flasks by rinsing with 5 mL PBS and 1 mL 0.05 % trypsin-EDTA solution and subsequent incubation with 1 mL 0.05 % trypsin-EDTA solution for 5 min. Afterwards the solution was diluted with 5 mL culture medium and put into the centrifuge for 5 min at 1200 rpm. The cell pellet was resuspended with fresh medium and used for experiments instantly. For continuous cultivation the cells were split 1:10 and seeded in T-25 tissue culture flasks. Confluent passages were obtained every 2 to 3 days. Non adherent cell lines were harvested by centrifugation of the complete 5 mL cell suspension from the T-25 culture flask at 1200 rpm for 5 min.

Table 1: Cell lines used for experiments

Cell line	Organism	Tissue	Description	Culture Media	Reference
REF52	Rat	Embryo	Fibroblast, adherent	DMEM, 5 % CO <sub>2</sub>	[169]
REF52 YFP-paxillin	Rat	Embryo	Fibroblast, adherent	DMEM, 5 % CO <sub>2</sub>	[170]
H1299 (CRL-5803)	Human	Lung	Epithelial, adherent	RPMI 1640, 8 % CO <sub>2</sub>	[171]
KG-1a (CCL-246.1)	Human	Bone marrow	Myeloblast, suspension	RPMI 1640, 5 % CO <sub>2</sub>	[172; 173]
HL-60 (CCL-240)	Human	Peripheral blood	Promyeloblast, suspension	RPMI 1640, 5 % CO <sub>2</sub>	[174]
K-562 (CCL-243)	Human	Bone marrow	Myeloblast, suspension	RPMI 1640, 5 % CO <sub>2</sub>	[175]
Kasumi-1 (CRL-2724)	Human	Peripheral blood	Myeloblast, suspension	RPMI 1640, 5 % CO <sub>2</sub>	[176]
Jurkat (TIB-152)	Human	T-cell leukemia	Lymphoblast, suspension	RPMI 1640, 5 % CO <sub>2</sub>	[177]
HPC (primary)	Human	Umbilical cord blood	Hematopoietic cell, suspension	LTBMC, 5 % CO <sub>2</sub>	[178]

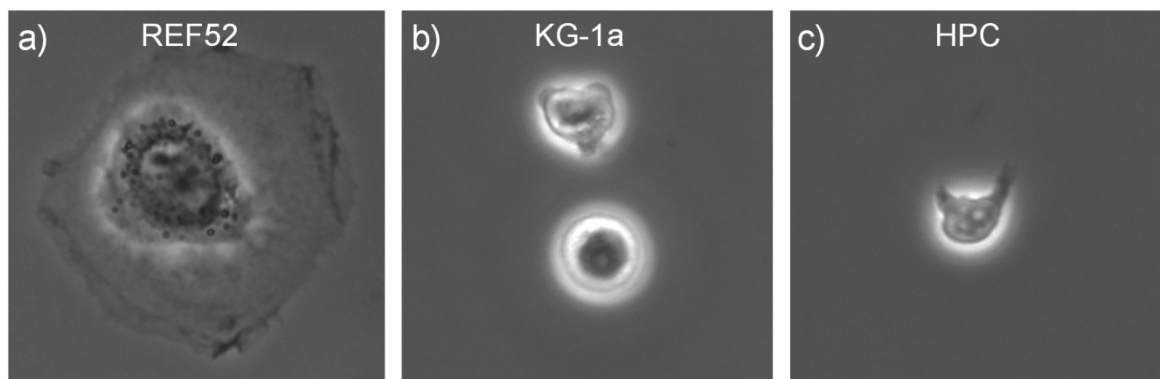


Figure 23: Examples of adherent and suspension cell lines used in this study. Phase contrast images were taken with 40x Ph2 objective. Fully spread adherent cells are much larger than suspension cell lines (a). Suspension cell lines occur in round (b) or elongated with pronounced filopodia (c). Lateral image length is about 65  $\mu\text{m}$ .

### 3.1.7 Sample preparation for ultrahigh vacuum applications

For X-ray or electron microscopy under vacuum conditions biological specimen were fixed and dried on silicon nitride (SiN) membranes with a typical window size of 1 x 1 mm<sup>2</sup> and a thickness between 30 nm and 100 nm. It was found to be crucial that the membranes

were kept wet during the whole process. Instead of washing steps gentle exchange of solution, usually leaving the membranes 2 mm below the liquid/air interface were performed. At first the SiN membranes were dipped upright into a multiwell plate containing PBS. In case of mammalian cells the SiN membranes were precoated with 1 mg/ml fibrinogen in PBS buffer for 30 min and washed three times in PBS and once in culture medium. Then, freshly suspended cells were seeded on the membranes according to the desired dilution. Adherent cells were incubated for 4 h - 5 h at culture conditions, suspension cells and bacteria for 1 h prior to fixation. The membranes were washed three times with PBS and then incubated with 2 % paraformaldehyde (PFA) in PBS for 15 min to 20 min at room temperature.

After fixation, the membranes were washed five times with PBS solution. PBS was exchanged for MilliQ water in three steps. After that, the water was exchanged every 10 min for ethanol/water in six steps starting at 50 % ethanol. Finally the solution was exchanged two more times for 100 % ethanol within 1 h.

The membranes were transferred into a custom build sample holder inside the ethanol filled critical point drying device (CPD 030, Bal-Tec, Schalksmühle, Germany). The critical point drying was performed according to an established procedure. The exchange procedure from ethanol to liquid carbon dioxide was conducted 6 times to 8 times. Then the temperature was raised to 40 °C and the pressure increased from 50 bar to 75 bar. The system was kept in the critical phase for 10 min before the gas was released slowly within 1 h to prevent sample wetting due to recondensation of carbon dioxide. The dried samples were kept in gelatin capsules to prevent rehydration.

## 3.2 Analytical techniques

### 3.2.1 Contact angle goniometry

Contact angle goniometry is a technique to determine the wettability of a surface. In the classical setup the solid/liquid interaction at ambient conditions of a substrate is measured. A small contact angle displays a high wettability and therefore a strong interaction of the liquid with the solid (Figure 24).



Figure 24: Contact angles of a polar liquid on hydrophobic and hydrophilic substrate.

The contact angle  $\theta_Y$  in ideal systems is described by Young's equation [179].  $\gamma_{SL}$ ,  $\gamma_{SV}$ ,  $\gamma_{LV}$  describe the three tensions in between solid-liquid, solid-vapor and liquid-vapor (10).

$$\cos\theta_Y = \frac{\gamma_{SL} - \gamma_{SV}}{\gamma_{LV}} \quad (10)$$

Equation (10) is only valid for small droplets (gravitational force is negligible) on flat chemically homogeneous surfaces. Topography and chemical composition influence the contact angle. Surface structure effects the wetting behavior and can be described with the Wenzel equation [180] (Figure 25a). The Wenzel contact angle  $\theta_W$  is determined by the surface roughness ratio  $z$  which is defined as the ratio between actual and projected surface area and the Young contact angle  $\theta_Y$  of a flat surface from the same material (11).

$$\cos\theta_W = z \cdot \cos\theta_Y \quad (11)$$

If the structured surface may not be fully wetted, which is the case for the lotus effect (see 2.3.3), the wetting can be described by the Cassie-Baxter equation [181] (Figure 25b). The Cassie contact angle  $\theta_{CB}$  is dependent on the surface contact fraction  $\varphi$  of the liquid droplet and the surface characteristic contact angle  $\theta_Y$  (12).

$$\cos\theta_{CB} = \varphi \cdot (\cos\theta_Y + 1) - 1 \quad (12)$$

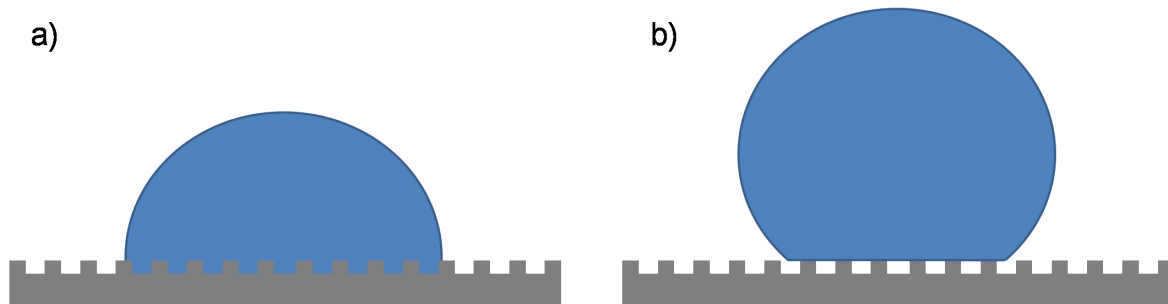


Figure 25: Scheme of the Wenzel (a) and the Cassie-Baxter (b) principle. In the Wenzel model the surface roughness contributes to the contact angle. In the Cassie-Baxter model the droplet does not fully wet the substrate due to surface roughness.

The degree of interaction of polar water molecules with the substrate by means of wettability reveals the surface free energy. In this work the contact angle goniometry was used to characterize water contact angle of SAMs and polysaccharides. Measurements were performed on a custom build goniometer with a tilting stage with temperature control (Figure 26). This makes the setup capable to measure droplet roll off angle and temperature dependence of contact angle for thermoresponsive surfaces such as poly(N-isopropylacrylamide). The camera records the image of a droplet on the sample. The program CAM 3.02.01 (Kölsch, P.; Motschmann, H.; Orendi, H.) calculates the contact

angle by image analysis via thresholding and geometric means. In the following characterization data the contact of a substrate was measured at three different positions and the mean value was calculated accordingly.

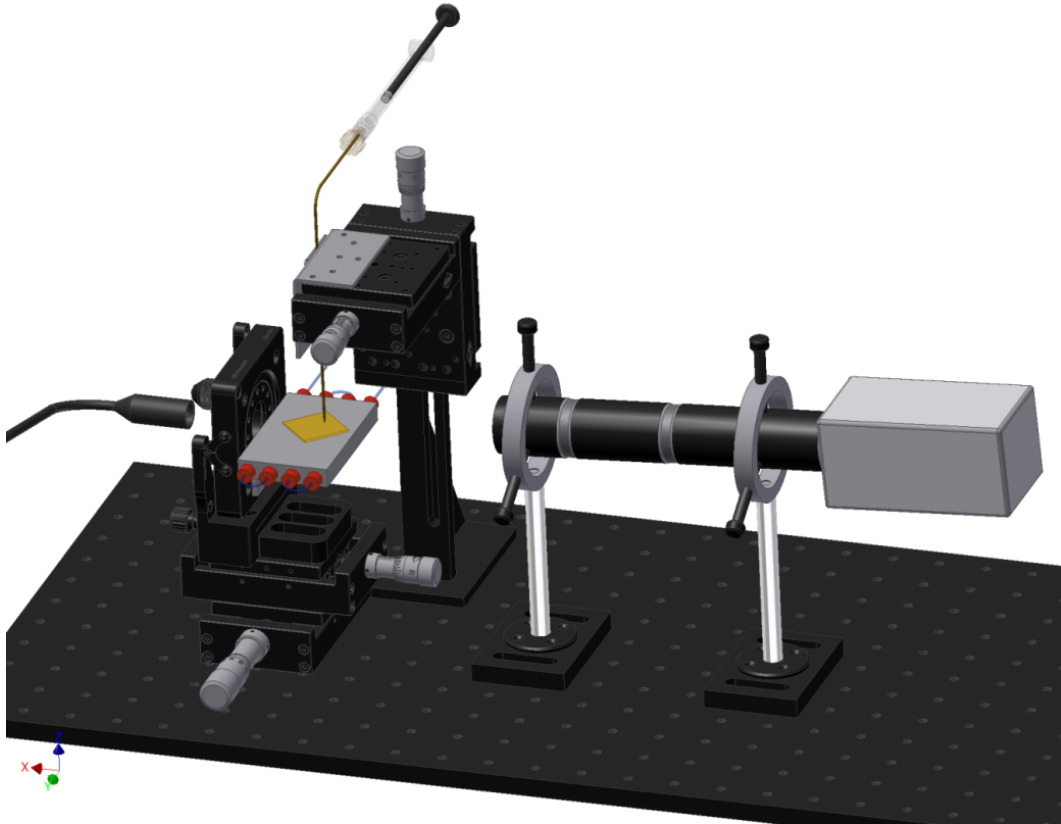


Figure 26: Setup of the custom made contact angle goniometer with temperature control unit.

### 3.2.2 Spectral ellipsometry

Ellipsometry is an optical technique which uses polarized light in the region of visible to near infrared to determine material properties of surfaces and thickness of thin films.

A beam of linear polarized light (*s*- and *p*-polarized) is directed onto a substrate and the reflected light is collected on a detector (Figure 28). During interaction with the substrate light is adsorbed and the phase of *s*- to *p*-polarized part is shifted so the light gets elliptically polarized (Figure 27). The reflected light passes through the analyzer and the detector measures intensity and phase shift between the *s*- and *p*-polarized parts of the light. The change in polarization can be expressed by the ratio  $r$  of the reflection coefficients  $r_p$  and  $r_s$  in the form of equation (13) [182]:

$$r = \frac{r_p}{r_s} = \tan(\psi) \exp(i\Delta) \quad (13)$$

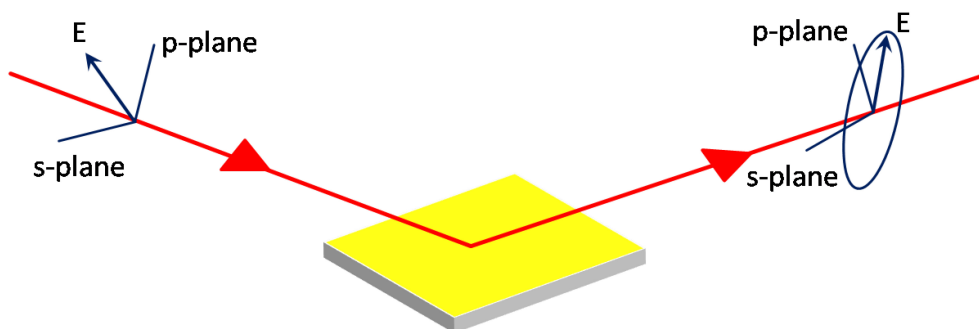


Figure 27: Ellipsometry working principle. The linear polarized light is reflected by the sample and gets elliptically polarized. Image inspired by [182].

The parameter  $\Delta$  represents the change of the phase difference between  $p$  and  $s$  components and  $\psi$  the amplitudes ratio of  $p$  and  $s$  components. Both parameters are accessible by measurement but the optical constants have to be calculated by regression analysis. Therefore a model has to be introduced which represents the substrate with all known optical properties. With knowledge of the substrate thickness the optical constants can be determined and the other way round. Film thickness down to the sub-nanometers regime can be determined. In the case of a multilayer each layer has to be modeled individually.

Film thicknesses were measured with a M-44 multiple wavelength ellipsometer from J. A. Woollam Co., Inc. (Lincoln, NE) aligned at a nominal incidence angle of  $\sim 75^\circ$  to the surface normal. SAM and protein layer thickness were determined by the modeling software (WVASE<sup>TM</sup> from J. A. Woollam Co.) using a single cauchy model layer with an estimated refractive index of 1.45.

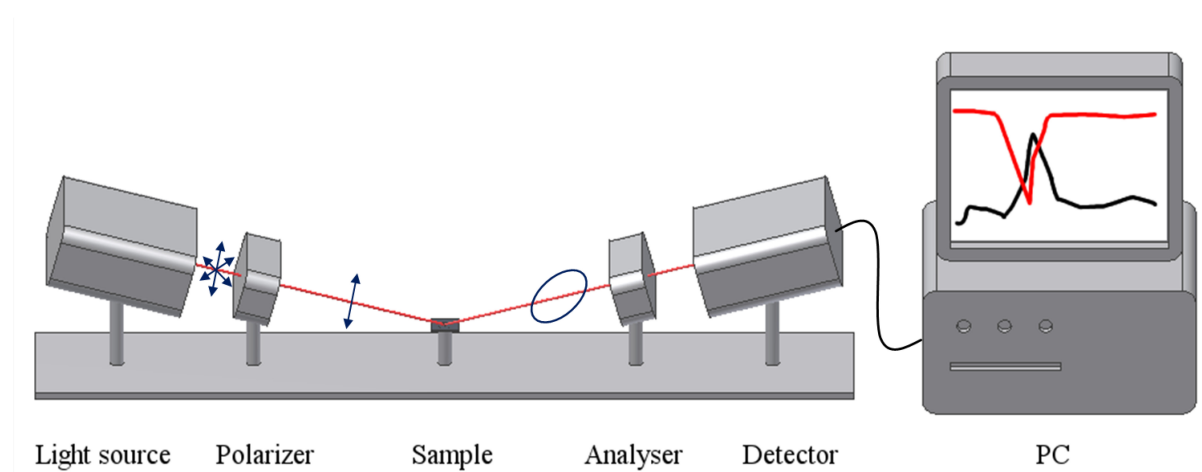


Figure 28: Scheme of ellipsometry setup. The source emits light which is linear polarized. After reflection from the sample the light is elliptically polarized. The light polarization direction is sorted by the rotating analyser and its intensity by the detector. The PC can collect the circular dependent intensity and calculate the layer thickness using models.

### 3.2.3 X-ray photoelectron spectroscopy

X-ray photoelectron spectroscopy (XPS) is a surface sensitive technique to investigate the chemical composition of a sample. Based on the Einstein photo electronic effect (Figure 29) the substrate is probed with X-rays which cause electrons to emit from the substrate with a kinetic energy (14):

$$E_{kin} = h\nu - E_B - \psi_{XPS} \quad (14)$$

The electron binding energy  $E_B$  is determined by measurement of the kinetic energy  $E_{kin}$  with an analyzer and the knowledge of the energy of the X-rays  $h\nu$  produced by the source and the work function of the instrument  $\psi$ .

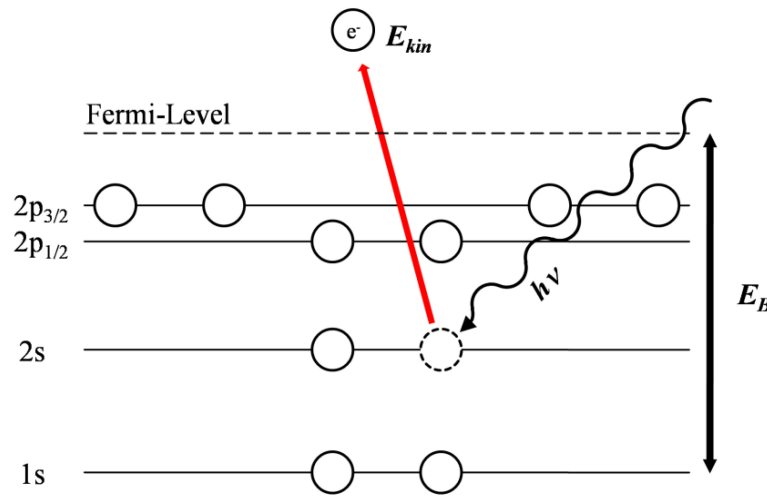


Figure 29: Scheme of the photoelectric effect. X-rays hit the inner shell electrons of a material followed by the emission of the electron.

The used instrument was a MAX 200 with a LHS 12 spectrometer (Leybold-Heraeus GmbH, Germany) equipped with an Al K<sub>α</sub> and a Mg K<sub>α</sub> X-ray source (1486.6 eV and 1253.6 eV, respectively) and a Specs EA200 multi-channeltron detector. Measurement with the Mg-Anode at 250 W (13 kV, 18 mA), 48 eV pass-energy and resolution of 0.7 eV was performed with a step size of 0.2 eV for each element.

For data evaluation SPECSLAB software was used to normalize the peaks of Au 4f<sub>7/2</sub> signal to 84.00 eV. XPSPEAK software was used to determine signal intensity using the Shirley background subtraction method [183] and Voigt peak modeling with Gauss/Lorentz ratio 4 : 1. The attenuated integral signal intensities of the gold substrate are especially useful to determine the film thickness of SAMs and protein layers. The film thickness can be calculated using Lambert-Beers law (15) where  $I(d)$  is the signal intensity after attenuation;  $I_0$  is the entrance signal intensity,  $\epsilon$  the material adsorption constant,  $c$  the material concentration and  $d$  the material thickness.

$$I(d) = I_0 \cdot \exp(-\epsilon cd) \quad \text{or} \quad d = \epsilon c \cdot \ln \frac{I_0}{I(d)} \quad (15)$$

In XPS, material adsorption coefficient  $\epsilon$  and concentration  $c$  can be expressed through the attenuation length  $\lambda_{att}$  (see Table 2) and the geometric parameter of the take off angle expressed as  $\cos\theta$  (16).

$$d = \lambda_{att} \cdot \cos\theta \cdot \ln \frac{I_0}{I(d)} \quad (16)$$

The sample can be used as an internal reference. An argon driven sputtering gun is used to remove the SAM from the surface followed by measurement of the underlying Au layer which is then used as the reference for SAM thickness determination.

Table 2: The attenuation length of photoelectrons for Mg  $K_\alpha$  as determined by Nikolaus Meyerbröcker, according to the technique described in the diploma thesis [184].

Signal	Au 4f	C 1s	O 1s	S 2s
$\lambda_{att} / \text{Å}$	36.5	30.1	22	33.5

### 3.2.4 Light Microscopy

Light microscopy is the most widely used technique for visual analysis in the biological and medical area. Although the working principles and different techniques are well known, for this work special modifications had to be accomplished and will be discussed here. A custom-made incubator, inspired from a prototype invented by the group of Prof. Spatz, was designed and built to meet the needs of long term live cell imaging (37 °C, 5 % CO<sub>2</sub>). The special design of the incubator, enclosing most of the inverted Nikon microscope TE-2000 (Figure 30), was needed to ensure constant environmental conditions. The incubator was made of transparent poly(methyl methacrylate) (PMMA) with heating cable attached to the walls. A temperature control unit was connected to the heating cable and a Pt100 thermocouple, located at the center of the incubator, in order to back regulate the temperature. A gas valve controlled tubing serves as CO<sub>2</sub> inlet to generate appropriate gas atmosphere. Both gas valve and a CO<sub>2</sub> sensor, which was placed in proximity to the specimen, were connected via a controller. The semi-automatic microscope had a programmable stage and shutter systems to allow long term observation of biological specimen. It was capable to image with a cooled 2 megapixel black/white camera in transmission mode (brightfield, phase contrast Ph, differential interference contrast DIC) and in reflection mode (brightfield, DIC, fluorescence). A variety of objectives (all Nikon, Tokyo, Japan) were used to image large areas (4x Ph0, 10x Ph1) and at higher magnifications with high flexibility because of the objectives long working distance and correction rings (20x Ph1 ELWD, 40x Ph2 ELWD, both 0 to 2mm glass). A high magnification objective (100x, NA = 0.9) was especially useful to investigate dry samples with high resolution. A second incubator setup was build for an upright Nikon microscope 90i in order to investigate biological specimen on non transparent samples (Figure 31).

This microscope, equipped with a cooled 5 megapixel color camera was fully automated. Also this setup, comprising the same objectives as the inverted, was operated in brightfield, phase contrast, DIC and fluorescence imaging mode.

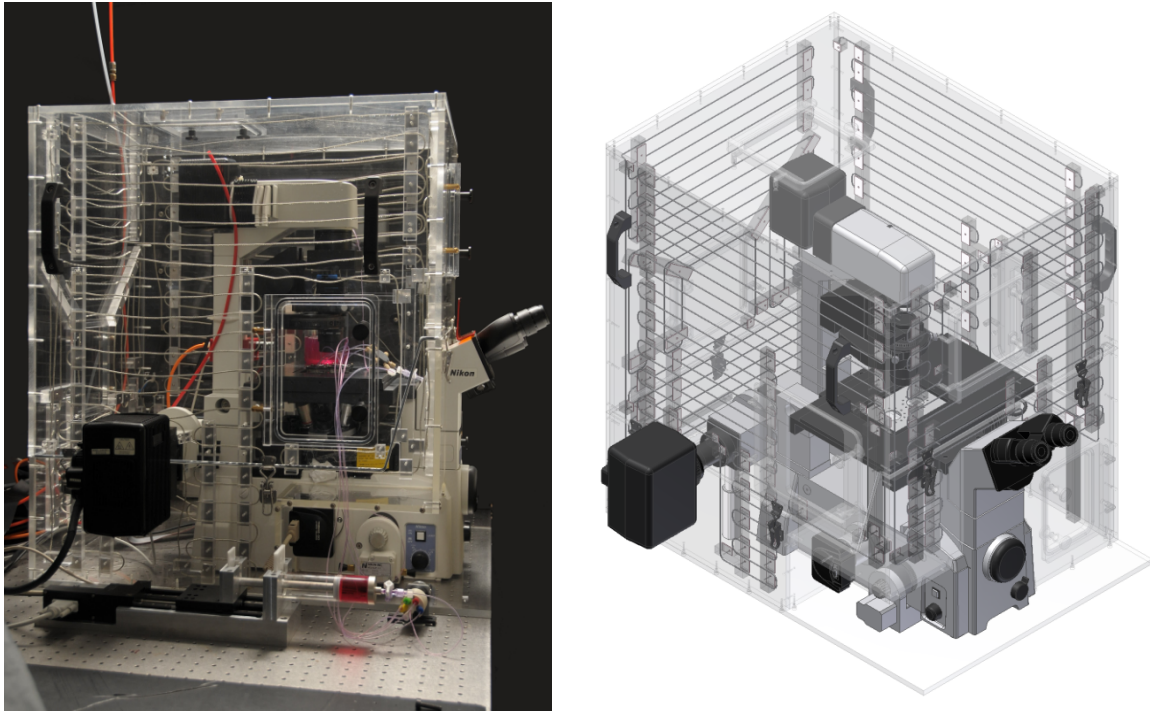


Figure 30: Photograph of TE-2000 incubation microscope (left) and the corresponding CAD scheme (right). Major parts of the microscope is enclosed by the incubator

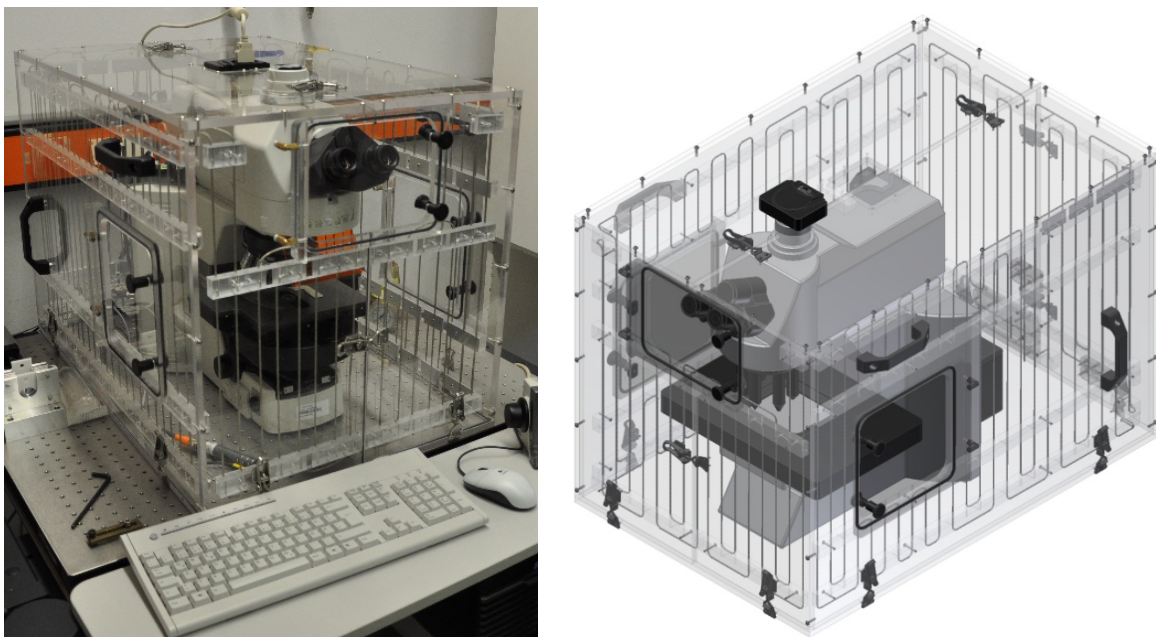


Figure 31: Photograph of 90i incubation microscope (left) and the corresponding CAD scheme (right). The whole microscope, except the camera, is enclosed by the incubator.

### 3.2.5 Scanning electron microscopy

SEM is a widespread technique to analyze topography and material composition of surfaces [185]. In principal, an image is obtained by detecting the interaction of a focused electron beam with the surface of the analyzed object. In comparison to common light microscopy, the resolution is increased by a factor of  $\sim 1000$ , enabling the visualization of features on the nanometer scale. Detection limitations, e.g. spatial resolution  $r$  of different microscopy techniques, are linked to the wavelength  $\lambda$  of the incident beam via the lens specific numerical aperture  $NA$  which is shown in equation (17). It is determined by the opening angle  $\alpha$  of the lens and the refractive index of the medium  $n$  (18). In SEM electrons are used instead of photons for imaging which takes the advantages of the de Broglie relation (19) ( $h$ : Planck constant;  $p$ : momentum;  $E_e$ : electron energy;  $m_e$ : electron mass).

$$\delta = \frac{0.61 \lambda}{NA} \quad (17)$$

$$NA = n \cdot \sin \alpha \quad (18)$$

$$\lambda = \frac{h}{p} = \frac{h}{\sqrt{2m_e E_e}} \quad (19)$$

This implies a resolution of 0.02 nm by using reasonable values for a field emission gun of 100 kV electrons ( $\lambda = 0.0037$  nm) and  $\alpha = 0.1$  rad, which is far below the wavelengths applied in light microscopy. Although the use of electrons for imaging does not limit the resolution in theory, the spherical aberration limits the resolution in praxis. It is nowadays possible to resolve objects with commercially available microscopes which are below 1nm in size.

SEM works with conductive specimen inside a high vacuum chamber. The main components of the SEM are electron gun, optics, measurement chamber and detector & electronics.

The electron gun consists of a cathode that emits electrons which are accelerated towards the anode. The emission can be excited either thermally (thermionic emission) or by applying high voltage (field emission). The most common cathodes are working on thermionic emission principle and consist of a tungsten filament (W) or a lanthanum hexaboride (LaB<sub>6</sub>) tip. These materials are heated until the minimum energy for electron emission is reached. The advantage of this method is the relatively low operating vacuum needed. Disadvantages are the short lifetime of the filament/tip and the high emission energy distribution.

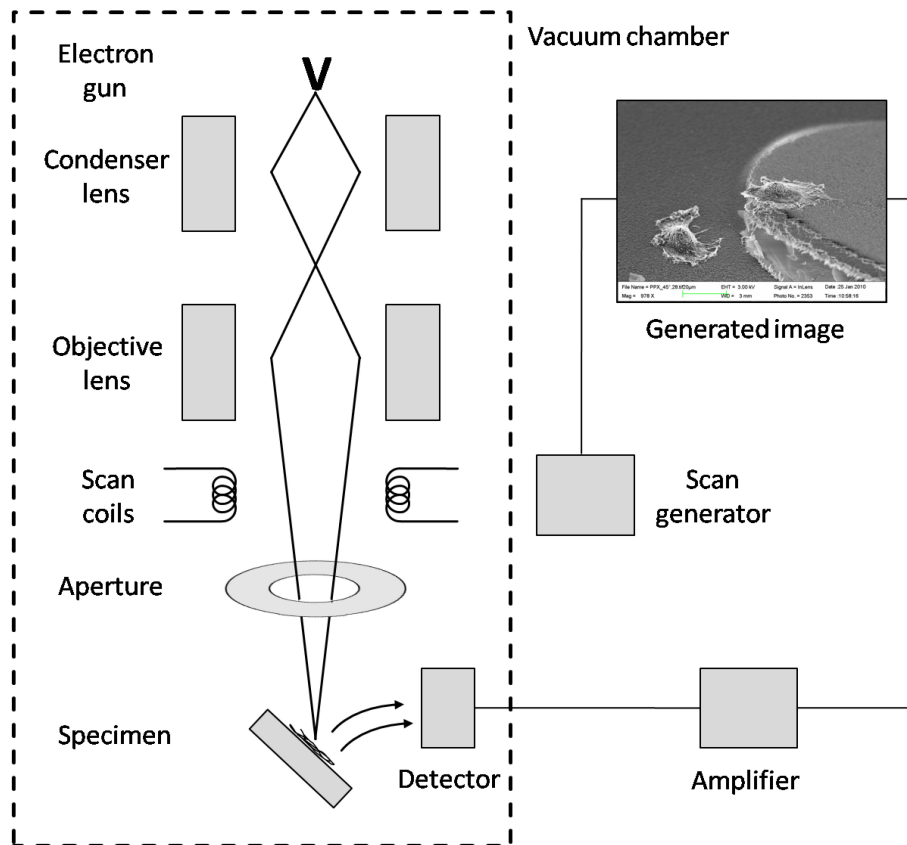


Figure 32: Schematic setup of a SEM. Image was adapted from [185].

The optical components of a SEM are the lens system, aperture and scanning coils (Figure 32). The lens system in the column focuses the electron beam and corrects symmetric defects of the beam with respect to the optical axis. The aperture limits the current density, the scanning coils raster the region of interest on the surface.

Specimen, sample holder, mechanic steering devices, and detectors are located in the measurement chamber. While the electron source is always kept under high vacuum the measurement chamber can be purged with nitrogen to allow sample exchange under ambient conditions.

Different detector designs are available to collect back-scattered electrons (BE) or secondary electrons (SE) which generate different contrasts due to their interaction depth with the material (Figure 33). A common SE detector for gaining a topographic contrast and high spatial resolution is the Everhart-Thornley detector. It attracts SE and BE through applying a positive voltage. Due to an applied bias voltage of +10 kV at the aluminum layer on the scintillator, the collected electrons are accelerated, penetrate the metal layer and create electron-hole-pairs in the scintillation layer. A fraction of the hole-pair recombination process yields a photon. The photons are emitted on a photo cathode where again an electron is created which is amplified by a photomultiplier to result in the obtained signal. The BE detector collects only back-scattered electrons from the sample. Electron scattering depends on atomic number  $Z$  and therefore yields material contrast.

There are scintillator, solid state and trough-the-lens detectors available. To combine imaging and elemental analysis EDX (Energy Dispersive X-ray) or WDX (Wavelength Dispersive X-ray) detectors are used which collect and analyze energy or wavelength of the emitted characteristic X-rays. The microscope used in this work is a LEO 1530 from Zeiss (Oberkochen, Germany).

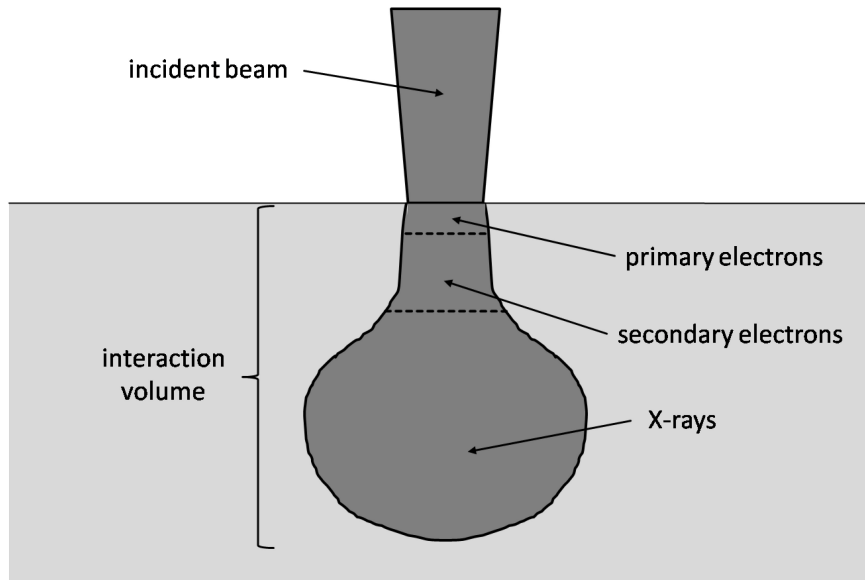


Figure 33: Scheme of an electron beam interacting with material. The interaction volume can be divided into three regions. Close to the surface high energy primary electrons are backscattered. In the middle region secondary electrons are emitted. Most X-rays are emitted from the lower region and do not serve for imaging but for elemental analysis. Inspired by [185].

## **4 Microfluidic shear force setup**

Since the development of soft lithography [186] microfluidic techniques have become widely spread in the area of biophysical and biomedical research [187 - 189]. Rapid prototyping - using visible light and a photomask - followed by the replica molding technique is a straightforward procedure which yields inexpensive structures in polymeric materials like poly-dimethylsiloxane (PDMS) [190]. The motivation for the use of microfluidics in biotechnology origins is the need for low material consumption [191], a controlled environment e.g. mimicking blood flow in veins, and multistep analysis in a single experiment [192].

In literature different techniques for the measurement of cell adhesion strength are described and compared [105; 193] (see chapter 2.5). The big advantage of using microfluidics over spinning disc [127], centrifugation assays [194] or using a cantilever [122; 195] is that cell adhesion strength can be determined quantitatively and be visualized at the same time. Even though the principle of the microfluidic setup appears rather simple, only a handful of basic commercial systems with very limited applications have been established yet. In general, the channel design has to be customized in order to meet the scientist's specific demands.

In this work the setup had to meet rather challenging demands with respect to application flexibility, range of force application and robustness respectively.

### **4.1 Demands on the setup**

The setup had to be capable of monitoring the cell detachment visually for single cells and cell populations in order to obtain qualitative and quantitative information on cell adhesion. Both suspension cells types, which adhere only weakly, and spreading cell types, which show much stronger adhesion strength after long term incubation, had to be investigated. Therefore cell adhesion strength had to be measured across a wide range which needed force application over several orders of magnitude. Also, incubation time for the cells had to be high enough to guarantee the cells full adaption to the environment without suffering from toxic effects of the environment. Finally, cell adhesion had to be determined on a large variety of functionalized surface types which were partially synthesized by collaborators around the world. Therefore design for substrate standards are needed which satisfied most of the scientists needs. Also a self reference method for the technique had to be realized in order to compare the cell adhesion measurements and to draw conclusions from the variety of surfaces.

Summarized, the key criteria are quantitative cell adhesion measurement of a long term incubated cell population with a high reproducibility while at the same time the cells had to be observed. The surface had to be exchangeable and a generalized protocol had to be established.

## 4.2 Microfluidic device

First the appropriate technique to measure cell adhesion strength was chosen. A microscopy technique was necessary to observe both cell adhesion process and cell detachment *in situ*. Only AFM, radial plate and parallel plate flow chambers were capable to match this demand. AFM also meets the need to apply forces on a wide range which is not possible for the radial plate flow chamber (see chapter 2.5), but AFM is suitable to measure cell adhesion on single cells only. Thus, only the parallel plate flow chamber design could fulfill the demands of simulations application of high forces to a large number of cells.

The flow channel (see chapter 4.2.1) was designed with an exchangeable bottom to fit *ex situ* prepared surfaces with lateral length of  $25\text{ mm} \pm 5\text{ mm}$ , which is the edge length of a standard microscopy slide cut into three equal pieces. In order to measure the high adhesion strength of adherent cells in this design, the channel height was kept relatively low while the aspect ratio of channel width to height was kept high in order establish a laminar flow (see chapter 2.5.3).

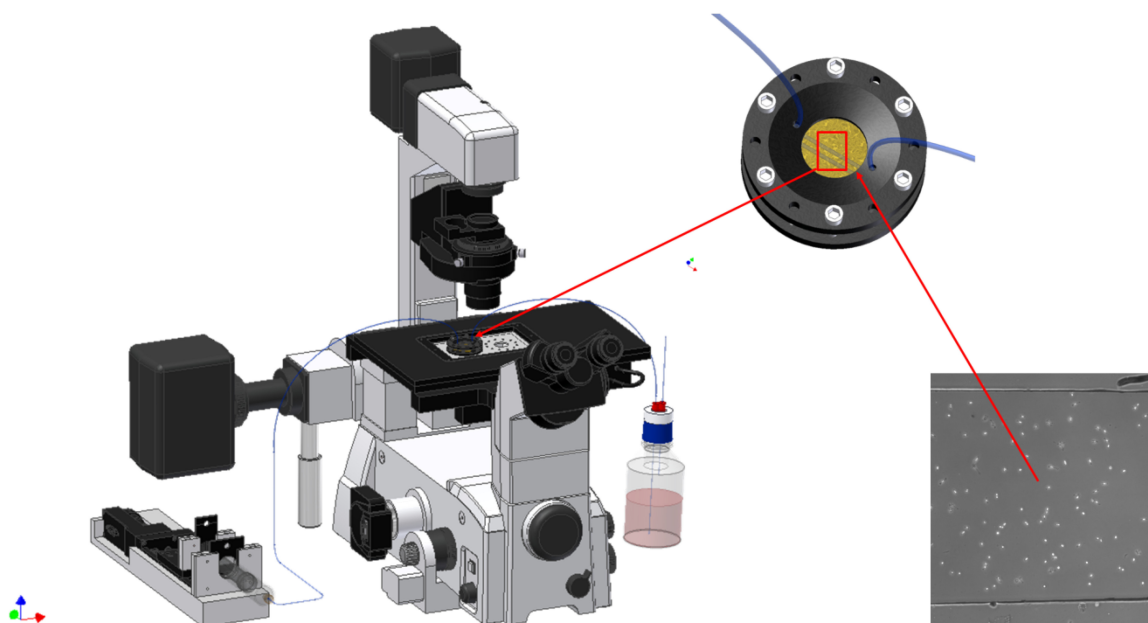


Figure 34: Scheme of microfluidic shear force setup. A channel system placed on a microscope was connected to a liquid reservoir at the inlet and a syringe pump at the outlet. Cells were cultured inside the channel.

The channel system was connected via tubing to a custom build programmable syringe pump which was capable to apply flow in the range of six orders of magnitudes. On the counter side the channel was connected to a pressurized liquid reservoir. The overpressure assisted the pulling syringe pump at high flow rates. The channel system was mounted inside the light microscope TE-2000 (Figure 34). The microscope was enclosed by a

custom built incubator (Figure 30) with control of temperature and CO<sub>2</sub> atmosphere (see also chapter 3.2.4), which allowed long term cell incubation. The channel walls and the tubing consisted of a gas permeable material to allow gas exchange.

In order to compensate biological variability a set of surface samples were investigated with the same cell population. In order to do so, the channel system was parallelized (Figure 35).

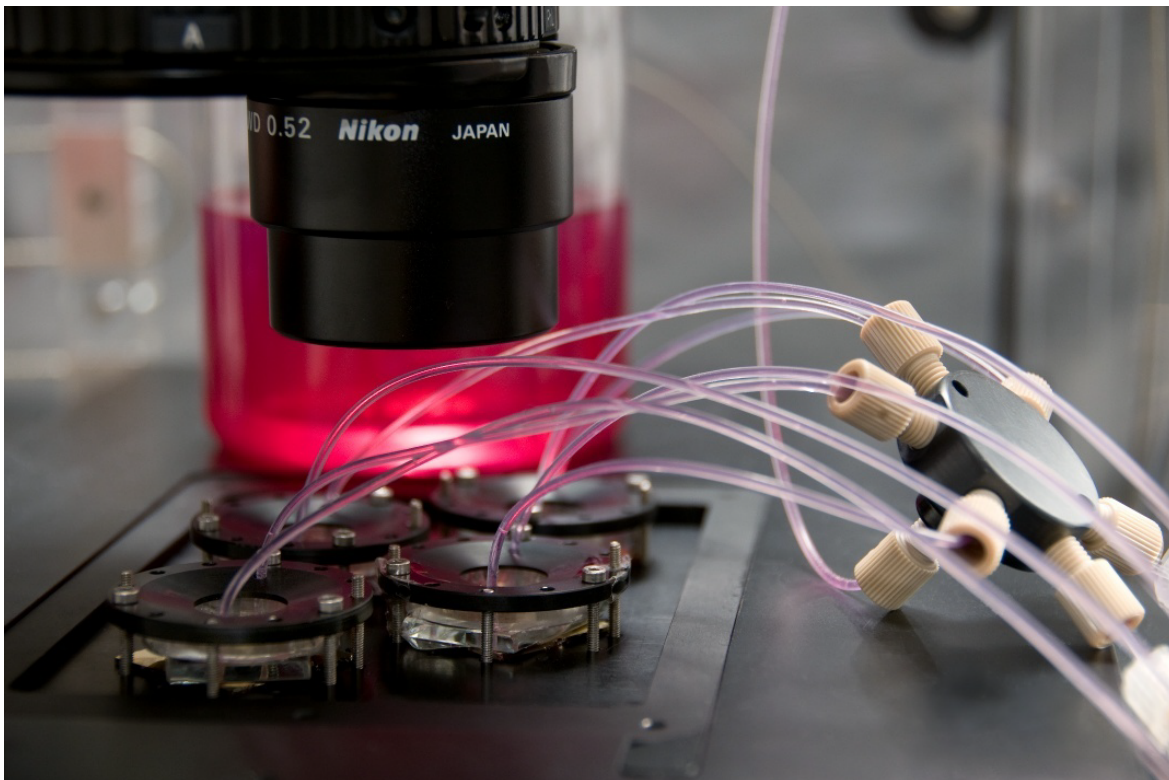


Figure 35: Photo of a multichannel platform to perform consecutive flow channel experiments. In each channel a different substrate was measured to compare surface properties towards cell adhesion directly.

#### 4.2.1 The parallel plate flow channel

The channel consisted of a gas permeable PDMS gasket which was sealed by the upper glass slide and the substrate of interest at the bottom (Figure 36). For liquid inlet and outlet two 1mm wide holes in the distance of 24 mm were drilled through a 30 mm x 20 mm and 2 mm thick float glass lid with a diamond tip drill. For a tight connection a 1/16" (1.56 mm) polyfluoroalkoxy tubing was interconnected through 1.2 mm holes of a 4 mm thick PDMS polymer ring [196] which was glued on top of the glass lid with Pattex commercial silicone adhesive.

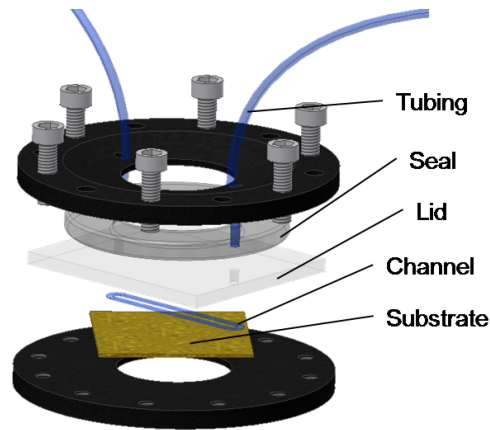


Figure 36: Scheme of microfluidic channel sandwich construction. The upper parts were assembled and the substrate was mounted directly before the experiment only.

The channel was made of PDMS cast in a polished micro machined brass mold and cured at 65 °C for 16 h (Figure 37). The mold defines the channel dimensions to be 25 mm x 1.5 mm x 0.14 mm and a wall thickness of 1 mm.

The channel was aligned on the glass lid as described in chapter 4.3.1 in detail (see also Figure 40). After placing the substrate with a approximate size of 25 mm x 25 mm diagonal to the expected channel orientation, the channel system was kept together by an upper windowed 3 mm thick aluminum or PMMA discs and M2 screws and a 5 mm thick windowed aluminum platform at the bottom, as seen in Figure 35, both with a hole diameter of 20 mm. In contrast to PDMS microchannels sealed chemically to glass, this system allows a ten-fold higher flow without leakage. For the parallel channel setup the top discs are mounted on a multi windowed platform.

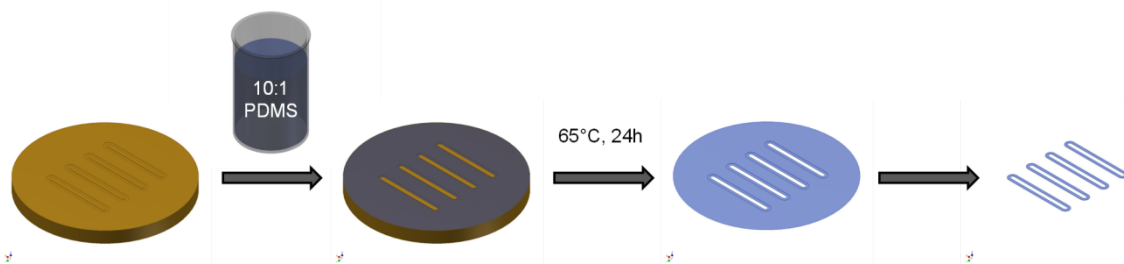


Figure 37: Scheme of replica molding technique. A micromachined and polished brass mold was used to cast PDMS polymer and cure the polymer at 65 °C overnight. Afterwards the channels are peeled off.

### 4.2.2 Flow control

Commonly, thermal drift and pressure instabilities cause major problems in microfluidic devices. Small leaks can cause a continuous flow due to the capillary effect which then

have, like temperature gradients, a major impact at that scale of microfluidics. Hence, specific arrangements were made to maintain reproducible conditions.

To overcome the thermal convection the incubator was heated to 25 °C for experiments which were designed for room temperature. That way the liquid reservoir and most of the tubing stayed at constant temperature. Stronger microflows arose from pressure instabilities. Therefore the liquid reservoir was pressurized with nitrogen to around 500 mbar using a back regulated high precision gas metering valve (Pressluft Götz, Mannheim, Germany). The overpressure did not only stabilize the flow but also supports the syringe pump, so that the CO<sub>2</sub> saturated cell culture media did not degas at high liquid flows when the drag of the syringe pump overcame the pressure drop along the flow path. A specific fluid system was developed in order to parallelize the channel setup (Figure 38). A manifold connector (e) served as a liquid distributor from the reservoir to the channels and as an interface for sample injection (f) into the channels. The selection valve (b) was located between the parallel plate flow channels (c) and the syringe pump (a). Each position on the valve selector opened the flow path to the syringe for one channel only. One tube ran from the manifold as a “by-pass” directly to the selection valve. During experimental incubation periods the “by-pass” was opened to the system to equilibrate the channel system and thus to avoid microflows.

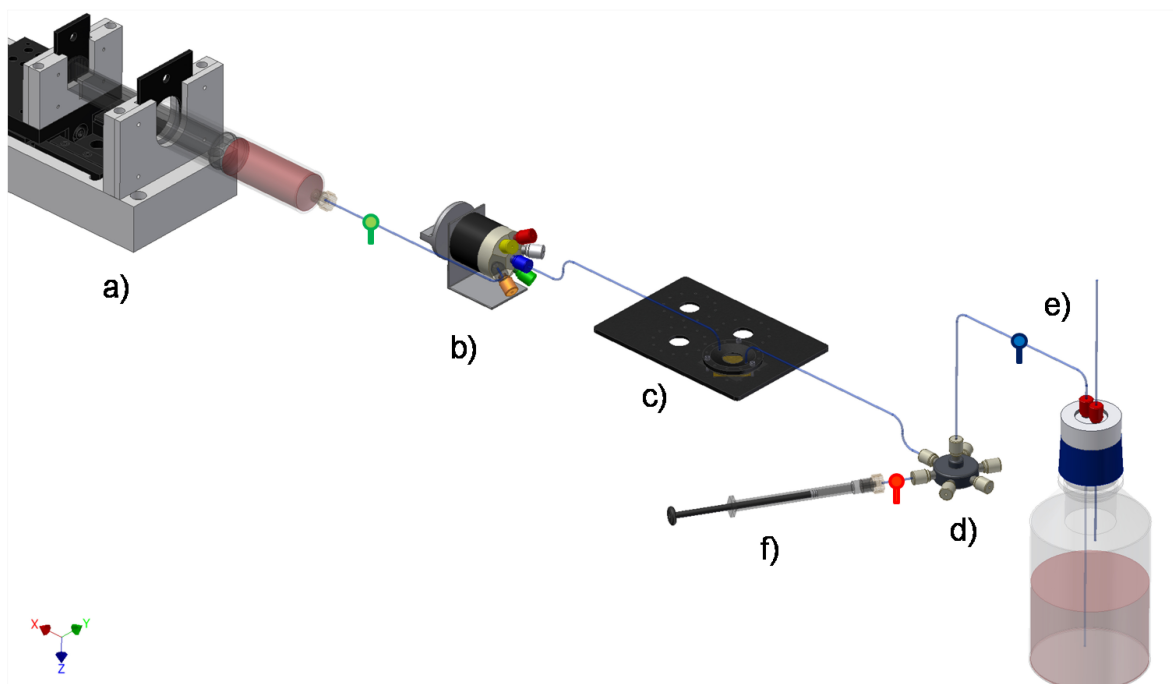


Figure 38: Scheme of the fluidic system, exemplary for one channel. The liquid was sucked by the syringe pump (a) from the pressurized reservoir (e) through the manifold (d), the channel (c) and the selection valve (b). The valve selects the pathway for one channel at a time. The manifold also serves for specimen injection (f). For clearance the schematic T-connectors between syringe/selector, manifold/reservoir and manifold/injector are color coded.

During the experiment the flow was controlled by the syringe pump. A custom build pump uses a M.403-4DG translation table from PI Instruments (Karlsruhe, Germany) as its base. A syringe attachment system is mounted on top. Two plastic wedges (see Figure 38a) assured that the syringe are mounted firmly so that minimal movement of the translation stage was conducted to the syringe. The translation stage then is controlled by the software Micromove® available from the translation stage distributor. An interface for macros was used to enter the flow program. The table speed and hence the volume flow was increased exponentially with time to cover up to six orders of magnitude in volume flow (Figure 39). The dwell time for each step was varied and hence the shear rate and overall time of the experiment was changed.

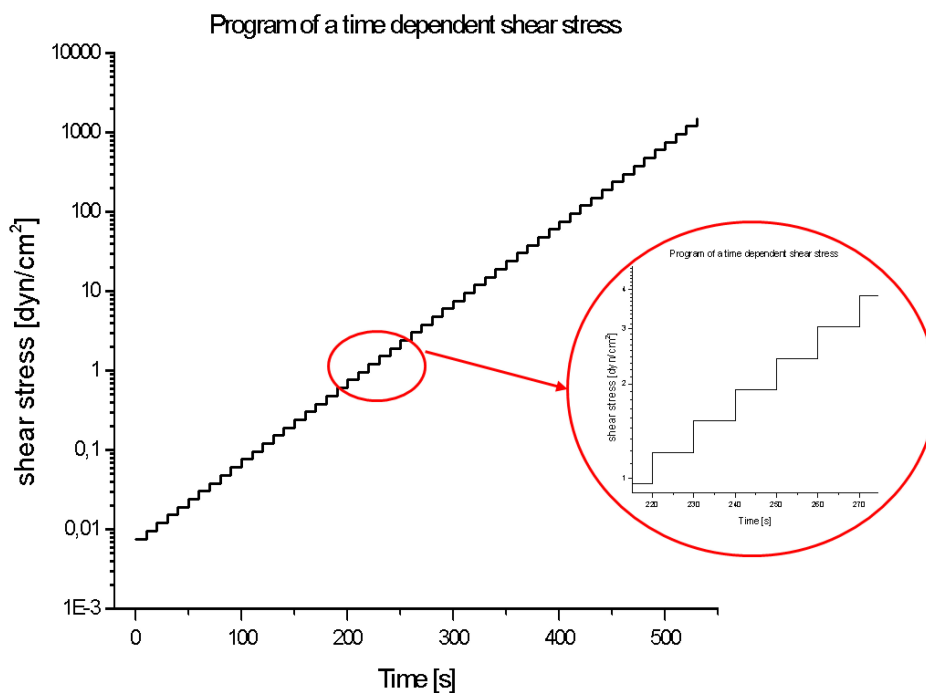


Figure 39: Flow profile for a cell detachment assay. The flow was increased every time interval by 25.9 % which resulted in 10 steps covering one order of magnitude in shear stress. Here the dwell time is 10 s.

### 4.3 Microfluidic shear force assay

A couple of microfluidic shear force assays (see chapter 2.5) to measure cell adhesion strength in a parallel plate flow channel have been described in literature yet [105; 140; 197]. These assays use a stepwise linear increased shear stress approach to determine the cell adhesion strength. In the most setups, a small number of steps and long dwell times are reported. This makes it rather difficult to determine cell adhesion strength because an initial guess or multiple experimental runs have to reveal the shear force range where cell detachment occurs.

In this section a shear force assay is presented which reveals cell adhesion strength of weak to strong adherent cells in one run by increasing the shear stress in a short time exponentially over six orders of magnitude.

### 4.3.1 Preparation of the channel system

The channel system was rinsed with Milli-Q water and iso-propanol to get rid of polar and apolar residues. Then the system was kept in 50 % p.a. iso-propanol over night. A final rinsing step with 50 % p.a. iso-propanol was followed by purging the system with nitrogen. At the same time the PDMS channels were rinsed with Milli-Q water and iso-propanol. Then the channels were immersed in 2 % Extran solution for 30 min, kept in Milli-Q water over night and 30 min in iso-propanol to remove apolar residues. Before channel alignment the glass lid was cleaned with 2 % Extran, Milli-Q water and iso-propanol using dust free wipes. A droplet of ethanol on the lid and two blunt cannulas helped to adjust the PDMS channel (Figure 40). As soon as ethanol evaporated the channels stuck to the glass lid and were finally rinsed with Milli-Q water. A subsequent nitrogen stream (~100 mbar) removed the remaining water.

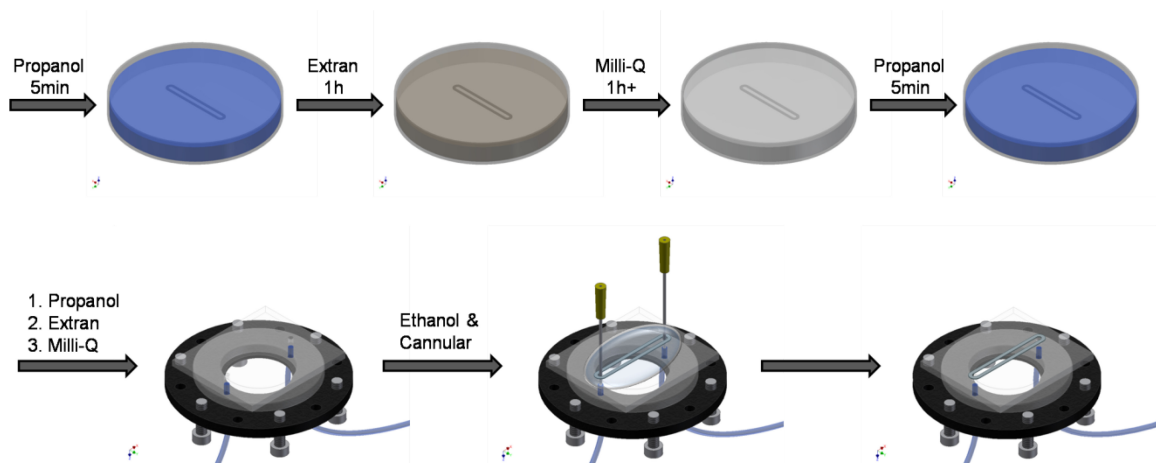


Figure 40: Scheme of channel cleaning and channel arrangement.

The pre-synthesized substrates were placed on the platform and the channel systems were mounted one by one. Mounting posts ensured correct alignment of the channel top. At least three screws were used for fixation – one closest to the inlet the others distributed symmetrically. To avoid channel leakage or breaking of the lid the screws are fastened alternately. As soon as the channel walls got visually transparent the channel was sealed tight.

The channel platform was put onto the microscopy table (Figure 35) and the tubing was fixed with adhesive tape to discriminate vibrations from the tubing when the table was moved. The syringe pump device was connected to the computer, started up and set on position. Then, the medium filled reservoir and the syringe with a T-connector were

connected via luer-lock adapters to the channel system. The “by pass” was switched open and 500 mbar overpressure was applied. The channels were rinsed one by one while the syringe was filled with medium. The syringe was then liberated from air bubbles and put into the pump device. If channel leakage occurred during experiment, it was at this step. Finally the center position of each channel was determined by imaging with a 4x PhL objective, stored and a reference image was taken to determine the channel width.

### **4.3.2 Conduction of the experiment**

Freshly harvested and pelletized cells (see 3.1.6) or beads were resuspended in 1mL culture medium. The flow path (Figure 38) from the reservoir was blocked (blue) and the outlet at the T-connector before the syringe pump (green) was opened. From the interface of the multifold connector (red) 200  $\mu$ l of the cell suspension was injected into each channel (c). The injection was followed by life imaging with the microscope. Then the outlet (green) was closed, the selection valve (b) put to the “by pass” position and the flow path from the reservoir (blue) unblocked. The pressure from the reservoir compressed the medium a little, resulting in a residual flow with the speed of 5  $\mu$ m/min to 10  $\mu$ m/min in the first 5 min inside the channels. During the hours of incubation one channel was observed using time lapse microscopy (one picture / minute). After incubation the microscopy stage was moved to the stored channel position. At a given magnification a movie recording with a rate of one frame per second (1 fps) was started. At the same time the flow program of the syringe pump was started. The valve position (a) to the corresponding channel was turned open directly afterwards. During the flow program the cell detachment took place (Figure 41). After the flow program was finished the movie recording was stopped and the valve closed. The syringe was emptied by opening the T-connector (green) and putting the pump device to the starting position. Then the “by pass” was opened and during 5 min pressure compensation was achieved. Then the next channel was measured.

After the last measurement the liquid reservoir was replaced by an empty one. Air was purged through all channels and the valve was closed. Using a 20x Ph1 objective each channel height was determined by focusing the channel top (lid) and the channel bottom (substrate) in air and measurement of the distance between both. Finally the channels were washed with MilliQ, iso-propanol and kept in MilliQ/iso-propanol according to chapter 4.3.1.

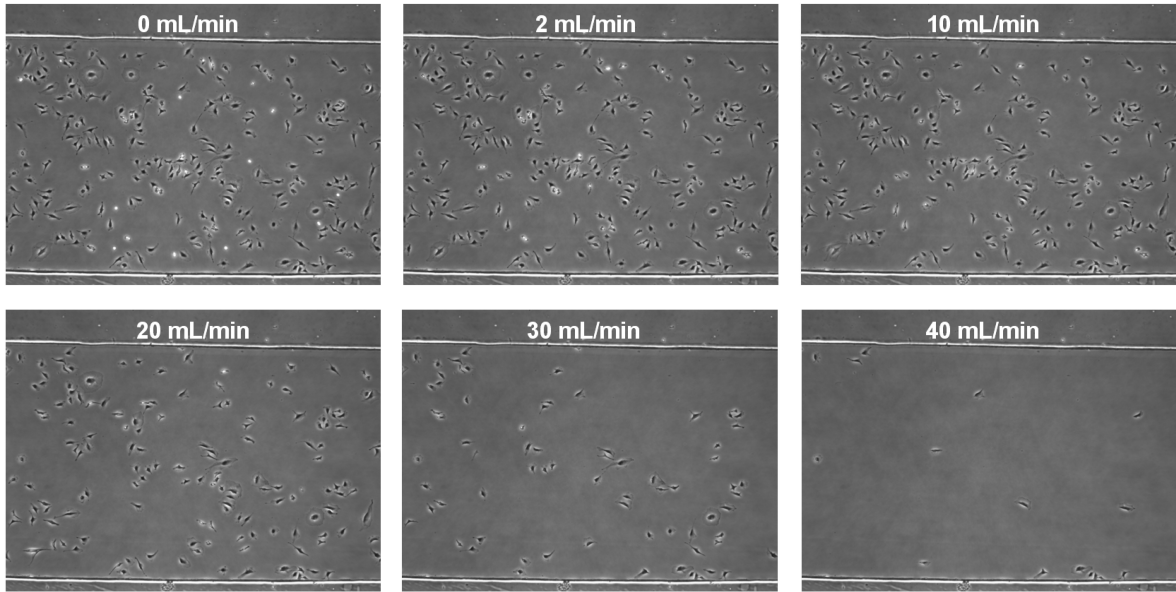


Figure 41: Time series of cells detached during the microfluidic shear force assay. Most cells detach in a narrow range of volume flow.

### 4.3.3 Evaluation of the experiment

The reason why cells detach from a substrate by a reasonably flow is the hydrodynamic shear force which is applied to the cell. A Poiseuille model for parallel plate flow channels describes the shear stress  $\tau$  generated onto the channel walls (see also 2.5.3) which causes the cells to detach from the substrate [198].

$$\tau = \frac{6Q\mu}{h^2w} \quad (20)$$

$Q$  is the flow rate,  $\mu$  the viscosity of the liquid,  $h$  the channel height and  $w$  the channel width. More complex 3D numerical simulations on cells in flow channels [140] showed a good agreement with the Poiseuille model. Gaver *et al.* solved a two-dimensional model computationally by the boundary element method which included the relative size of the cell towards the channel dimensions [199]. They found that maximum shear stress might be 2.95 times higher than the mean shear stress in parallel plate flow channels calculated by (20). Despite that Young *et al.* followed the Purday approximation [200] and present a detailed calculation [197] resulting a factor of 1.07 x as recalculated for the dimensions of the system presented here.

However, to calculate the applied shear stress the channel dimension need to be known. The channel height was measured after each experiment directly (see 4.3.2) and the channel width is determined from the image at center position (see 4.3.1). The viscosity of the medium depends on temperature and salt content. For 20 °C the viscosity of water is  $\mu = 1.00 \times 10^{-3} \text{ kg m}^{-1} \text{ s}^{-1}$  [201] but drops for 37 °C warm medium to  $\mu = 0.72 \times 10^{-3} \text{ kg m}^{-1} \text{ s}^{-1}$  [197]. The volume flow depended on time and increases exponentially which could be

displayed by equidistant points on a logarithmic scale (see 4.2.2). Knowing the program of the syringe pump the time of the cell detachment video (see 4.3.2) was assigned to the volume flow and hence to the shear stress.

That way, the number of cells determined at a reasonable time point in the video (Figure 41) was assigned to a specific  $Q$ . Volume flow  $Q$  was then directly correlated to a certain shear stress  $\tau$ . The cell count (around 300 cells) was then normalized to a cell fraction in order to compare experiments of different sets independent on the absolute cell seeding density. The normalization also worked as a self reference so surface types of different origin could be compared directly (see 4.1 “demands on the setup”). The fraction of cells, which were still on the substrate, was then plotted against shear stress  $\tau$ . The point on the graph where 50 % of the initially attached cells had come off (Figure 42a) marks the point the characteristic critical shear stress  $\tau_{50}$  is reached [127]. A second method was the application of a dose-response fit  $\{y = A_1 + (A_2 - A_1) / (1 + 10^{(\log x - x_0)p})\}$  fit to the detachment curve. After differentiation of the resulting model curve the maximum detachment rate / s of the cell fraction was determined as the peak in the differentiation curve (Figure 42b). Both methods obtain about the same  $\tau_{50}$  value. The difference in  $\tau_{50}$  of the two methods in this example is about 1.4 % (425.5 dyn/cm<sup>2</sup> vs. 419.5 dyn/cm<sup>2</sup>). The advantage of method I is a straight forward procedure and the result is expected to be more precise because no artificial data is generated and is thus used throughout this work. Method II is helpful in the case two or more populations with different adhesion strength have to be identified and evaluated separately, because after a higher order fit multiple maxima appear in the differentiated graph, which are then determined easily.

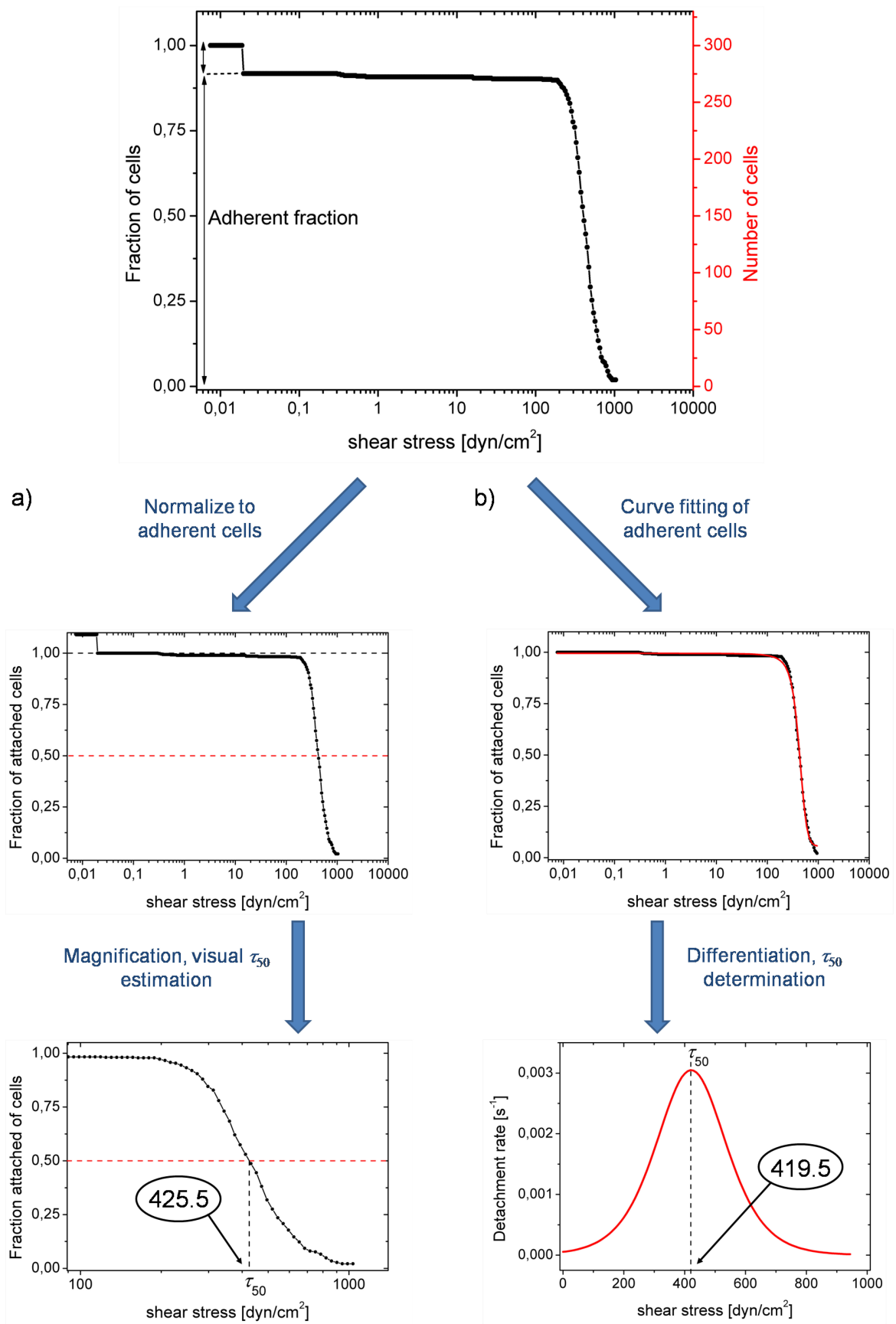


Figure 42: Determination of critical wall shear stress. (a) Method I describes a direct approach. (b) In method II first a curve fit is applied and then differentiation reveals the maximum detachment rate.

## 4.4 Performance of the shear force assay

Before performing the assay on biological systems the setup was characterized. Calculations and measurements of the flow profile were conducted. Model systems were used to investigate the performance, namely the robustness and the reproducibility of the setup. To circumvent uncertainties e.g. biological fluctuations or active cell response to the assay, microspheres were attached to well defined surfaces and the critical shear stress was determined. A second advantage of these test objects is the possibility to make proper calculations with the spherical shape of these particles and redirect the calculations to experimental values.

### 4.4.1 Flow characterization

In order to apply the formula (20) from the last chapter (see also 2.5.3) the liquid flow had to be laminar (7) and fully developed (9). For the present setup the channel was 1.5 mm x 0.14 mm x 25 mm ( $w \times h \times l$ ). The maximum applicable volume flow  $Q$  was 30 mL/min. The liquid density  $\rho$  was about 1 kg/L and the viscosity at least  $\mu = 0.72 \times 10^{-3} \text{ kg m}^{-1}\text{s}^{-1}$  (at 37 °C).

From these values the maximum Reynolds number calculates  $Re \approx 850$  which was far from the critical  $Re = 2300$ . The flow was fully developed after  $L_e \approx 9.1 \text{ mm}$  at maximum applicable flow. The observation window was right in the middle of the channel which was  $12.5 \text{ mm} \pm 1 \text{ mm}$  from the entrance and therefore in the region of fully developed flow. These calculations show that formula (20) can be applied confidently.

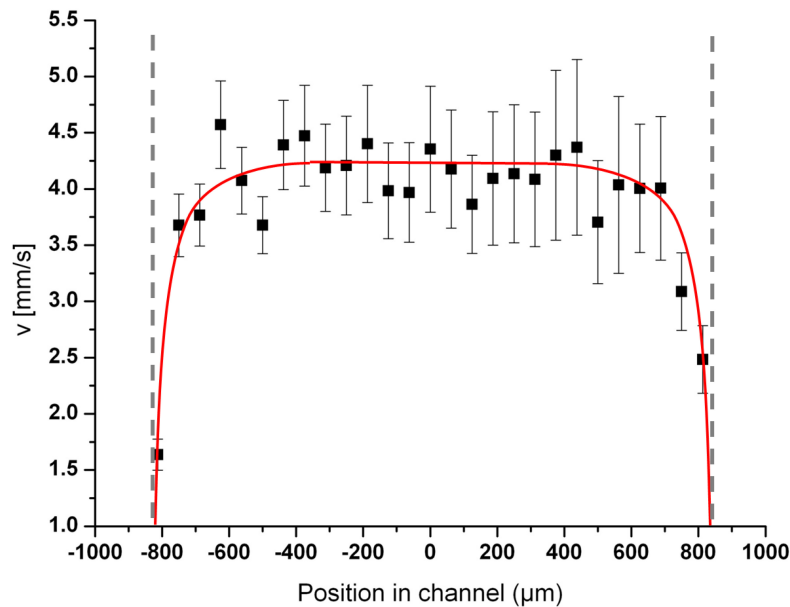


Figure 43: Flow profile measured with FCS method. The velocity in the middle of the channel is in agreement with the theoretical mean velocity.

Additionally, the flow profile was experimentally measured using Fluorescence Correlation Spectroscopy (FCS) in collaboration with Jessica Balbo from the group of Dr. Dirk Herten (Bioquant, Heidelberg University). The flow profile parallel to the surface (Figure 43) was measured in the middle of the channel height at a volume flow of  $64.7 \mu\text{L}/\text{min}$  ( $\sim 1.4 \text{ dyn}/\text{cm}^2$ ) resulting in a theoretical mean flow velocity of  $\sim 4.0 \text{ mm}/\text{s}$  ( $w = 1805 \mu\text{m}$ ;  $h = 152 \mu\text{m}$ ). The velocity of the main flow front as obtained from the FCS measurement was slightly higher ( $\sim 4.2 \text{ mm}/\text{s}$ ) than the calculated mean velocity, which was due to the parabolic shape of the flow profile itself and hence showed good agreement with the calculations. Furthermore, the flow profile showed the homogeneous velocity of the broad flow front and only 10 % of channel width close to each wall had to be discarded for data evaluation in the detachment experiment.

#### 4.4.2 Polystyrene microspheres on dodecanethiol SAMs

Channel to channel reproducibility was investigated by measuring the adhesion strength of polystyrene microspheres (PS-spheres) on alkanethiol (Figure 44). The adhesion strength was expected to be determined predominantly by hydrophobic interactions between PS-sphere and the SAM. Due to the hydrophobic effect between the apolar surface and the apolar sphere, water molecules are expelled between the sphere/substrate contact area, so the sphere adhesion is governed by capillary forces.

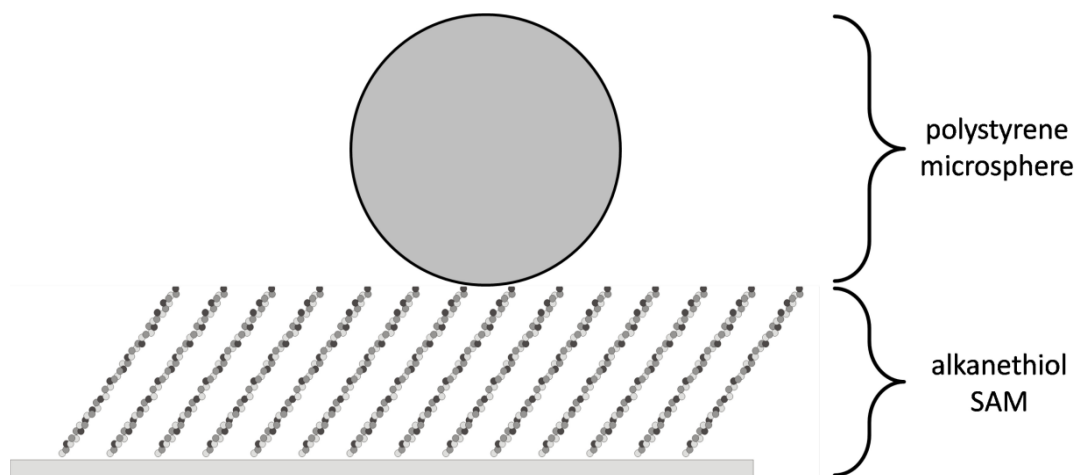


Figure 44: Scheme of polystyrene microsphere on C12-SAM. Capillary forces, caused by the hydrophobic effect, appear between apolar sphere and apolar surface and cause sphere adhesion.

PS-spheres ( $d_{\text{ia}} = 10 \mu\text{m}$ ) were diluted with PBS solution to  $2 \times 10^6 / \text{mL}$ . The particles were injected into all four parallel microfluidic channels each with a dodecanethiol SAM (C12) substrate. The C12-SAMs were synthesized prior *ex situ* (contact angle:  $103^\circ$ , film thickness:  $14\text{\AA}$ ) according to section 3.1.1 or *in situ* by injection of the dodecanethiol solution directly into the channel with the cleaned gold coated substrate. The PS-spheres,

around 600 in the field of view, were incubated for 5 min. Subsequently the detachment assay was conducted for each channel using PBS solution cooled to 10 °C. In a second set of experiments 30 °C warm PBS solution was used for PS-sphere detachment.

The detachment curves (Figure 45) were similar for all three channels at both temperatures. At 10 °C PS-spheres showed a critical shear stress  $\tau_{50}$  value of 369.0 dyn/cm<sup>2</sup> for channel-1, 387.5 dyn/cm<sup>2</sup> for channel-2 and 315.5 dyn/cm<sup>2</sup> for channel-3 respectively. The mean  $\tau_{50}$  was 357.3 dyn/cm<sup>2</sup> and the SD is  $\pm 37.4$  dyn/cm<sup>2</sup>, which was about 10.5 % of the mean value. For the 30 °C measurement the  $\tau_{50}$  values for channel1-3 were 201.5 dyn/cm<sup>2</sup>, 206.5 dyn/cm<sup>2</sup> and 224.0 dyn/cm<sup>2</sup> resulting in a mean value of 210.7 dyn/cm<sup>2</sup>. The standard deviation (SD) was  $\pm 11.8$  dyn/cm<sup>2</sup>, which was only about 5.6 % of the mean value. Thus, the reproducibility in adhesion strength measurement between the channels was very high. Also, a temperature dependent microsphere detachment was observed. The temperature dependence of viscosity already considered in the calculations ( $\mu_{10^\circ\text{C}} = 1.3 \times 10^{-3} \text{ kg m}^{-1}\text{s}^{-1}$ ,  $\mu_{30^\circ\text{C}} = 0.8 \times 10^{-3} \text{ kg m}^{-1}\text{s}^{-1}$ ), and revealed that adhesion strength of PS-spheres was 1.7 x higher at 10 °C compared to 30 °C. On the first sight the investigated system looked simple enough for running theoretical calculations on the sphere detachment in order to determine setup specific parameters. On a second sight it became evident that the strongest interactions between sphere and surface are of short range and in about the same order as the surface and sphere surface roughness which makes theoretical predictions complicated (personal communication with Prof. Alexander Pertsin, University of Heidelberg).

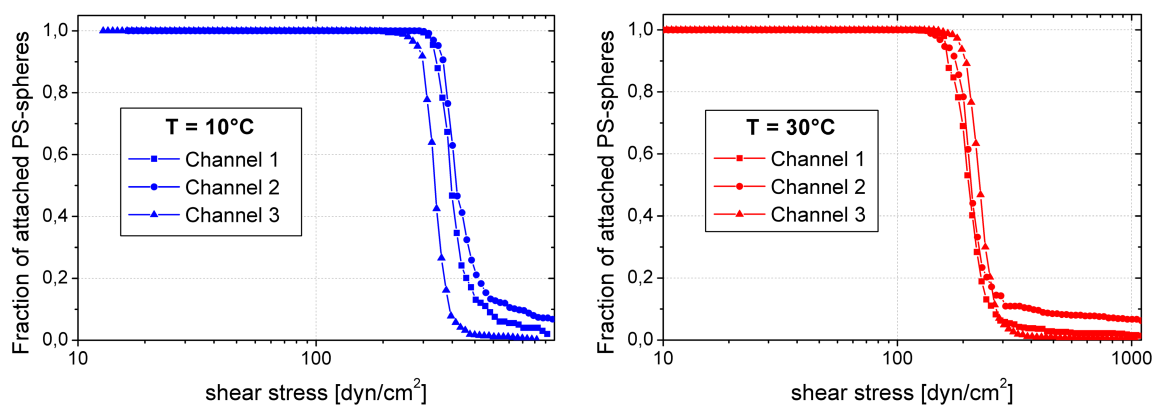


Figure 45: Detachment curves of 10  $\mu\text{m}$  PS-spheres on C12 in three different channels at 10 °C and 30 °C. The standard deviation for  $\tau_{50}$  was  $\sim 5\%$  to  $10\%$  of the total value. The total number of spheres counted in each experiment was 400 - 500.

#### 4.4.3 Streptavidin microspheres on biotinylated SAMs

In a next step a model system based on protein-ligand interactions was investigated. Protein-ligand interactions play a major role in cell adhesion (see chapter 2.1). A model system to investigate protein-ligand interactions is the binding between streptavidin and biotin (see

2.3.2). Determining the adhesion strength of streptavidin coated microspheres (streptaspheres) on biotinylated SAMs (Figure 46) might help to estimate force scales in which cell adhesion strength will occur.

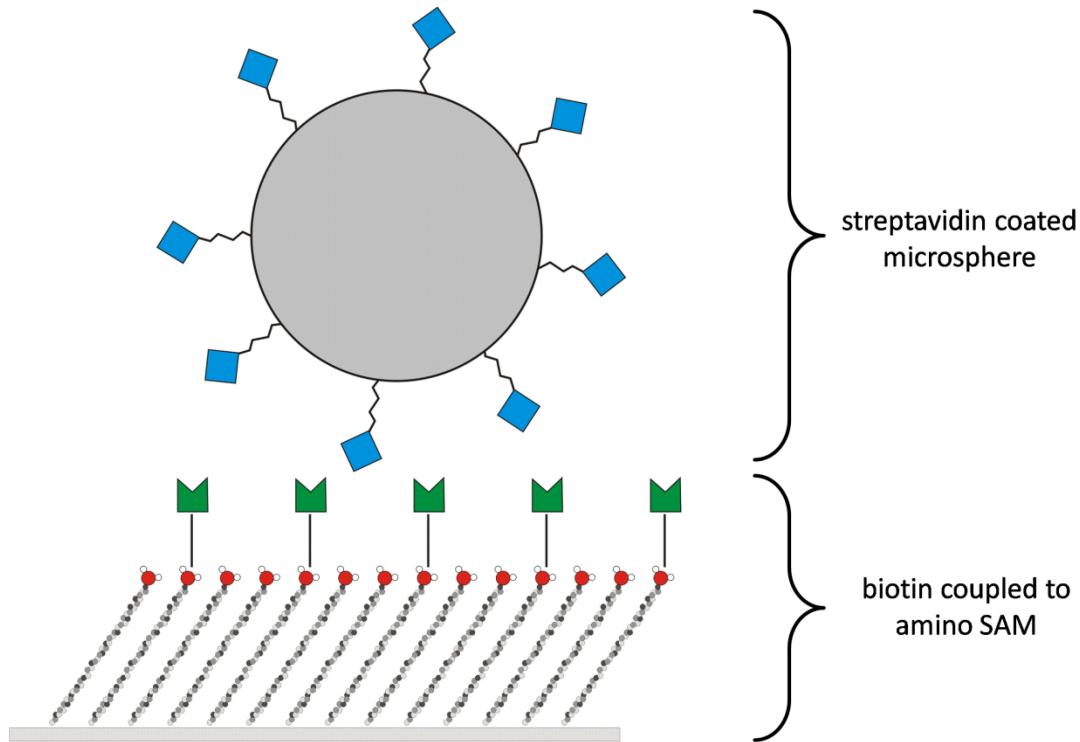


Figure 46: Scheme of streptavidin coated spheres on biotinylated AUDT-SAM.

Amino terminated SAMs were synthesized according to section 3.1.1 using ethanolic AUDT on 30 nm gold coated microscopy slides. NHS-biotin was dissolved in DMF and diluted with PBS to 10 mg/ml. The AUDT SAMs were immersed in the NHS-biotin for 30min and rinsed with PBS. Subsequently the samples were immersed in 0.1 % bovine serum albumin (BSA) in PBS for 1 h to block unspecific binding. A layer thickness on  $\sim 20 \text{ \AA}$  was measured for biotin, which was equal to  $\rho_{surface} \sim 1 \text{ molecule/nm}^2$ . The treatment with BSA resulted in additional  $\sim 40 \text{ \AA}$  layer thickness. The samples were rinsed with PBS and build into the channel system. The incubator was heated to physiological  $37 \text{ }^\circ\text{C}$ . PBS was then flushed through the channels and a suspension of commercial  $6\mu\text{m}$  strepta-spheres ( $\rho_{surface} \sim 0.01 \text{ molecule/nm}^2$ ), diluted in PBS to  $1 \times 10^6 / \text{mL}$ , was injected into the channels. The spheres bound within minutes to the substrate but incubation time was set to 1 h before performing the detachment experiment. Even after 24 h incubation the critical shear stress did not change significantly (data not shown).

The mean critical shear stress (Figure 47) was  $68.0 \text{ dyn/cm}^2 \pm 17.2 \text{ dyn/cm}^2$ , which is much lower than the adhesion strength for PS-spheres on C12-SAM (previous section). Also, the biotinylated substrates (here the biotin  $\rho_{surface}$  was  $\sim 0.1 \text{ molecule/nm}^2$ ) have been reused multiple times without losing performance (Figure 48) which indicated reversible

binding and detachment of the strepta-spheres to biotinylated SAM. Obviously the hydrophobic effect between a PS-sphere and a C12-SAM causes capillary forces between the sphere and the surface which are much stronger than the receptor ligand interaction between hydrophilic biotinylated SAM and the strepta-sphere.

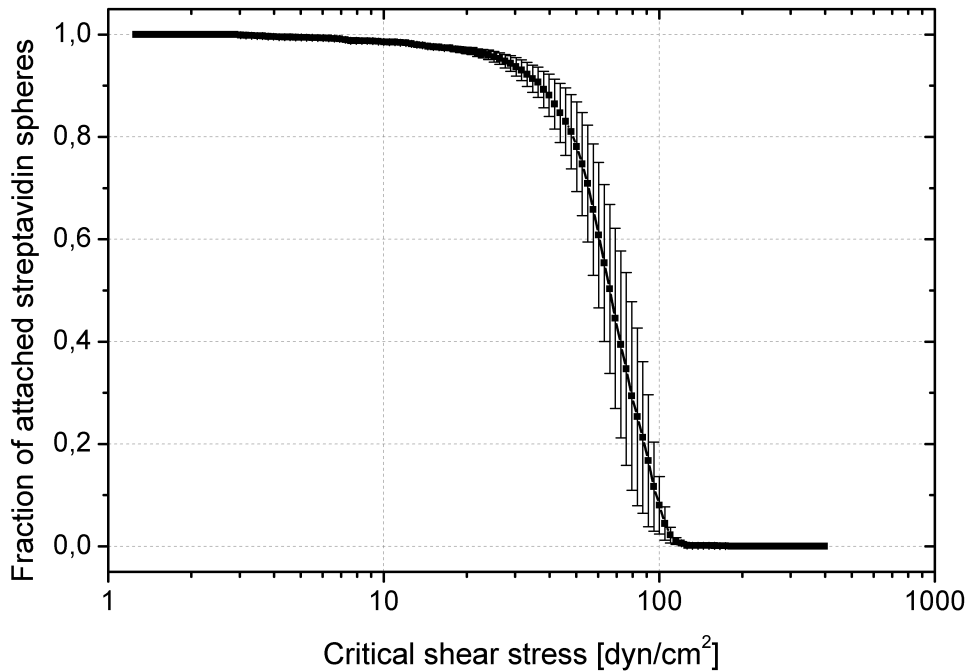


Figure 47: Mean detachment curve of 6µm streptavidin spheres on biotinylated AUDT-SAMs at 37 °C. Four experiments, each with ~ 1000 spheres, were conducted in different channels. Error bars indicate standard error of the mean.

The lower critical shear stress compared to the PS-sphere/C12-SAM system and the reversible particle binding supported the assumption of having pure protein/ligand interactions. As derived from Yago *et. al.* [202], the tethering force (assuming the same lever arm as for PSGL-1/L-selectin) of the streptavidin sphere with the radius  $R_s$  on the biotin substrate should be  $F_t = 13.2 \text{ pN} \cdot R_s^2 \cdot (\text{dyn/cm}^2 / \tau)$ . In this case  $F_t$  would be  $\sim 8080 \text{ pN}$ . The effective area  $A_{eff}$ , on which a sphere comes into close contact with a substrate can be estimated by  $A_{eff} = 2\pi \cdot D \cdot R_s$  [203]. The maximum binding distance  $D$  of the streptavidin/biotin complex was found to be 0.4 nm before unbinding occurs [51]. From that,  $A_{eff}$  is  $7.54 \cdot 10^{-15} \text{ m}^2$  which means that about  $N \sim 75$  streptavidin molecules may interact with comparably biotin saturated ( $N \sim 7500$  molecules) surface ( $N = A_{eff} \cdot \rho_{surface}$ ). Based on the assumption that one streptavidin binding site of each molecule had bound to one biotin the tethering force for a single bond is  $\sim 110 \text{ pN}$ . This value shows a considerably good agreement with AFM studies at 37 °C where biotin/avidin binding strength was found to be 70 pN [54], but assumes that all bonds between sphere and surface break at the same time. Anyhow, the good correlation between AFM and microfluidic measurement has to be regarded with caution. The binding strength in this

system strongly depends on the loading rate which is applied to break the bond [51]. This means that the bond has a distinct lifetime under a defined force and so the measured binding strength depends on the time the force is applied. This is known as the streptavidin-biotin paradox [52]. Nevertheless, the present experiment proofed the applicability of the microfluidic shear force assay towards adhesion strength measurement of protein-ligand interactions.

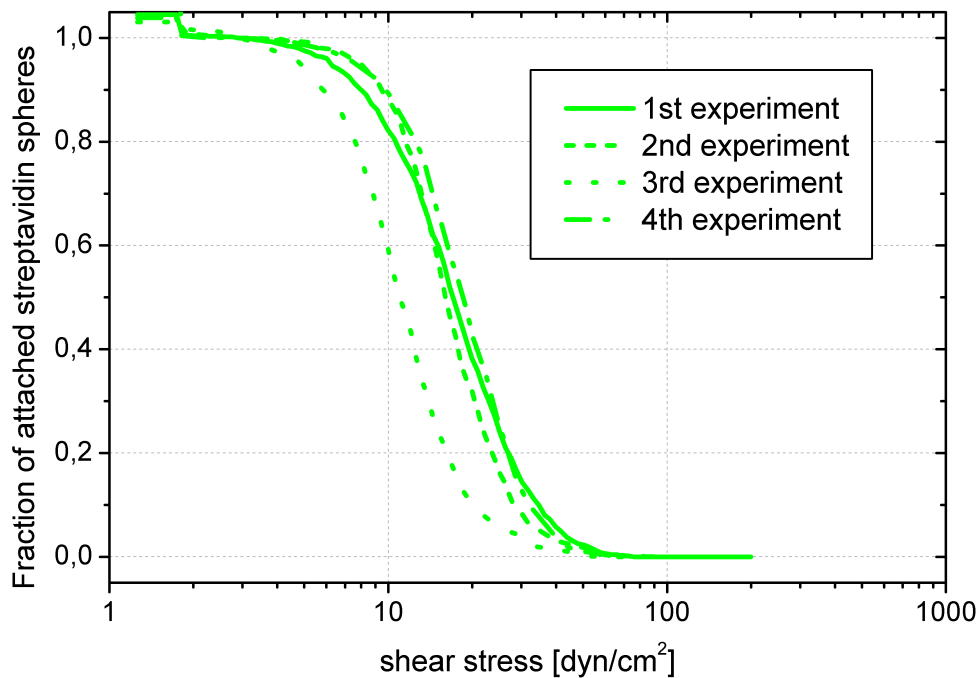


Figure 48: Detachment curves from repeated detachment experiments of 6  $\mu\text{m}$  streptavidin spheres ( $\sim 1000$  each) on biotinylated AUDT-SAMs. Repeated use of the biotinylated AUDT-SAM did not show loss of performance. Compared to Figure 47 adhesion strength was decreased because biotin density on the AUDT-SAM was only  $\sim 0.1$  molecule/ $\text{nm}^2$ .

## 4.5 Parameter optimization for adherent mammalian cells

In contrast to the presented model systems more precautions were needed when dealing with biological specimen. Parameters of the cell harvesting protocol, incubation time to allow cell adhesion and duration of the detachment assay were adjusted to establish reliable and reproducible measurements with the microfluidic shear force assay.

### 4.5.1 Harvesting protocol

A crucial parameter in the harvesting protocol of adherent cell culture was the confluence of the cells. If the degree of confluence in the culture dish was low, the membrane of single cells was extremely spread out and did not represent the native behavior. If the confluence was way above full coverage, meaning the cells had to move closer to each other to allow freshly divided cells to respread. In that case more prominent cell-cell contacts form and

the cell behavior changed as well. Especially fibroblasts are capable to these changes as these may further differentiate into different cell types [10]. This problem was circumvented using cultures with confluence of 90 – 105 %.

Another important aspect was the cell preparation. In order to collect the cells these had to be detached from the culture dish. Most commonly enzymatic reagents as trypsin are used to dissolve the ECM [204] and force the cells to round up. Under these conditions also the cells are damaged and treatment time has to be kept to a minimum.

Standard protocols were adapted and optimized (see 3.1.6). Still, in order to observe the impact of enzymatic treatment step towards cell adhesion, two ~ 95% confluent flasks of co-cultured REF52 were treated with 1mL 0.05 % trypsin/EDTA according to the protocol. In one flask the enzymatic process was quenched with 5 mL DMEM after 5 min in the other one after 8 min. Both cell suspensions were put into the centrifuge and pelletized. For the microfluidic shear force assay each cell pellet was resuspended and injected one fraction in each channel equipped with a glass substrate. After 3 h of incubation the shear force assay was conducted. The critical shear stress decreased from 290 dyn/cm<sup>2</sup> for 5 min trypsin/EDTA treated cells to 210 dyn/cm<sup>2</sup> for 8 min trypsin/EDTA treatment (Figure 49). Thus, the cell adhesion strength for 8 min treatment with trypsin/EDTA dropped to about 72.4 % of the correct 5 min incubation time. This experiment showed how accurate the harvesting protocol had to be followed in order to obtain reproducible results with mammalian fibroblasts.

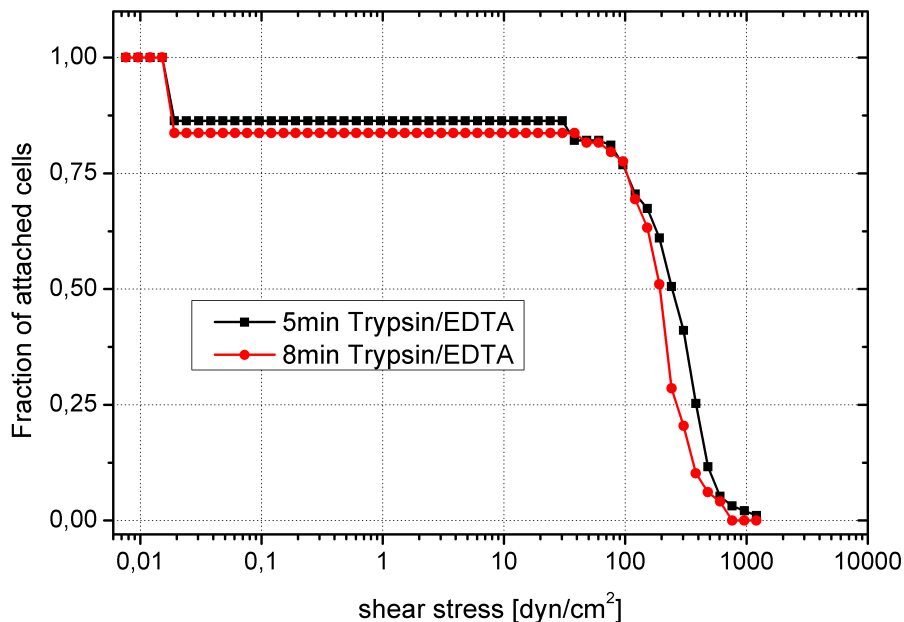


Figure 49: Cell adhesion strength of ~ 100 fibroblasts on glass in dependence of trypsin/EDTA incubation time. For treatment times longer (8 min) than suggested by the protocol (5 min) cell adhesion strength decreased.

### 4.5.2 Influence of in channel incubation time on cell adhesion strength

The adhesion strength of cells depends on the cell type and on the cell contact time with the surface. Thus, to perform the detachment assay the incubation time needed to be chosen carefully. The two concerns for adherent cells were that cells needed to be sufficiently spread in order to measure representative values for adhesion strength and to avoid already spread cells rounding up as it occurs during cell division. In the latter case adhesion strength of a subpopulation could have been affected which disturbs the result. In order to optimize the incubation time, cell detachment was measured after incubation of REF52 fibroblasts for 3 h, 4 h, 5 h and 6 h on polished glass (Figure 50). Glass represented an intermediate surface where cells spread well but the spreading takes longer compared to most lab plastic ware. As a result of the cell detachment assay, the critical shear stress for detachment nearly doubled from 447 dyn/cm<sup>2</sup> after 3h of incubation to 832 dyn/cm<sup>2</sup> at 6 h incubation time. The difference in critical shear stress between 5 h and 6 h incubation time was less than 10 % (775 dyn/cm<sup>2</sup> and 832 dyn/cm<sup>2</sup>, respectively), which indicated that the adhesion strength was barely changing after 5 h of in channel incubation. Inspection of the microscopy pictures confirmed that after 5 h incubation time the cells were mostly spread (Figure 51). Cell division on glass started after 7 h to 8 h of incubation which caused a certain fraction of cells to detach at low shear stress of about 10 dyn/cm<sup>2</sup>. Based on these findings, incubation for 5 h appeared to be optimal for the microfluidic assay with REF52 fibroblasts. However, this value needs to be redetermined if the cell type is changed.

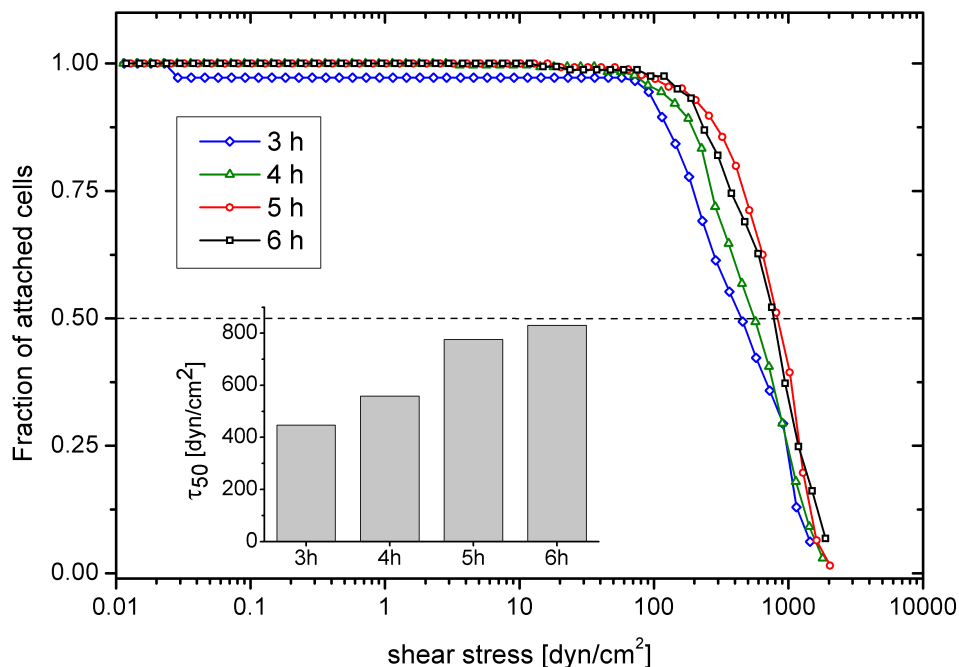


Figure 50: Fibroblast detachment assay for different in channel incubation times on polished glass. Each curve represents ~ 250 cells. Squares show data for 6 h, circles for 5 h, triangles for 4 h and diamonds for 3 h incubation time. The inset shows the critical shear stress at a linear ordinate.

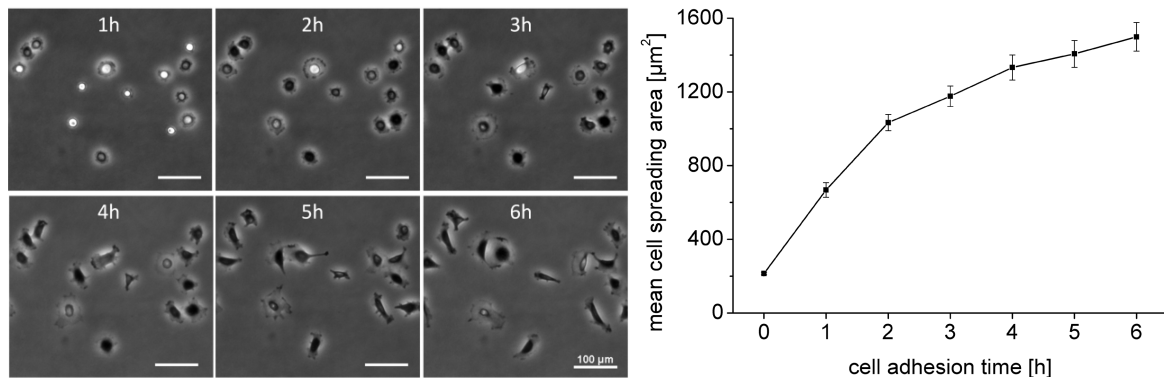


Figure 51: Images of cell spreading after 1 h to 6 h incubation. The graph shows that cell spreading barely improved after 4 h to 5 h.

### 4.5.3 Influence of detachment assay time on cell adhesion strength

Stimulating cells by an external shear force can induce a substantial growth of focal contacts [205206]. Temporal exposure of adherent cells to a fluid shear stress exerts a stimulus and thus modulates cellular signaling pathways and the expression of genes as reviewed by Li et al. [207]. This had an effect on multiple cell functions such as proliferation, apoptosis, migration, cell alignment and mechanical properties [207]. Spread endothelial cells e.g. elongate [208] and an alignment of stress fibers and microtubules along the axis is observed [209; 210]. This is accompanied by cytoskeleton reorganization and changes of the cell shapes [210]. In the present case, the duration of the shear force assay determined how long the cells were exposed to shear stress and hence the degree of cellular reorganization. Thus, the measured critical shear stress depended on the total experimental time. In order to assess this influence and to find the optimal experimental conditions, the influence of flow duration on the adhesion strength was investigated.

Therefore, the number of flow velocity steps in the detachment assay was kept constant but the dwell time was increased from 5 s to 10 s, 20 s and 40 s. This resulted in total experiment durations of 4.5 min, 9 min, 18 min and 36 min, respectively. The result for cells incubated for 5 h on polished glass is shown in Figure 52. The measured adhesion strength decreased with increasing flow duration from 646  $\text{dyn}/\text{cm}^2$  in the 4.5 min experiments and 438  $\text{dyn}/\text{cm}^2$  in the 10 min experiment to 244  $\text{dyn}/\text{cm}^2$  in the 18min experiment but increased to 316  $\text{dyn}/\text{cm}^2$  for the 36 min experiment. This was understood the way that cells respond to the flow by rearrangement of the cytoskeleton to optimize their hydrodynamic properties.

At a shear stress just prior to removal of the first cells ( $\sim 22 \text{ dyn}/\text{cm}^2$ , see also dotted line in Figure 52) the cell shape was investigated in closer detail (Figure 53a and b). In the case of the 4.5 min experimental duration the changes in the cell shape were marginal and the total cell adhesion area at 22  $\text{dyn}/\text{cm}^2$  was comparable to the cell adhesion area before the experiment (Figure 53b). In the 9 min experiment the cells started to contract and elongate during flow, while in the 18 min experiment some cells even started to round up.

Interestingly, in the 36 min experiment the cells elongated but barely rounded up. All morphological changes of the cells, i.e. elongation, contraction and rounding up, led to a detachment at comparably lower critical stresses. In the case of the longest, 36 min experiment, the cells have been exposed to the liquid flow for nearly 19 min until shear force of 22 dyn/cm<sup>2</sup> was reached (Figure 53a). The long duration of moderate flow seemed to be sufficient for the cells to adapt to the shear stress and reinforce adhesion so that the critical shear stress needed for its removal was larger compared to the 18 min experiment.

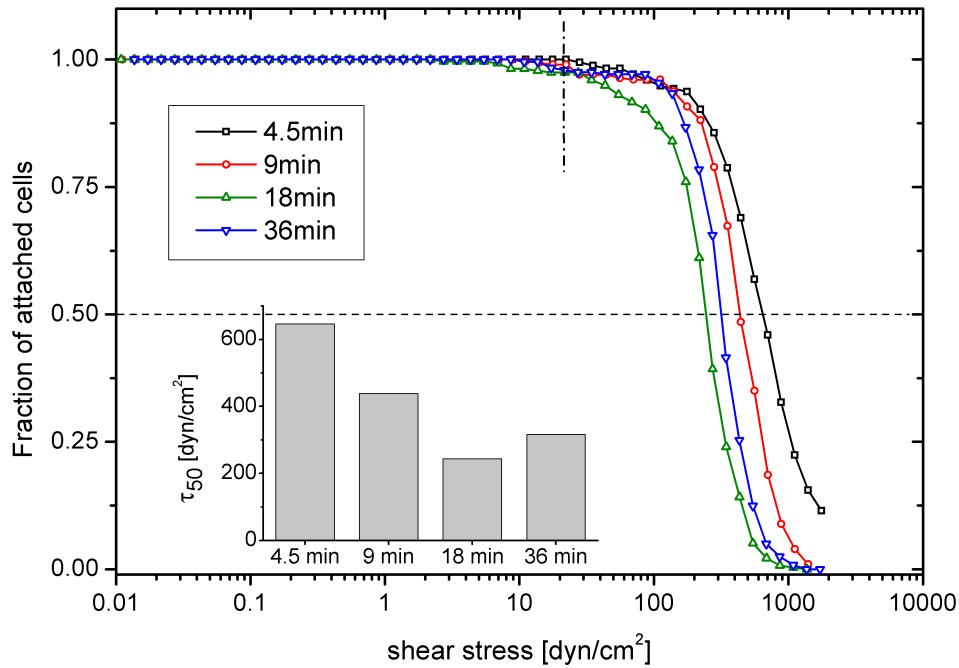


Figure 52: Cell detachment assay for different dwell times per volume flow step of 5 s (squares), 10 s (circles), 20 s (triangles) and 40 s (diamonds). The total duration of the detachment phase of the assay was 4.5 min, 9 min, 18 min, and 36 min, respectively. The total number of cells for each experiment is ~ 250. The inset shows the resulting critical shear stress on the glass substrates using a linear ordinate.

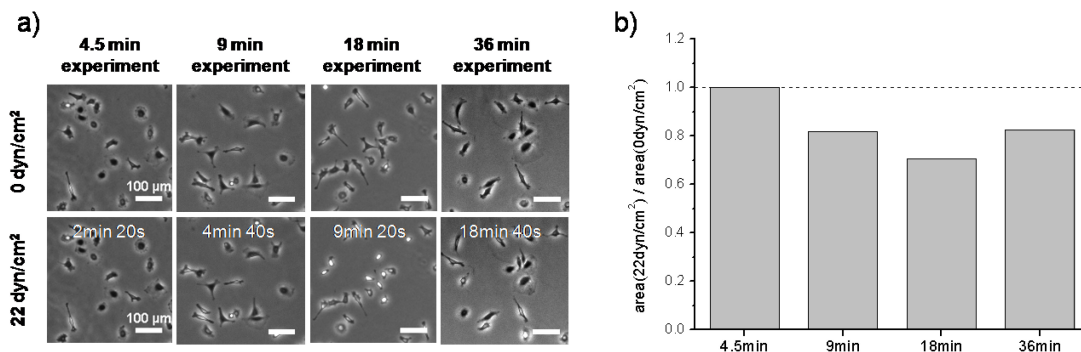


Figure 53: (a) Microscopy images of cells before applying microfluidic shear stress (upper images) and at a shear stress of 22 dyn/cm<sup>2</sup> (lower images) for the different dwell times (total experiment duration: 4.5 min, 9 min, 18 min and 36 min, respectively). (b) Cells barely responded in the 4.5 min experiment and tended to elongate and also round up towards longer experimental durations (18 min). Even longer experimental durations lead to similar attachment areas as for shorter experiments as cells adapted to the flow.

The involvement of continuous flow in cytoskeleton rearrangement was already observed before by Masuda et al.. Vascular endothelial cells exposed for 10min to a liquid flow of  $10 \text{ dyn/cm}^2$  developed additional lamellipodiae at the upstream rim [211]. Also the change of focal contacts due to the liquid flow is most likely to occur. In other studies, increased formation of microfilaments and enhanced growth of focal contacts at the upstream rim has been observed [210].

As the effect of flow induced reorganization of the cytoskeleton and focal contact formation was most likely to occur, the continuous flow effect in this setup was investigated in further detail. Again REF52 fibroblast cells were cultured in the microfluidic channel system for 5h and a constant flow was applied. In order to speed up the process and enhance the effect of cell rearrangement, EG2OH SAMs were used instead of glass. On EG2OH SAMs cells did not spread as well as on glass substrates and thus have a higher motility. Due to that the applied flow was chosen to result only in shear stress of  $0.1 \text{ dyn/cm}^2$ . As obvious from time lapse microscopy images (Figure 54) fibroblasts contracted and rounded up within 5 min followed by respreading of the cells which was accomplished after 10 min already. Even though this experiment was conducted under constant shear stress conditions it still confirmed the conclusion drawn for the cell detachment assay time above. For the 9 min and 18 min assay times cells were still in the rounding up phase in the 36 min assay the cells respread already.

As a consequence of these measurements it was concluded that in order to measure the pristine adhesion strength, detachment experiments with 5 s dwell times and thus 4.5 min total assay duration suit this system best, as the effects caused by hydrodynamic pre-stress on the cells are minimized (Figure 53).

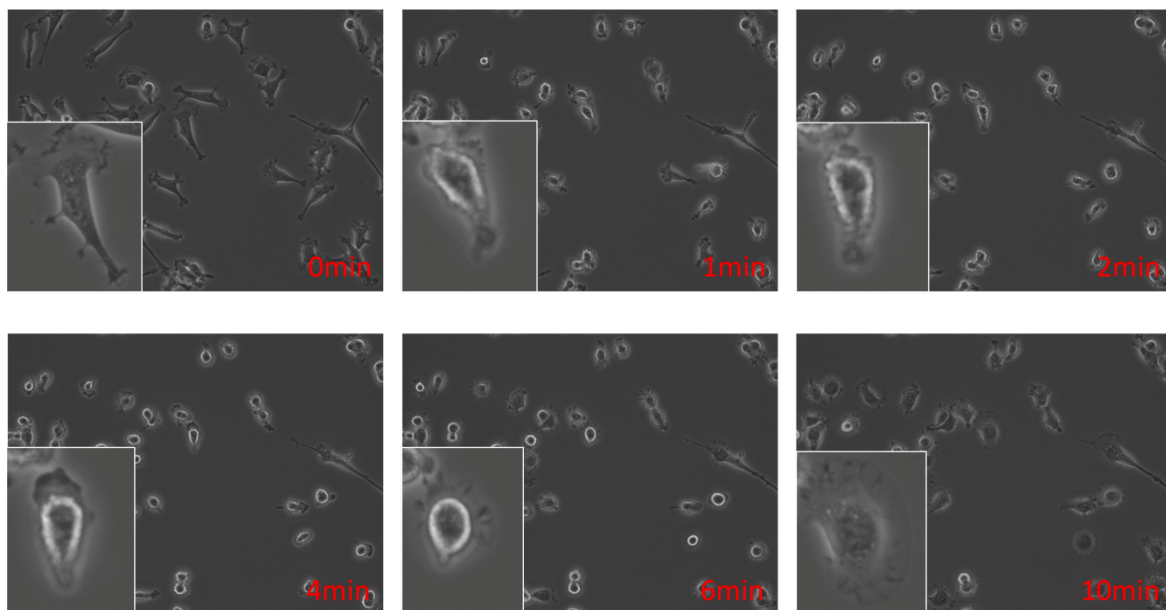


Figure 54: Cell response to shear stress of  $0.1 \text{ dyn/cm}^2$  on EG2OH SAM. Rounding up is characterized by loss of peripheral contacts, which occurred in the first 5 min. Respreading was accomplished after 10 min.

## 5 Cell adhesion strength on hydrated ethylene glycol terminated SAMs

Ethylene glycol terminated self assembled monolayers have been used to study the effect of hydration towards resistance against biological matter (see chapter 2.3.1). As has been shown for the simple adsorption of proteins [36] and the adhesion of mammalian cells [212] or living marine algae spores [37] only two repeating units of EG are sufficient to prevent adsorption of biomaterial. Still there is a lack of data to describe the impact of each additional terminal EG unit quantitatively. In order to reveal this quantitative impact of hydration towards cell adhesion the microfluidic shear force assay was utilized. Critical shear stress as a measure for cell adhesion strength was determined for REF52 fibroblasts on oligo ethylene glycol SAMs with different numbers of EG units [213], which were prepared according to chapter 3.1.1.

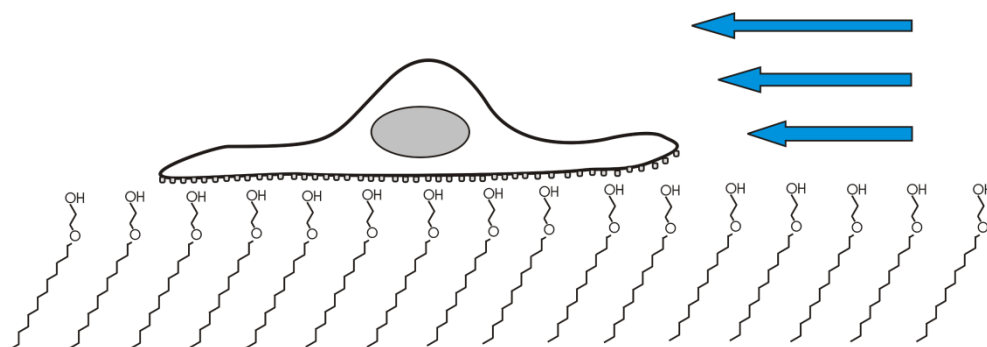


Figure 55: Scheme of an adherent fibroblast on an ethylene glycol terminated SAM.

### 5.1 Surface characterization of EG-SAMs

The films of EG-SAMs are hydrophilic with contact angles in the range of  $30^\circ$  and a thickness of  $15 \text{ \AA}$  to  $25 \text{ \AA}$  (Table 3). The SAM thickness increases with increasing number of terminal EG units in the alkanethiol. The XPS integral intensity of the Au 4f signal and ellipsometry was used to measure the SAM film thickness (Figure 56). The thickness of a fibrinogen protein layer adsorbed on the SAMs (see 3.1.2) was measured by ellipsometry. Fibrinogen thickness is much higher on EG10H ( $11 \text{ \AA}$ ) than compared to the homologues with two ( $3 \text{ \AA}$ ) and three EG units ( $1 \text{ \AA}$ ) which is in agreement with the literature [37]. This trend matches well with the observation that increasing hydration of the films leads to increasing protein resistance [42; 214].

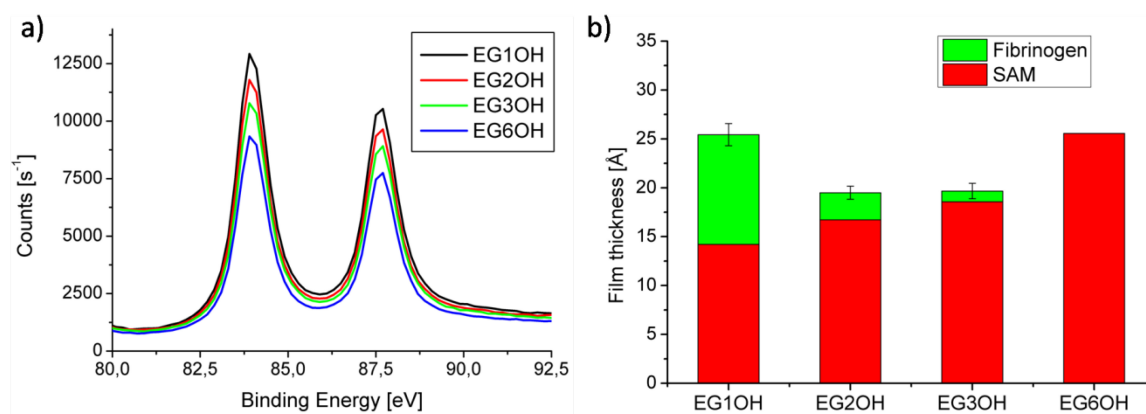


Figure 56: Characterization of the height of EG-SAMs via XPS signal intensity due to attenuation of the 4f gold signal by the SAM (a) and ellipsometry film thickness characterization including the fibrinogen adsorption experiments (b).

Table 3: Characterization results of EG SAMs on gold coated glass slides.

Name	Contact angle	Thickness		
		XPS SAM	ellipsometry SAM	ellipsometry protein layer
EG1OH	26.4±0.5°	15.0 Å ± 0.5 Å	14.2 Å ± 0.8 Å	11.2 Å ± 0.7 Å
EG2OH	30.5±0.5°	18.2 Å ± 0.5 Å	16.7 Å ± 0.8 Å	2.8 Å ± 0.4 Å
EG3OH	31.2±0.5°	20.2 Å ± 0.9 Å	18.6 Å ± 1.0 Å	1.1 Å ± 0.5 Å
EG6OH	30.1±0.5°	25.2 Å ± 1.0 Å	25.6 Å ± 1.0 Å	0.0 Å ± 0.3 Å

## 5.2 Cell adhesion strength decreases with increasing OEG chain length

The microfluidic shear force assay encountered the question how strong the hydration of the surface affects cell adhesion and if a higher hydration weakens the cell–surface interaction. The parameters determined above (chapter 4.5) for 5 h of cell incubation and 4.5 min duration of the detachment assay (5 s dwell time) were used for the assays on OEG substrates. The assay was carried out five times for each surface. Figure 57a shows the result of the assay and the corresponding microscopy pictures of the cells prior to the detachment phase of the experiment. After the first seconds flow is high enough that non-attached cells begin to move. As mentioned in chapter 4.3.3 this fraction is considered as not adhered. Sometimes (as e.g. for EG1OH) a small number of round cells can be seen in phase contrast microscopy, which are less well adhered than the main fraction. This results in a small dip preceding the main decay. The symmetric curve is representative for the distribution of adhesion strength within the population of fibroblasts present on the surface. The fraction of adhered cells decreased from 100 % on EG1OH to a value of about 80 % on EG2OH and approximately 25 % on EG3OH to less than 5 % on EG6OH. From the

detachment curves in Figure 57 the critical shear stress  $\tau_{50}$ , at which 50 % of the cell from the adhered fraction are removed, can be calculated. Cell adhesion strength drops by two orders of magnitude from about 330 dyn/cm<sup>2</sup> on EG1OH to 34.5 dyn/cm<sup>2</sup> on EG2OH and 3.0 dyn/cm<sup>2</sup> on EG3OH. On EG6OH no statistical relevant number of adherent cells was present, so the adhesion strength corresponds to 0 dyn/cm<sup>2</sup>. This result concurs with the protein resistance of these coatings [213] and also to more recent *Ulva linza* results [37]. Prime and Whitesides [213] and later Herrwerth et al. [214] identified hydration as an important design rule for protein resistant surfaces [38]. Additionally it can be derived that cell adhesion strength is reduced by the factor of ten for each additional EG unit.

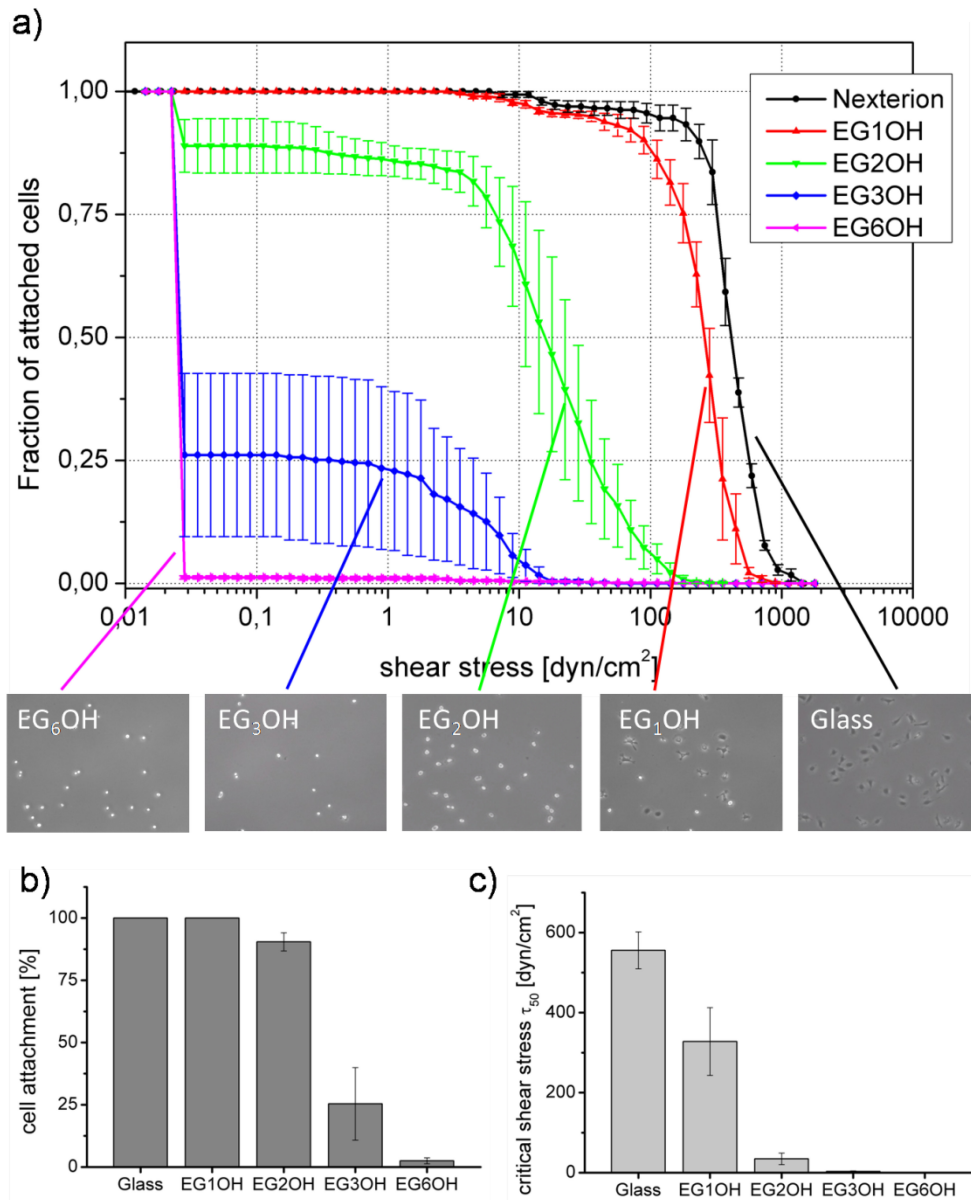


Figure 57: (a) Mean cell detachment curves for fibroblasts on different ethylene glycol SAMs. Every curve was determined from 200 to 300 cells. (b) Fraction of adherent fibroblasts on EG-SAMs and glass standard after 5 h in channel incubation, (c) adhesion strength of adherent fraction of fibroblasts on EG-SAMs and glass standard after 5 h of in channel incubation.

### 5.3 Correlation of cell morphology and adhesion strength

Visual inspection of the microscopy data revealed that the weaker adhesion is also associated with a reduced tendency of the cells to spread on the surface. Figure 58 shows a plot where the critical shear stress values  $\tau_{50}$  for cell removal on a set of EG1OH, EG2OH and EG3OH substrates are correlated with the mean spreading area on these surfaces. The mean spreading area has been calculated by measuring the area of each individual cell and then calculating the average. It becomes immediately obvious that weaker adhesion strength goes along with a smaller spreading area.

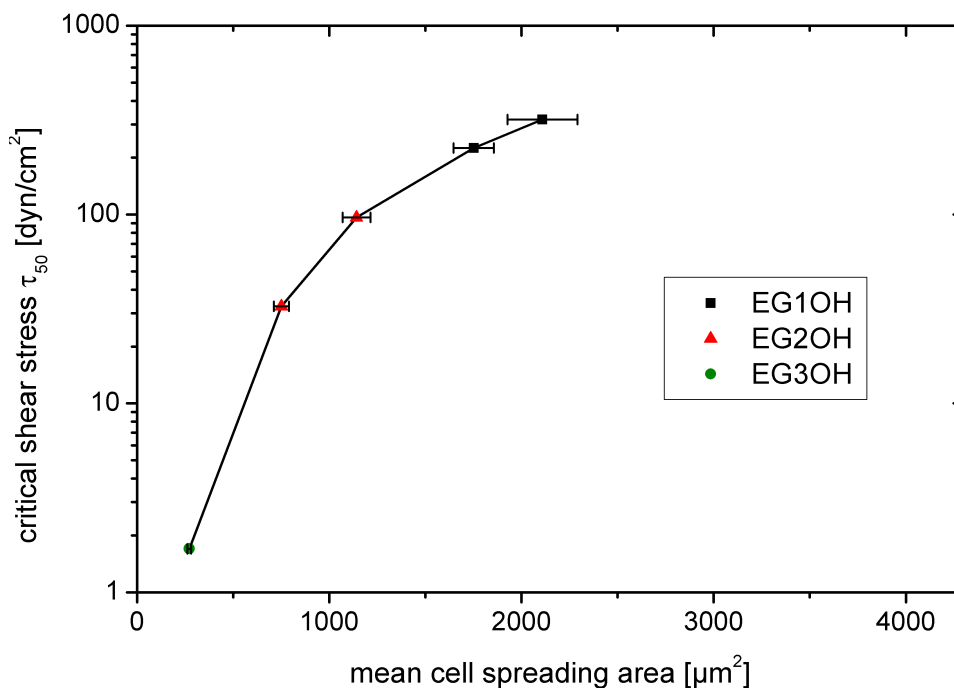


Figure 58: Fibroblast adhesion strength on EGXOH substrates dependence on the mean spreading area. Squares represent data sets from EG1OH, triangles from EG2OH and circles from EG3OH substrates. For comparison the x-axis was chosen on the same scale as Figure 59.

At this point the question arises if the observed effect of weakening of adhesion strength is solely due to the smaller attachment area of the whole cell or if it is connected to a reduced attachment strength per unit area which then would depend on the substrate. To answer the question if cell adhesion strength on EG-SAMs depends only on the spreading area or also on attachment strength per unit area, the removal experiment on EG1OH and EG2OH was revisited and the cell adhesion strength is determined for every single cell of the whole set. Then, the cells are grouped by size in bins of  $250 \text{ mm}^2$  (e.g. between  $500 \text{ mm}^2$  and  $750 \text{ mm}^2$  cell area) and the mean of the individual critical detachment shear stresses necessary for cell removal was calculated. Figure 59 shows that fibroblasts which have the same attachment area on EG1OH and EG2OH detach at higher shear rates when attached to EG1OH than to EG2OH. Interestingly between  $700 \text{ mm}^2$  and  $4000 \text{ mm}^2$  only minor

changes in the attachment strength are observed, which means that in this size range the area itself is not important any more for cell removal by a liquid flow. Probably this points towards a mechanism where the attachment strength of the cell rim facing the flow determines the critical shear stress necessary for its removal rather than the total cell area. Thus, it is clear that the attachment strength per unit area changes with the different hydration of the SAMs.

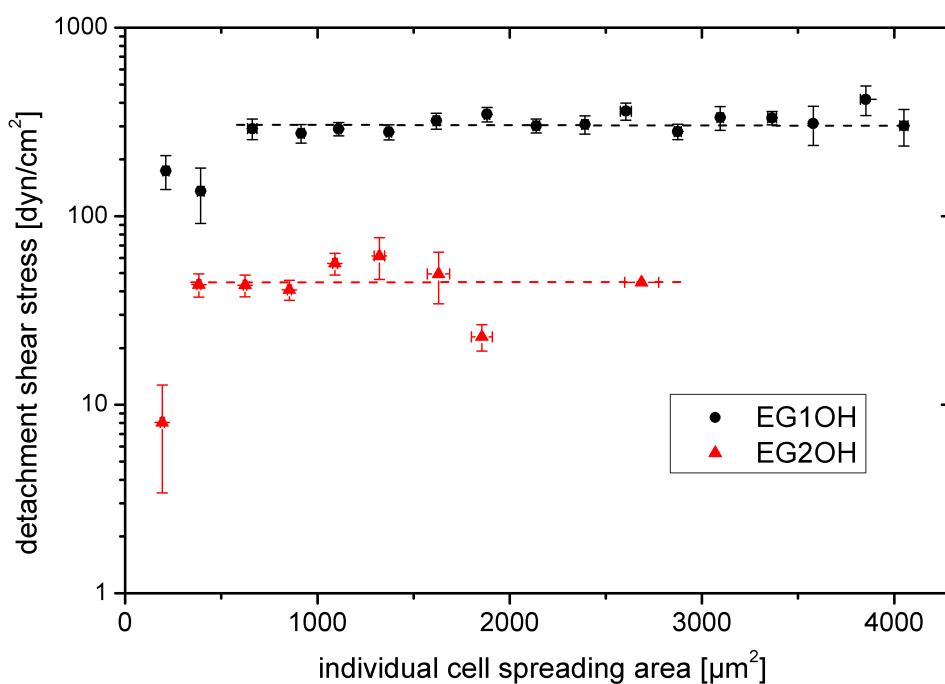


Figure 59: Fibroblast adhesion strength on EG1OH and EG2OH substrates. For every fibroblast ( $n = 690$ ) the spreading area and detachment shear stress was determined individually. The spreading areas, grouped in bins of  $250 \mu\text{m}^2$ , are displayed. Squares represent data from EG1OH, triangles from EG2OH substrates.

## 5.4 Discussion

The hydrodynamic shear force was applied to measure adhesion strength of around 300 cells at once on ethylene glycol terminated SAMs. Mammalian fibroblast cells were cultured inside a microfluidic channel and detached by hydrodynamic shear force. Parallelization of the process gave us the possibility to rule out the effects of biological variability. Cell adhesion strength for mammalian fibroblasts decreases with increasing EG-chain length and therefore with increasing water binding energy. These results are in line with previous findings on the adhesion of mammalian cells [212] and studies in the field of biofouling research where two repeating EG units were sufficient to prevent adhesion of marine algae spores [37]. In this study even three repeating units of EG are necessary to prevent major adhesion of the strongly adherent fibroblast cells. Additionally, the quantitative impact of EG chain length at the solid/water interface was revealed. The cell adhesion strength decreases with each additional EG unit by the factor of ten, resulting

in a nearly fully fibroblast adhesion resistant surface with at least three EG units. Secondly, the effects of cell spreading and surface properties towards cell adhesion could be separated. It was shown that on OEG substrates the cell adhesion strength does not only scale with cell adhesion area, but also depends on the substrate type at the same cell spreading area. This indicates that cell adhesion strength cannot be estimated accurately by simply determining cell spreading and shape. This would strengthen the assumption of a zipper mechanism for cell detachment. After rupture of distinct bonds at the leading edge of the cell, the applied force is then distributed to the remaining bonds. In the case of equal bonds, all other bonds will be overloaded and break. If the bond strength is not equally distributed, some of the weaker bonds may not withstand the extra load and break, which causes additional load on the remaining bonds and so forth. That way the cell adhesion strength is only dependent on the strongest bond strength and not the collective of cell adhesion bonds.

The developed microfluidic shear force assay was applied recently towards the adhesion strength measurement of marine bacteria *Cobetia marina* [215]. It was shown that the bacteria adhesion strength also decreases with increasing surface hydration (Figure 60). In contrast to fibroblasts the bacteria adhered much stronger and also EG chain lengths greater than three units were not sufficient to prevent cell adhesion. The study showed that the developed microfluidic shear force assay can also be applied to investigations dealing with biofouling issues.

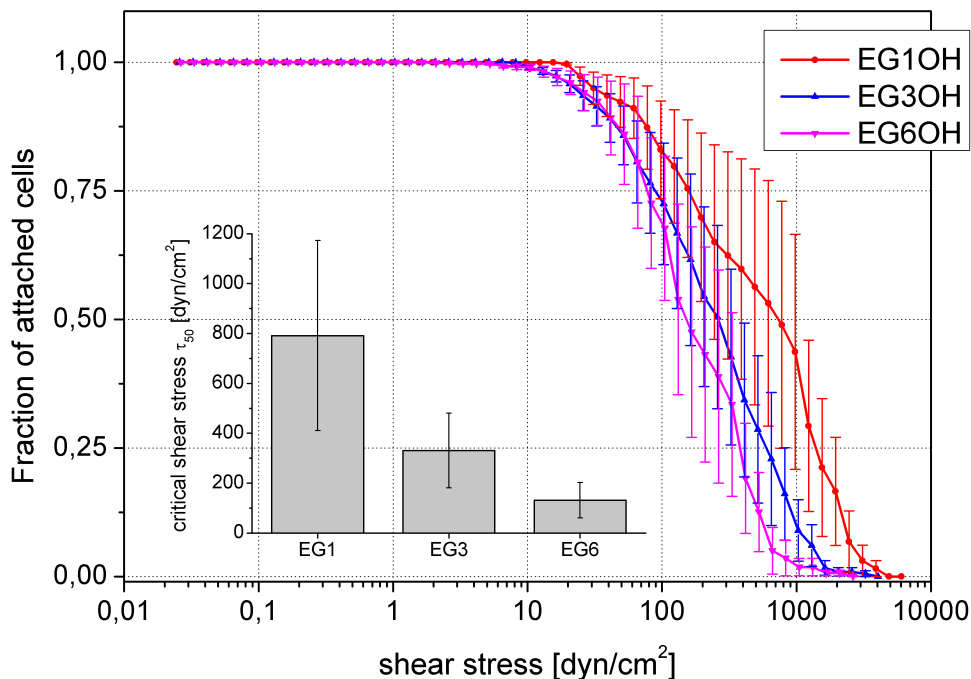


Figure 60: Mean bacteria detachment curves for adherent *Cobetia marina* on different ethylene glycol SAMs. Every curve was determined from 200 to 300 bacteria. Inset: bar graph of the mean critical shear stress. Data were taken from [215].

## 6 Cell adhesion strength on Polysaccharide Coatings

Polysaccharide coatings are considered as hydrogels which are known to show high repellence towards biomaterial (see chapter 2.3.1). On the other hand HA was found to be essentially involved in diverse processes taking place in the body (see chapter 2.3.2). Former studies point out that the specific binding of CD44 to HA has a high relevance for stem cell homing process [78; 79]. A prerequisite for the homing process is the initial escape of the cell from the blood stream by attachment via rolling followed by adhesion on the blood vessel and engraftment (see chapter 2.2). The mechanism of CD44 mediated rolling on HA seems to be complementary to the well known function of integrins and selectins in lymphocyte homing [27; 74 - 77]. Still, shear stress dependent attachment and detachment as found for selectins in leukocyte adhesion and rolling [20; 21] has not yet been reported for CD44/HA interaction. Also there is a lack of quantitative data to describe the interaction of CD44 positive blood related cells with HA under flow. In this chapter the question of how strong CD44 expressing leukemic cell lines and HPC interact with artificial immobilized HA under flow at different shear stresses is faced (Figure 61). In particular the absolute binding strength of the cells, the cell rolling speed and the question of flow stimulated cell binding to HA is addressed.

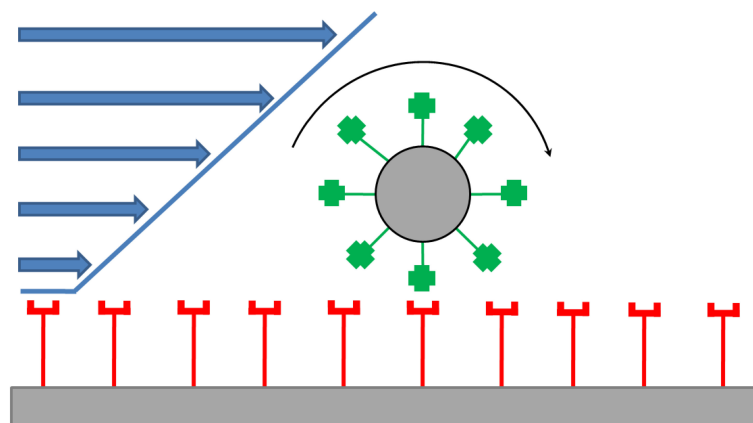


Figure 61: Scheme of CD44 expressing blood related cell rolling on HA under shear stress generated by liquid flow.

### 6.1 Characterization of hyaluronan and alginate thin films

Polysaccharide thin films have been prepared according to the protocol in section 3.1.4. Surface preparation and characterization has been performed by Georg Meseck and the results are displayed in Table 4. For a detailed description see Diploma Thesis of Georg Meseck [159]. Activation of the glass supports was achieved by plasma treatment which rendered the surfaces hydrophilic ( $\theta < 10^\circ$ ) [163]. Chemical vapor deposition of APTES on the substrates led to an increase in the contact angle ( $\theta = 33^\circ$  to  $42^\circ$ ) due to the short

amino-terminated alkylic chains. Subsequent grafting of the polysaccharides was achieved by EDC/NHS coupling and resulted again in hydrophilic surfaces (AA:  $\theta < 10^\circ$  to  $25^\circ$ , HA:  $\theta < 10^\circ$ ), in agreement with literature values [49; 163]. Spectral ellipsometry gave a thickness of 78.6 Å (SD. 23.6 Å) for HA and 21.7 Å (SD 3.9 Å) for AA. Considering the high average molecular weight of the HA used ( $M_r = 1.6 \times 10^6$  Da), the polymer is likely to establish multiple connection points, resulting in a rather loose mesh. XPS analysis confirmed the successful coupling in accordance with the comprehensive studies [49; 163].

Table 4: Thickness and contact angle of HA and AA coatings [159].

Sample	Thickness <sup>a</sup>	Contact angle <sup>b</sup>
O <sub>2</sub> plasma	n. a.	$< 10^\circ$
APTES	35.2 Å – 63.4 Å	$33^\circ - 42^\circ$
Alginate (AA)	17.7 Å – 25.6 Å	$< 10^\circ - 25^\circ$
Hyaluronan (HA)	55.0 Å – 102.2 Å	$< 10^\circ$

a) From spectral ellipsometry on silicon wafers; b) sessile contact angle on glass substrates.

## 6.2 Adhesion of fibroblasts on polysaccharides HA and AA

The capability of HA and AA to withstand the adhesion of fibroblasts are well described in the literature [46]. Still, the degree of interaction has not been quantified which is extremely useful with regard to compare the polysaccharides with other surfaces which are capable to withstand cell adhesion. Especially the EG-SAMs, which were described in chapter 5, might be put into this context for a direct comparison.

Fibroblasts were harvested according to the protocol (see chapter 3.1.6) and injected into the channel system of the microfluidic shear force assay which contained the surfaces HA and AA each in one channel and two glass surfaces for control only. The shear force experiment was conducted four times along the optimized parameters (chapter 4.5). After 5h of incubation the cells were mainly round and the adherent cell fraction was 9 % on HA and 20 % on AA (Figure 62). The critical shear stress for the adherent fraction was 5.1 dyn/cm<sup>2</sup> on HA and 7.5 dyn/cm<sup>2</sup> on AA. These values were in the size of the critical shear stress found on EG3OH-SAMs in chapter 5.2 (3.0 dyn/cm<sup>2</sup>), which are considered resistant to the adhesion of cells as described.

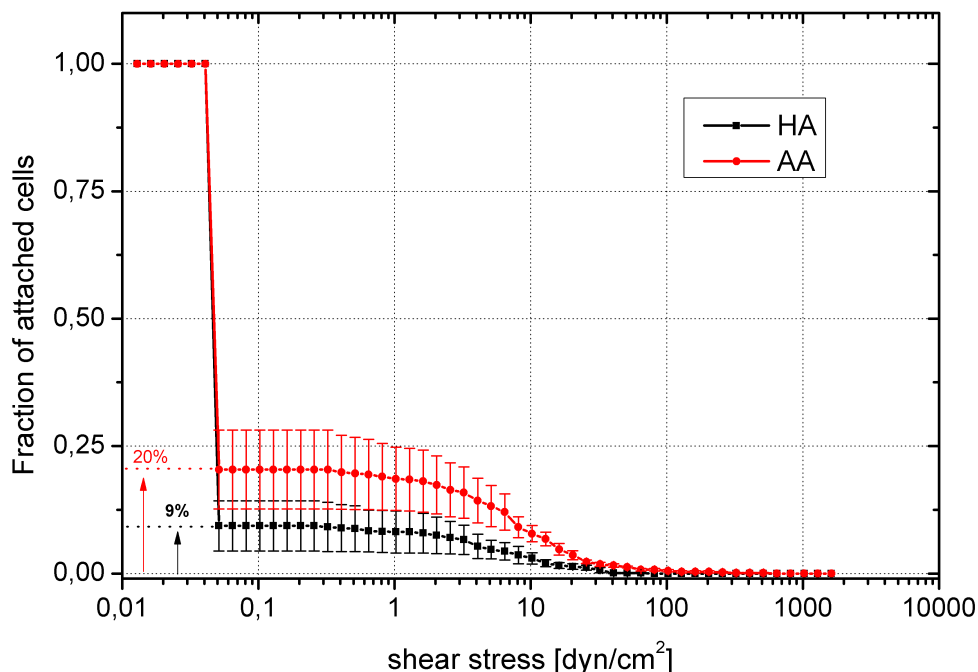


Figure 62: Adhesion of REF52 fibroblast cells on AA and HA. Detachment curves are normalized to initial cell number in the field of view ( $\sim 200$ ). Only 9 % of the cells adhere on HA (black squares) and 20 % on AA (red circles). Error bars indicate the standard error of four experiments.

### 6.3 Adhesion of leukemia cells to polysaccharides HA and AA

The interaction of two leukemic cell lines (CD44+ and CD44-) with covalently coupled thin films of AA and HA was investigated. The cell lines of choice were KG-1a cells, which have a high CD44 expression and Jurkat cells, which do not express CD44 [216217]. Parallel experiments on pristine glass were performed to control the viability of the cells and to serve as laboratory standard for comparison.

In the static adhesion assay, based on gravitational force upon inversion [178], generally a low adhesion of the leukemic cells to HA was observed. 13 % of the CD44+ KG-1a cells adhered to HA in comparison to almost no CD44- Jurkat cells (1,6 %) was found.

To determine the influence of HA towards cell adhesion quantitatively the adhesion strength with the microfluidic cell detachment assay was measured. KG-1a and Jurkat cells were incubated with supplemented RPMI-1640 medium at 37 °C and 5 % CO<sub>2</sub> on HA, AA and pristine glass inside the channels for 3 h. Afterwards, performing the cell detachment assay, an exponentially increasing flow was applied and the adherent cells were manually counted by analyzing the time lapse microscopy videos. Statically attached cells and cells which were slowly rolling on the substrate were assigned as adherent ones. Cells which were floating with the liquid flow (speed of  $\sim 25 \mu\text{m/s}$  per  $0.1 \text{ dyn/cm}^2$  shear stress) could easily be distinguished from rolling cells and were considered non adherent. Figure 63 shows the detachment curves for Jurkat and KG-1a on the three substrates. The standard error was calculated from up to six repeats of the experiment. As it can be seen for both

cell types, the discrimination of non-adherent from adherent cells appears clearly at a very small shear stress of  $\sim 0.05$  dyn/cm<sup>2</sup> and results in an initial drop of the cell number. The remaining (adherent) cells require a much higher flow to be removed. Thus, the fraction of initially adherent cells can be calculated as measure of how readily cells adhere to the surface.

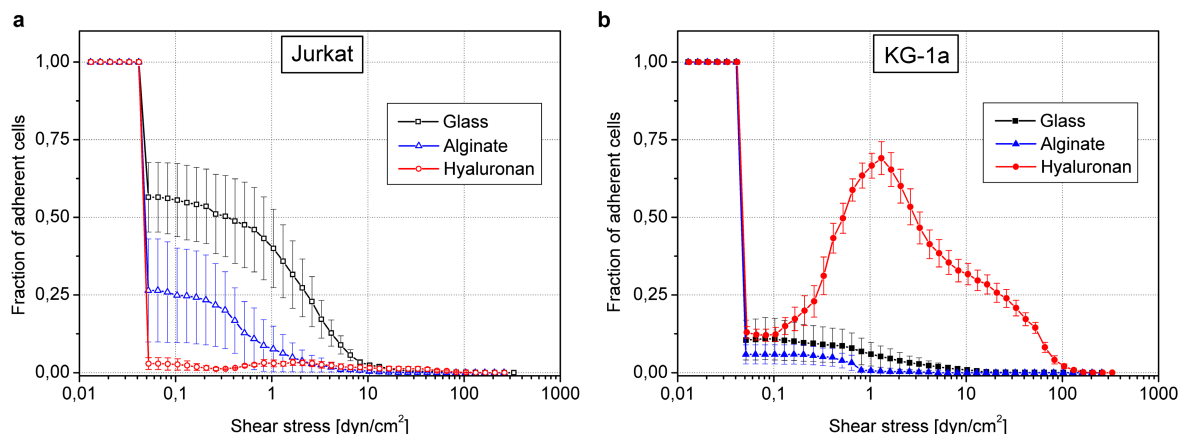


Figure 63: Adhesion of leukemic cells on AA and HA. Detachment curves are normalized to initial cell number in the field of view ( $\sim 600$ ). (a) Detachment curves of Jurkat cells on glass (open black squares), AA (open blue triangle) and HA (open red circles). (b) Detachment curves of KG-1a cells on glass (black squares), AA (blue triangle) and HA (red circles). Error bars indicate the standard error. Note, that the increase in fraction of adherent cells in (b) is due to shear stress induced readsorption as discussed in the text.

The experiment involving Jurkat cells (Figure 63a) shows that 56 % of the seeded cells adhere to glass while this fraction significantly decreases to 26 % on AA and 3 % on HA. To quantify the adhesion strength the critical shear stress ( $\tau_{50}$ ) was determined which is needed to remove 50 % of the adherent cells. The values obtained follow the above determined fraction of adherent cells with the strongest adhesion of 1.48 dyn/cm<sup>2</sup> on glass decreasing to 0.49 dyn/cm<sup>2</sup> on AA and less than 0.06 dyn/cm<sup>2</sup> on HA (Figure 64). Thus, the presence of covalently coupled HA or AA on glass did not only render the surfaces less attractive for adhesion but also weakens the adhesion strength of Jurkat cells. These results are in line with the fibroblast studies by Morra and emphasize that polysaccharide coatings are rather inert to cell adhesion if no specific interaction is possible [47].

The results for the CD44 expressing KG-1a cells are more complicated (Figure 63b). First of all, KG-1a cells showed a generally reduced tendency to adhere to glass compared to Jurkat as only 10 % of the seeded cells adhere. On AA substrate the adhesion is further reduced to a fraction of only 6 %. In contrast to that the HA substrate showed with 13 % adherent fraction of KG-1a cells an increase - even with respect to glass. A puzzling result which was not observed before in the microfluidic experiments (e.g. for Jurkat) is the increase in number of cells on the surface with increasing shear stress  $> 0.2$  dyn/cm<sup>2</sup>. At this point important experimental detail have to be pointed out: Though pure medium was used during the detachment assay to flush the channel, especially in the beginning there

were residual cells located in the tubing and the part of the channel upstream from the observed field of view. These cells were flushed into the field of view and seem to attach more readily than during three hours of static incubation. Thus, the flow seems to stimulate KG-1a cells to bind to HA leading to a temporary increase of the cell number during the experiment. At higher shear stress cells were removed and the  $\tau_{50}$  diminishes from 1.40 dyn/cm<sup>2</sup> on glass to 0.56 dyn/cm<sup>2</sup> on AA and reaches a maximum of 5.17 dyn/cm<sup>2</sup> on HA (Figure 64). Both, the adhesion strength and the fraction of adherent KG-1a cells are enhanced with HA present on the surface.

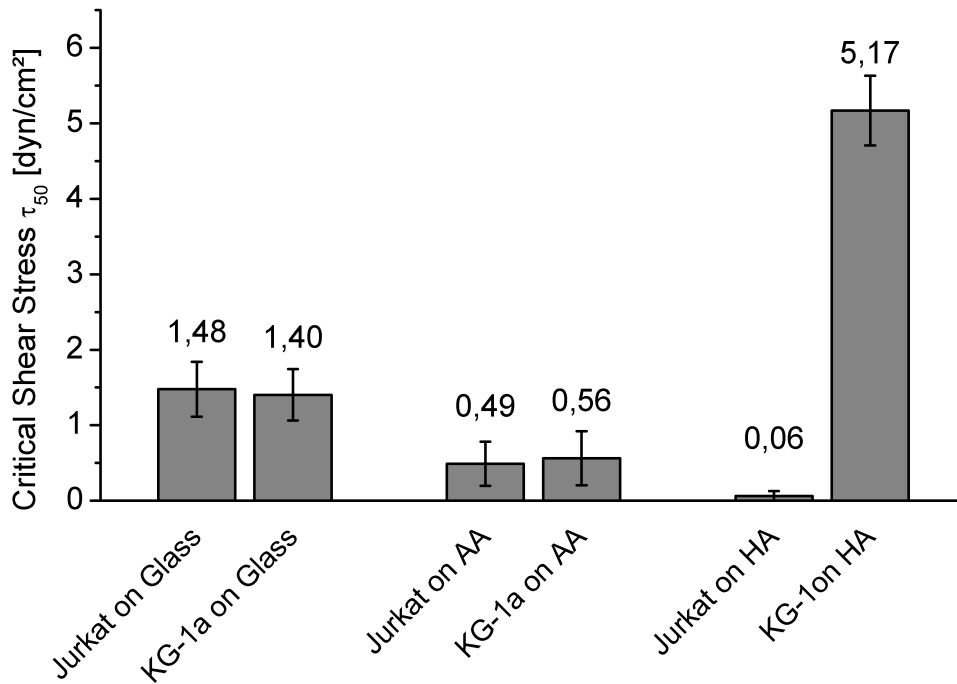


Figure 64: Critical shear stress as a measure of cell adhesion strength of Jurkat and KG-1a cell lines on glass, AA and HA. Cell adhesion strength is about the same for both cell lines on glass and AA but not on HA. Error bars represent standard error.

## 6.4 Flow mediated binding of KG-1a cells to hyaluronan

The above observation of flow induced adhesion was possible because cells still present in the tubing upstream of the observation area were rinsed into the channel. However, supply of cells in this experiment was not controlled and more systematic experiment was designed. KG-1a cells (~ 600) were seeded inside the microfluidic channel for 5 min to allow sinking down to the surface by gravity and to establish a physical contact to the surface. Subsequently, a constant flow was applied to stimulate adhesion of the resting cells. The experiment was conducted for each shear stress three times. After 10 s of shear stress the fraction of adherent, i.e. the fraction of non floating cells, was determined for a series of different shear stresses (Figure 65). The maximum number of adherent cells was

found at a shear stress of 1.0 dyn/cm<sup>2</sup>. This value is only slightly below the 1.3 dyn/cm<sup>2</sup> derived from the dynamic cell detachment experiment of described above (dotted curve reproduced from Figure 63b).

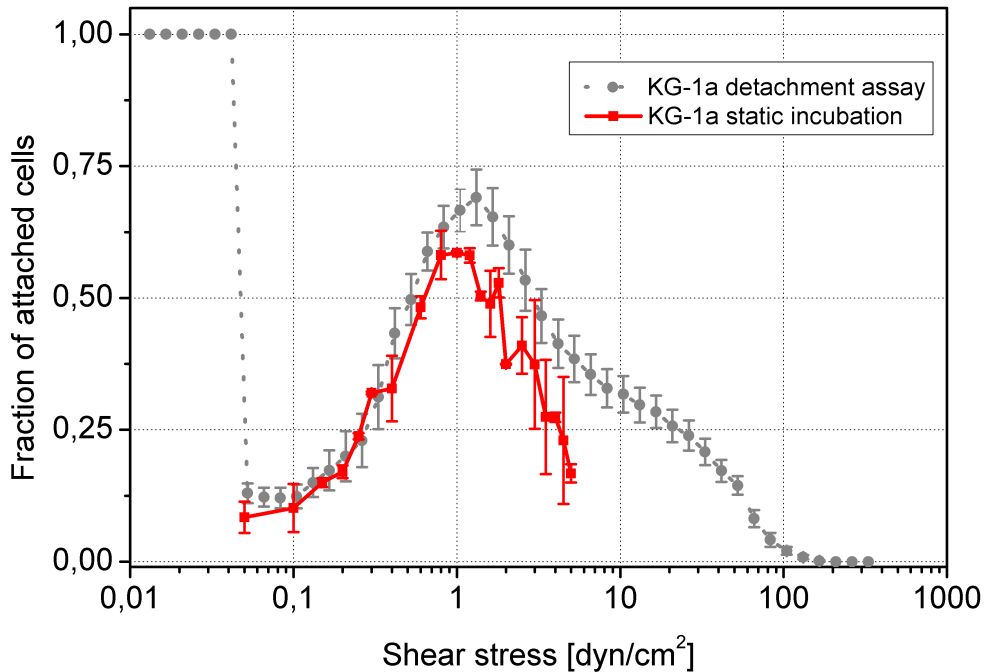


Figure 65: Comparison of KG-1a on HA flow activation measured by two different assays. Curves as determined by the cell detachment assay (gray cycles) and the constant flow assay (red squares). The maximum for both experiments is around 1 dyn/cm<sup>2</sup>. Error bars represent standard error.

Additionally to the number of adherent cells, their rolling speed in dependence of applied shear stress was analyzed. As pointed out above rolling cells can easily be distinguished from cells passively driven by the liquid flow due to their strongly decreased velocity (2 μm/s versus 25 μm/s at 0.1 dyn/cm<sup>2</sup>). Microscopy movies of rolling cells were recorded and cells (n > 30) were tracked during 60s of constant flow to calculate their rolling speed (Figure 66). Rolling velocity increased linearly from ~ 2.0 μm/s to ~ 11.5 μm/s when the shear stress was increased from 0.1 dyn/cm<sup>2</sup> to 0.6 dyn/cm<sup>2</sup>. At higher shear stress, the cells reach a maximum rolling speed of ~ 15 μm/s which remained constant, even at further increasing flow rates. The transition between the linear increase and the fixed rolling speed occurred around 1 dyn/cm<sup>2</sup>. This supports the findings of the adhesion experiments which showed an enhanced interaction of KG-1a cells and the HA coated surface for shear flows of about 1 dyn/cm<sup>2</sup>.

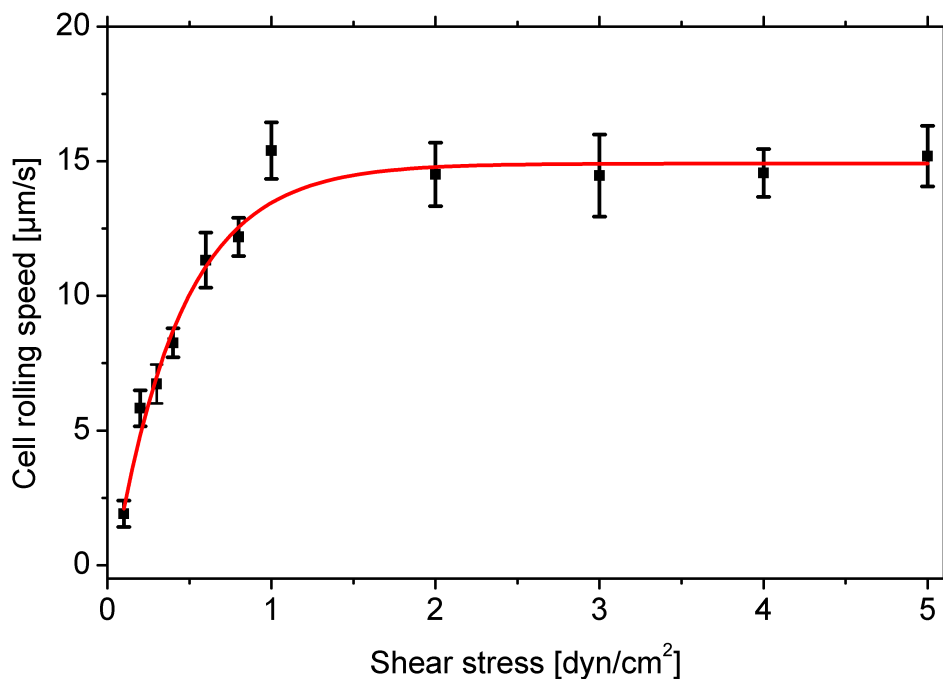


Figure 66: Cell rolling speed in dependence of applied shear stress. Rolling speed increases linearly up to 0.6 dyn/cm<sup>2</sup>. Maximum cell rolling speed is reached at around 1 dyn/cm<sup>2</sup>. Black filled squares indicated the measured data, red curve is the result of fitting an exponential saturation function. Error bars show standard error.

## 6.5 CD44 dependent binding of leukemic cells to hyaluronan

Further the concept of flow induced binding towards five leukemic cell lines with different CD44 expression on HA was tested. CD44 expression and distribution on the surface was determined by flow cytometry and immunofluorescence microscopy (Figure 67). Jurkat and Kasumi-1 cells showed no CD44 expression. K-562 cells showed a very heterogeneous expression. Cells with a high and a medium expression, but also cells without any CD44 expression were detected. KG-1a and HL-60 cells had a very high CD44 expression.

To compare the flow activation of the different cells to HA coated surfaces a constant flow assay was applied and the flow induced accumulation of cells analyzed. As evident from the flow cytometry measurements, some of the cells had only low CD44-expression. Thus, a comparably low shear stress of 0.2 dyn/cm<sup>2</sup> was chosen in order to just stimulate flow activated adhesion but not to remove weakly adherent cells. The constant flow assay was performed nine times. All three CD44 expressing cell lines attached from flow on HA while none of the two CD44 negative cell lines attach (Figure 68). Cell attachment for HL-60 was highest after 4 min (~ 810 cells, ~100 % CD44) followed by KG-1a (~ 340 cells, ~ 100 % CD44) and K-562 (~ 190 cells, ~ 92 % CD44). While the relative trend that CD44 expression enhances the sticking ability on HA is obvious, it was not possible to find a linear correlation between CD44 expression and attachment rate, as e.g. HL-60 and KG-1a

show similar expression but different attachment probabilities. One reason could be the cell size as larger cells rolling on the surface are exposed to a higher shear stress as they physically extend further into the parabolic flow profile. This could lead to an enhanced flow activation of HL-60 (14.86  $\mu\text{m}$ , SD 2.51  $\mu\text{m}$ ) compared to KG-1a (12.97  $\mu\text{m}$ , SD 1.63  $\mu\text{m}$ ) and therefore a higher attachment rate. Also, cell line specific regulation and expression of further receptors (e.g. VLA-4) are involved in the adhesion process to HA [72].

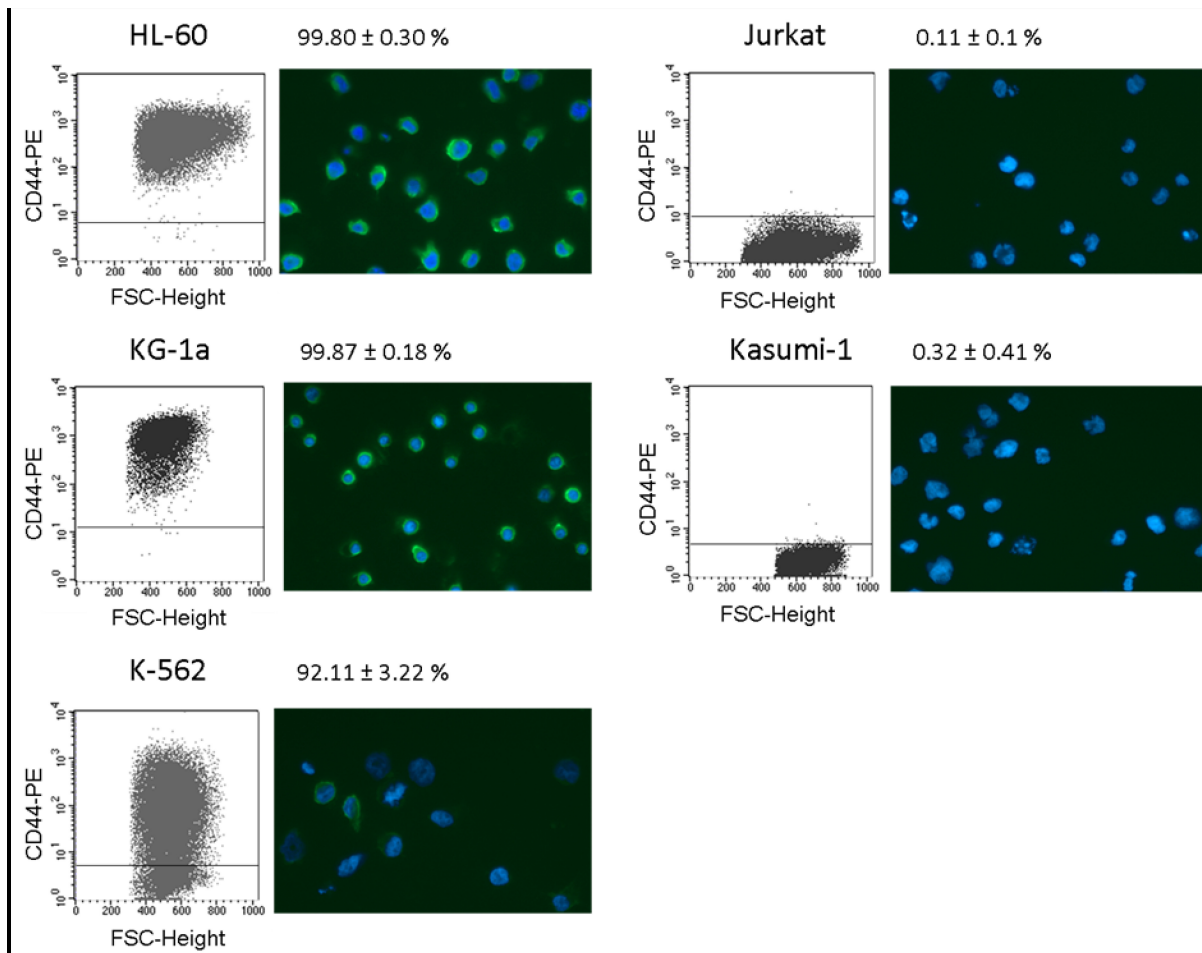


Figure 67: Flow cytometry and immunofluorescence microscopy images of CD44 on the five leukemic cell lines used in the microfluidic flow incubation assay. For flow cytometry anti-CD44- PE (clone G44-26) was used. Percentages for the mean and standard deviation of CD44-positive cells of at least 3 experiments are shown. For immunofluorescence microscopy DNA was stained with Hoechst 23342 (blue) and CD44 with the clone A3D8 and Alexa Fluor 488 (green).

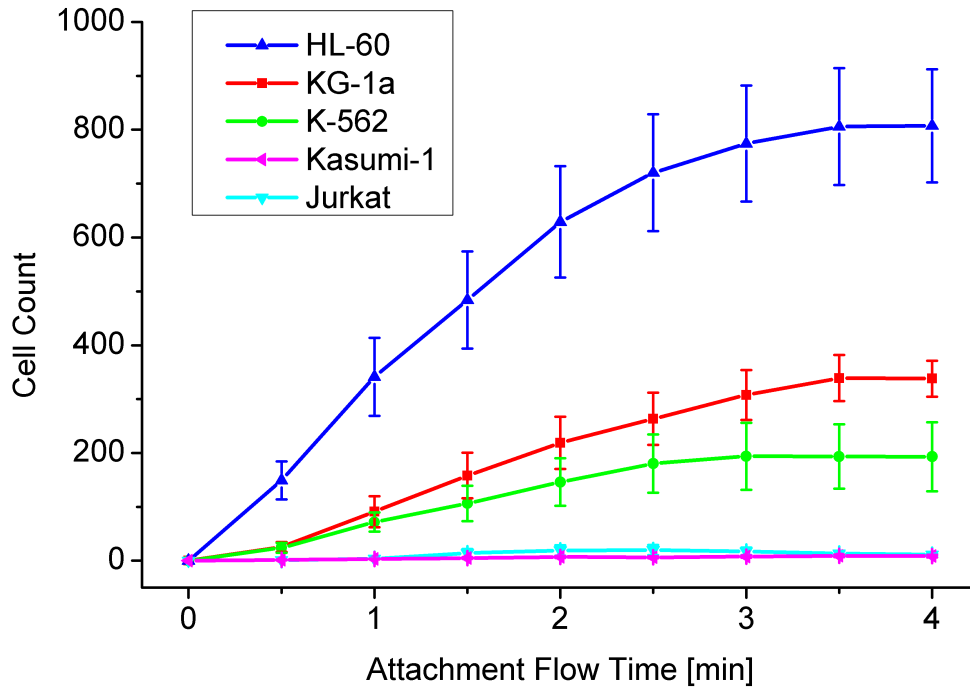


Figure 68: Constant flow assay for leukemic cell lines expressing different amounts of CD44. The applied shear stress during incubation was  $\sim 0.2 \text{ dyn/cm}^2$ . Cell attachment occurs only for CD44+ cell lines. Error bars represent the standard error.

## 6.6 Binding of hematopoietic progenitor cells to hyaluronan

To show that the findings above on leukemic cell lines have relevance for isolated human primary material, the impact of HA interactions towards clinical relevant hematopoietic stem cells was clarified. Therefore, HPCs, enriched from umbilical cord blood, were incubated on HA and AA substrates inside the channel system as described in the section before. HPCs have a high CD44-expression (Mean 98.78 %, SD 0.81 %). Unfortunately access to this isolated human material is limited and it was impossible to repeat the full experimental series conducted for the leukemic cell lines. Thus, experiments were restricted to single cell analysis in the microfluidic channel and a phenomenological description of the observations when a shear flow is applied. Conducting the cell detachment assay two times revealed that HPCs do not adhere on AA (0 %) and only few on HA (6 %). Still, at raising shear stress more HPCs adhere and roll in dependence of the shear stress (velocity of  $\sim 14 \mu\text{m/s}$  at  $0.5 \text{ dyn/cm}^2$  and  $\sim 18 \mu\text{m/s}$  at  $1.0 \text{ dyn/cm}^2$ ) on HA and detach at relatively high shear stress of  $2.17 \text{ dyn/cm}^2$  similar to KG-1a cells. However, the limited number of cells in this experiment ( $\sim 100$ ) did not allow any more elaborate analysis but this observation was supported by a descriptive experiment: When keeping the shear stress constant at  $2 \text{ dyn/cm}^2$  and switching the liquid flow direction the HPCs follow the flow direction instantly at constant rolling speed of  $17.8 \mu\text{m/s}$  (Figure 69). Whenever the flow was switched off, first HPCs arrested at  $0.3 \text{ dyn/cm}^2$  on HA then retracted the

filopodia contacts at around  $0.2 \text{ dyn/cm}^2$  and detached from the surface (Figure 70). The fact that the surface contact is lifted becomes visible in the velocity which is much higher than for the rolling cells at higher flow velocities. Thus, also HPCs have a strong interaction with HA as visible in adhesion strength and the tendency to roll at the surface. Also the shear force induction was visible as cells which are not exposed to the shear force for a certain while lift their surface contact and go with the flow. Thus the descriptive observations on HPCs isolated from human cord blood showed that the concept of flow activated adhesion also occurs in medically relevant material.

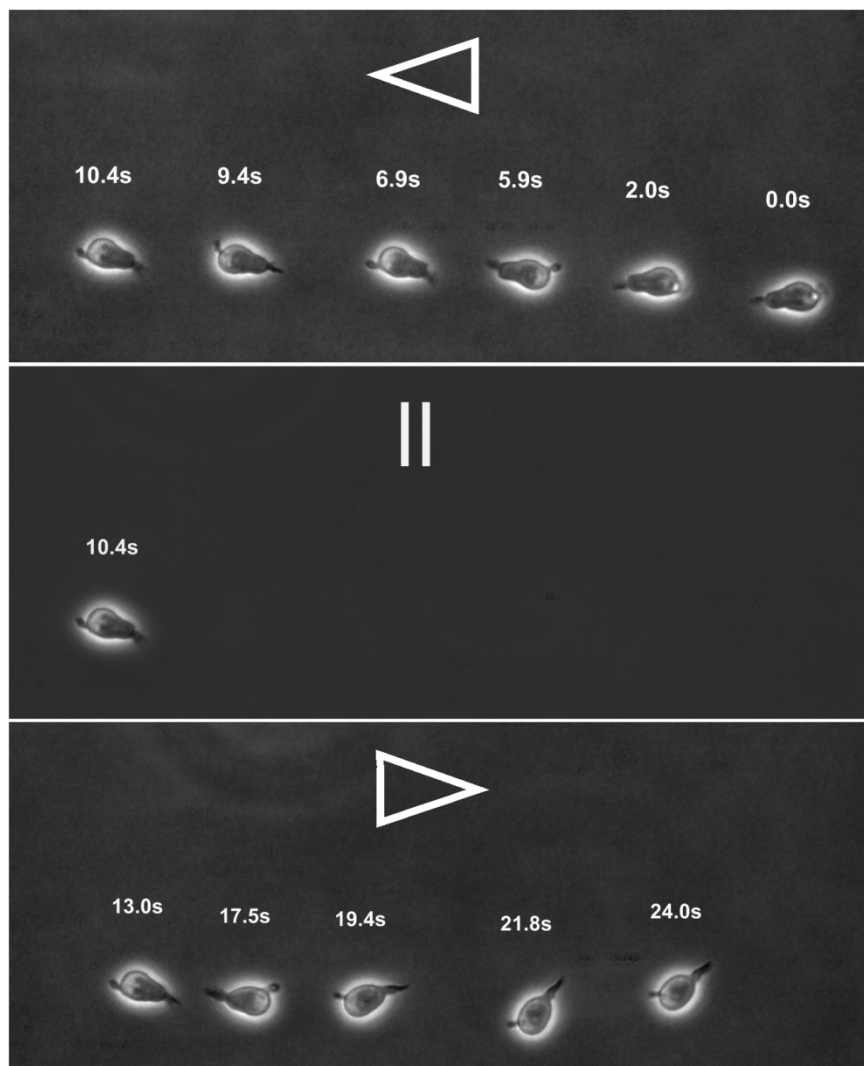


Figure 69: Image sequence of a rolling HPC cell on HA inside a microfluidic channel. Arrows show the flow direction. The rolling speed is in the mean  $17.8 \mu\text{m/s}$  at a liquid flow corresponding to a shear stress of  $2 \text{ dyn/cm}^2$  in the same direction (a, c). The cell rolling direction changes instantly when the flow direction is switched (b).

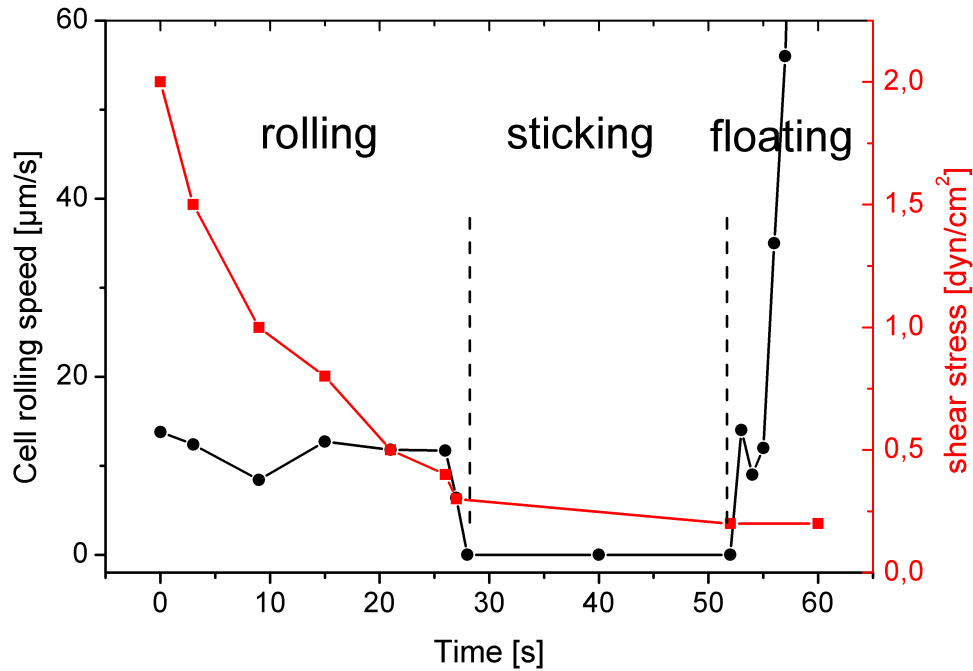


Figure 70: Cell rolling speed of a single HPC in dependence of applied shear stress. At shear stress below  $0.3 \text{ dyn/cm}^2$  (red curve) the HPC is in the arrest state (black curve). HPC retracts filopodia and detaches from the surface when shear stress decreases to  $0.2 \text{ dyn/cm}^2$ .

## 6.7 Discussion

In this chapter the adhesion strength of fibroblasts and the specific interaction between hyaluronan and leukemic cell lines and umbilical cord blood hematopoietic progenitor cells (HPCs) was investigated. Studies by Morra et al. [47] previously showed the general inertness of hydrogel like polysaccharide coatings which is most likely due to their strong hydration. The latter might present an important prerequisite to prevent adhesion [28]. The study confirms the inertness of such coatings as fibroblasts adhere about as weak as on EG3OH-SAMs, which were discussed in chapter 5. Also a low adhesion strength is observed for Jurkat on AA ( $\tau_{50} = 0.49 \text{ dyn/cm}^2$ ), on HA ( $\tau_{50} = 0.06 \text{ dyn/cm}^2$ ) and for KG-1a on AA ( $\tau_{50} = 0.56 \text{ dyn/cm}^2$ ). For CD44+ KG-1a on HA a stronger adhesion is observed ( $\tau_{50} = 5.17 \text{ dyn/cm}^2$ ). The accumulation of KG-1a on HA during the shear force assay for shear stresses at or higher  $0.2 \text{ dyn/cm}^2$  indicates that the interaction is shear stress mediated, so cell adhesion and rolling on HA are stimulated by the presence of a shear force. Interestingly the values directly correspond to the ones found for selectin dependent leukocyte rolling [20; 21]. Experiments using constant flow conditions reveal that the fraction of adherent cells and the rolling speed of KG-1a cells on HA depend nonlinearly on the shear stress present. The maximum adhesion fraction and thus the highest cellular response was found at around  $1 \text{ dyn/cm}^2$ . In alignment with these findings, the cell rolling speed correlates linearly with shear stress at low ranges but becomes constant above

1 dyn/cm<sup>2</sup>. This observation is in line with previous findings by Finger *et al.* and others for selectin dependent leukocyte rolling [20; 218]. From these observations the following mechanism can be concluded: KG-1a cells respond to a flow and attach to the HA substrate. The cells roll on HA with a specific speed that is proportional to the applied shear stress. Beyond a certain flow, cell binding to HA is activated and the cells actively resist further acceleration by the enhanced surface interaction. At even larger shear stress, the Stokes force on the cells exceeds the binding strength to the surface and the cells are removed. The mechanism of bond strengthening remains unclear but one might speculate on capture bond theory [22] or additional other transport mechanisms [218] known from leukocyte rolling. CD44+ KG1a, HL-60 and K-562 cells show a much higher attachment compared to CD44- Jurkat and Kasumi-1 cells. The findings indicate that CD44 expression is a prerequisite for adhesion to HA and it was for the first time observed that CD44+ leukemia cells roll on pure HA surfaces, but the mechanism behind CD44 dependent binding to HA is still controversial and not yet fully understood [219]. Not all CD44 expressing blood related cells attach to HA [62; 220]. Further experiments to unravel the specific role of different adhesion receptors are anticipated for the future but exceed the scope of the presented work which is focused on the shear stress regulated adhesion. Up to now it was unknown if the interaction of leukemia cells with HA is stimulated by flow. It was shown that minimum external shear stress (0.2 dyn/cm<sup>2</sup>) strongly enhances the interaction of CD44+ cells with hyaluronan (flow induced rolling and adhesion). The clinical relevance was demonstrated by the flow induced interaction between HPCs that were isolated from cord blood, thus the observations in cell lines were unequivocally validated. This is the first time that rolling and flow induced and regulated adhesion of hematopoietic progenitor cells on hyaluronan was observed. These results indicate that flow mediated adhesion is an important concept valid beyond lymphocyte rolling on endothelial cells [69; 70]. The shear stress regulated adhesion on HA is especially interesting as the CD44/HA interaction plays an important role for homing and engraftment of HPCs into the bone marrow which has been shown in spleen of NOD/SCID mice [221]. Possibly the mechanism of HPC and leukemic cell adhesion on HA might be similar to the one discussed for selectin based leukocyte rolling in inflammatory response and thus the shear stress regulated adhesion represents a more general principle than so far anticipated.

## 7 Cell adhesion on polarized LiTaO<sub>3</sub> substrates

In previous studies algal spores showed a reduced settlement on surfaces with the same charge as the spore body (see 2.3.4). To this point the effect of charge towards cell adhesion on chemically similar surfaces has only been studied in detail for Coulomb interactions but not for polarity effects yet.

In this chapter the question is addressed if cells can respond to different electric polarization. In order to give an answer to this question periodically poled LiTaO<sub>3</sub> substrates were investigated towards cell adhesion. The unique approach of using periodically poled substrate domains allows the cell to “choose” between the preferential polarizations and field gradients without being effected by response to chemical changes

### 7.1 Characterization of poled LiTaO<sub>3</sub> substrates

The ferroelectric LiTaO<sub>3</sub> substrates (see , chapter 3.1.5) provided by our collaborator Prof. Peter Dowben (University of Nebraska-Lincoln, USA), were analyzed by the Group of Prof. Alexei Gruverman (University of Nebraska-Lincoln, USA) with a piezoresponse force microscope (see Figure 71). The values for dielectric and piezoelectric constants, displayed in Table 5, are in line with previous results [165].

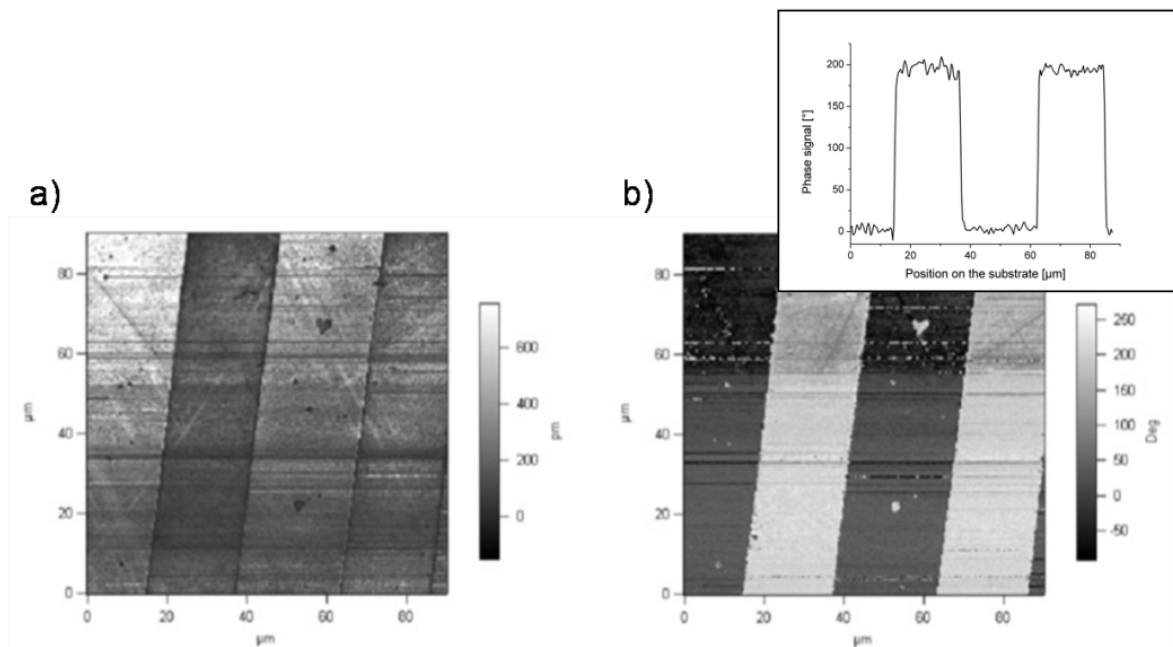


Figure 71: PFM images of periodically poled LiTaO<sub>3</sub> recorded by Prof. Alexei Gruverman Group (UNL). (a) amplitude image and (b) phase image with a linescan inset.

Table 5: Characterization results of piezoresponse force microscopy on periodically poled LiTaO<sub>3</sub>

Parameter	Value	
	constant stress	constant strain
$\epsilon_{11}$	51 $\epsilon_0$	38.3 $\epsilon_0$
$\epsilon_{33}$	45 $\epsilon_0$	46 $\epsilon_0$
Piezoelectric constant		
$d_{15}$	26 pC/N	
$d_{22}$	7 pC/N	
$d_{31}$	-2 pC/N	
$d_{33}$	8 pC/N	
Spontaneous polarization	$\sim 60 \mu\text{C}/\text{cm}^2$ [222]	
Surface dipole	$\sim 140 \text{ e}\text{\AA}/\text{K}$ ( $\frac{1}{2}\text{LiNbO}_3$ from [223])	

## 7.2 Cell adhesion on (+) and (-) and periodically poled LiTaO<sub>3</sub>

Prior to the adhesion experiments the substrates were cleaned by immersion in 3 mmol NaOH containing 10 % p.a. ethanol and ultrasonicated for 30min prior rinsing with ethanol and water. The three substrates were glued to the bottom of one petri dish. The adhesion and spreading of cells was followed by time lapse microscopy inside the custom build incubation chamber (chapter 3.2.4) at cell culture conditions (37 °C, 5 % CO<sub>2</sub>). Cell spreading of fibroblasts was followed on several positions on all three substrates by imaging with a 10x Ph1 objective and the automated microscopy stage. The time interval was 2.5 min for the first 15 min followed by a 10 min-interval afterwards. Fluorescence imaging of cell focal contacts was performed with a 20x Ph1 objective and GFP/YFP filter. Images of fibroblast cells after 1 h of adhesion on positive, negative and periodically poled LiTaO<sub>3</sub> showed advanced spreading on all substrates (Figure 72).

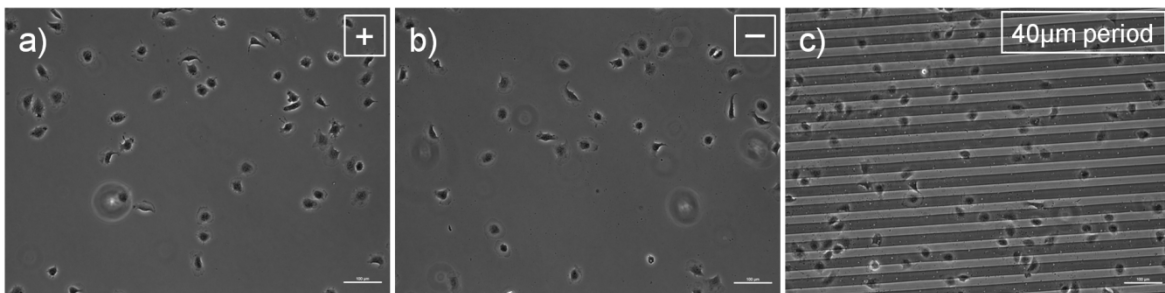


Figure 72: REF52 cell spreading after 1 h was similar on positive (a) negative (b) and periodically poled (c) LiTaO<sub>3</sub> surfaces. Cells were mostly spread of all three surfaces.

Time resolved analysis of cell spreading was performed at the border of a single poled and a periodically poled region (Figure 73) from a LiTaO<sub>3</sub> substrate. Independent on the substrate location cells started spreading after 10 min and cells were mostly spread after 1 h and have reoriented the cytoskeleton at the 18 h time point.

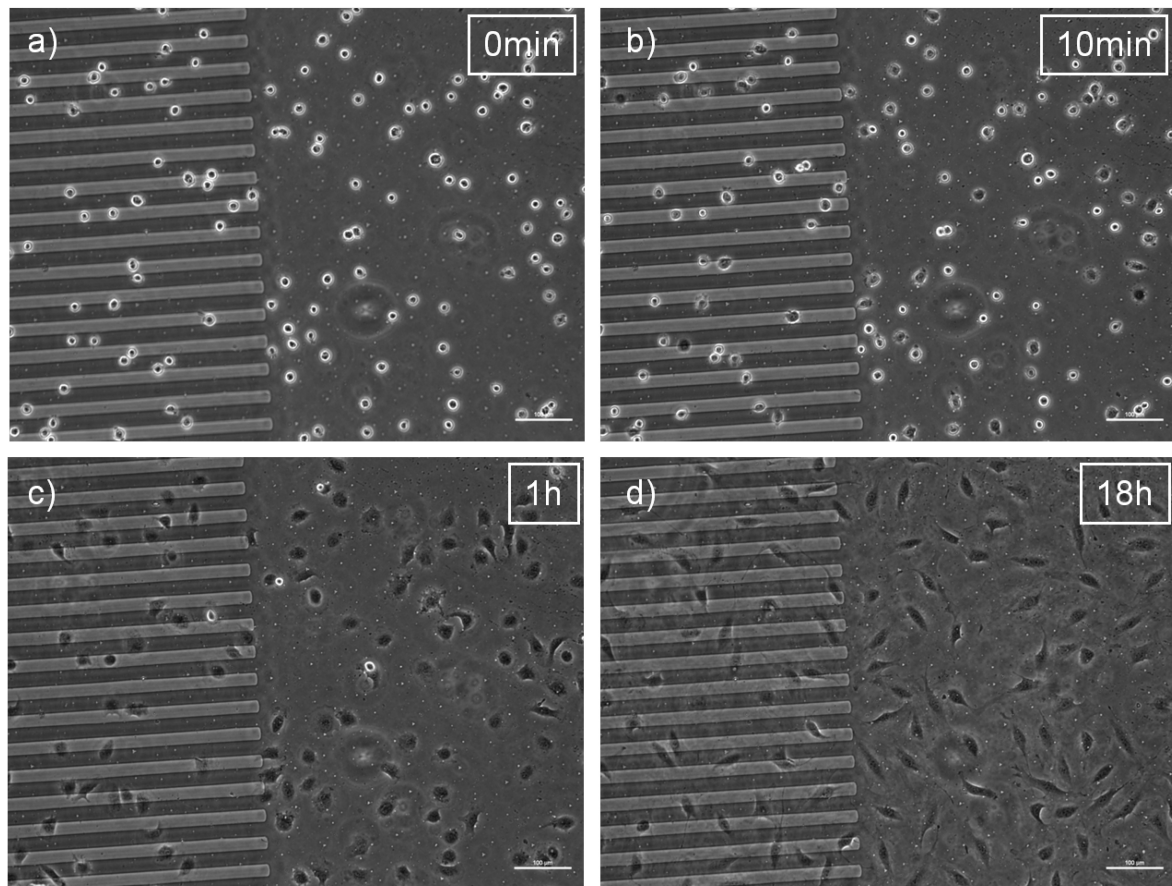


Figure 73: REF52 spreading of fibroblasts 0 min (a), 10 min (b), 1 h (c) and 18 h (d) after seeding on LiTaO<sub>3</sub>. Spreading kinetic was similar on single poled and periodically poled area.

The orientation of the cells after 18 h appears randomly and imaging of cell focal contacts by YFP-stained paxillin reveals the absence of preferential contact position and orientation in dependence of the surface polarization at that incubation time (Figure 74).

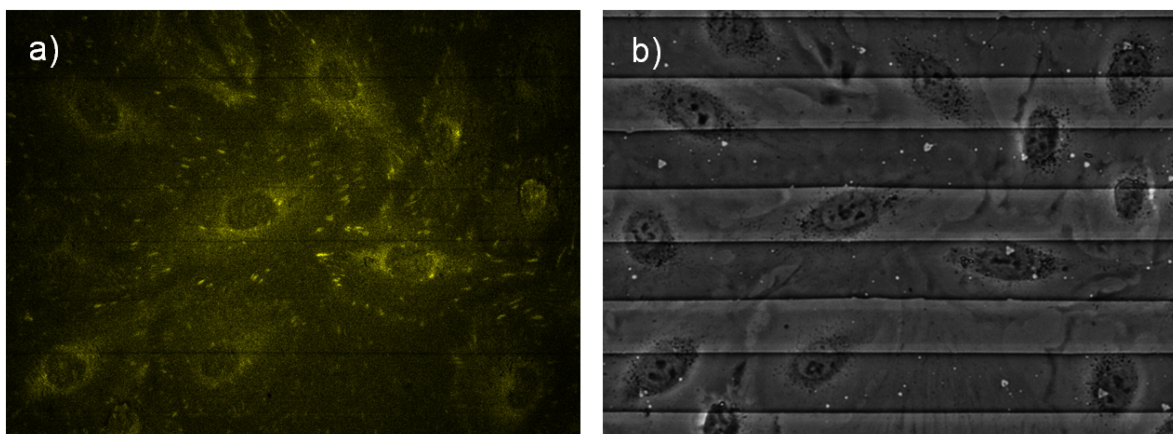


Figure 74: REF52 after 18 h of seeding on periodically poled LiTaO<sub>3</sub>. Cell focal contacts imaged by fluorescence microscopy of cells YFP stained paxillin (a) and the phase contrast image (b). The cells did not show either oriented anisotropy in shape or preferential positioning of focal contacts with respect to the surface polarization domains.

### 7.3 Cell response to polarization of periodically poled LiTaO<sub>3</sub>

As there was no evidence for polarization dependent cell adhesion kinetics, a more detailed analysis of the settlement site towards polarization was conducted. The time lapse microscopy images of both fibroblasts and leukemic cells were investigated towards a preferential settlement site on periodically poled LiTaO<sub>3</sub> with time. The fibroblast cell line REF52 represents a strongly adherent spreading cell line and myeloid leukemia cell line KG-1a a weakly adherent suspension cell type (see chapter 3.1.6) with a higher motility. Simple analysis methods were applied to determine the preferential site for cells to adhere. Due to the unequal sizes of the two cell types and thus their relative size to the polarized domains of the substrate, the center of the nucleus was used as a measure of cell position on the substrate. Pixel analysis on the time lapse images (Figure 75) was conducted to determine the absolute cell center position. The pixel values along the periodicity were binned in five which corresponds to a resolution of 1/7 for the bright stripes (~35 px) and 1/8 for the dark stripes (~41 px).

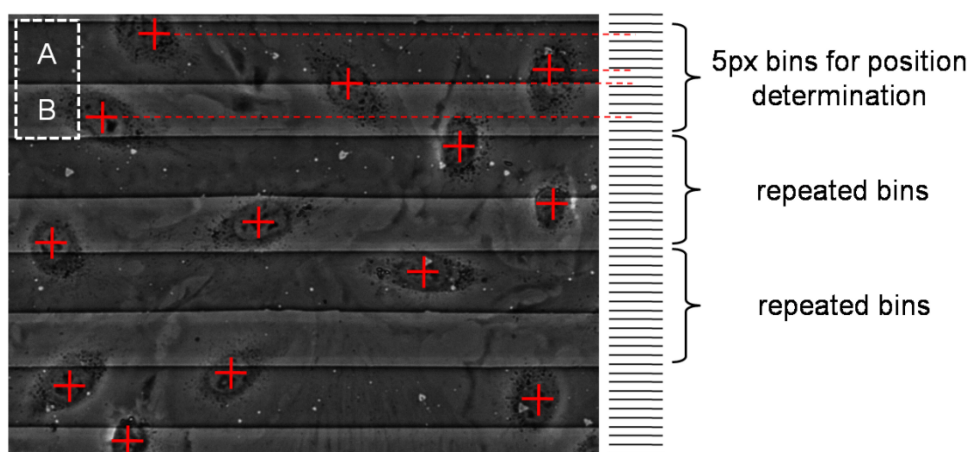


Figure 75: Pixel analysis method for cell position assignment. The nucleus center of a spread REF52 was related to the cell adhesion site position. The pixel value of the lateral position was binned in 5 px. After one period the bins repeat (indicated by the white square of a unit cell with repeating layers A and B) and assignments were added to the upper ones.

Cell position analysis of REF52 on periodically poled LiTaO<sub>3</sub> was conducted on four sample positions with 100 - 150 cells each to a total of ~ 550 cells. The bins of the sections were summed and the cell position analysis displayed for different adhesion times (Figure 76). During initial adhesion of the round fibroblasts the nucleus center showed a random distribution on the period of the polarized stripes. During cell spreading the probability to find a nucleus between the two stripes was strongly diminished.

This observation indicated that spread fibroblasts cells avoid positioning their nucleus on the border between the stripes. In order to prove this observation, pixel analysis was conducted for 11 time points of readily spread fibroblasts which was between 1 h and 18 h and summed up. The mean of four sample positions is displayed in Figure 77. Nearly twice

as many nuclei centers were found in the middle positions of the stripe (~ 40) compared to positions between the borders (~ 20).

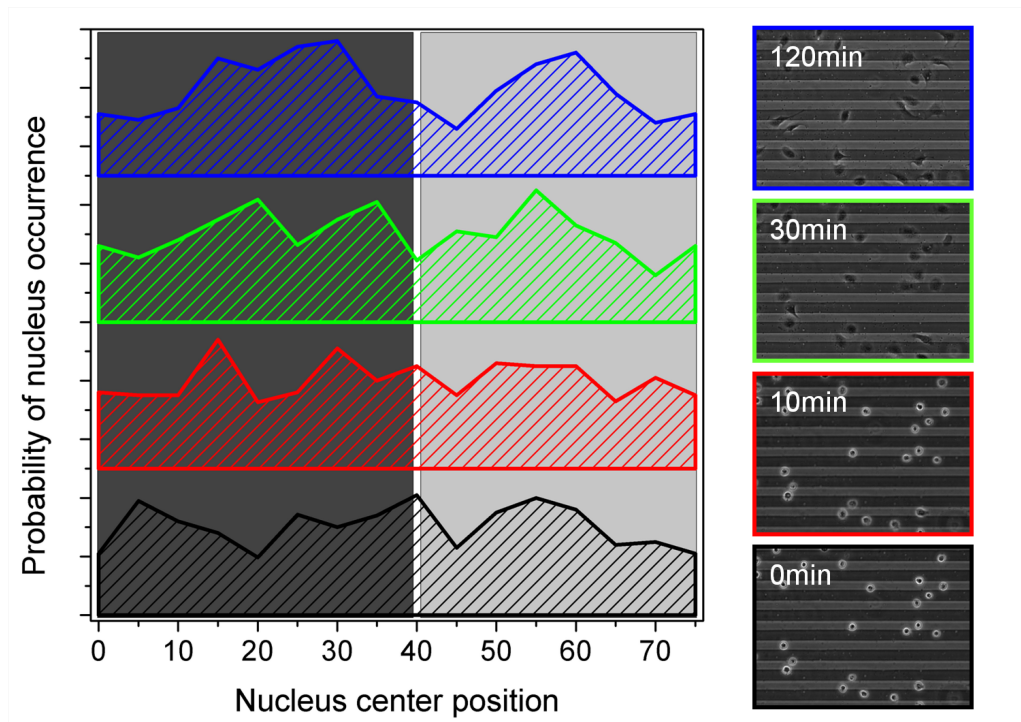


Figure 76: Pixel analysis of cell nucleus position on the (+) and (-) polarized stripes in dependence of cell adhesion time. During initial adhesion the probability of nucleus occurrence was randomly distributed. With increasing spreading, the probability of the nucleus center to be found on the borders between the stripes decreased.

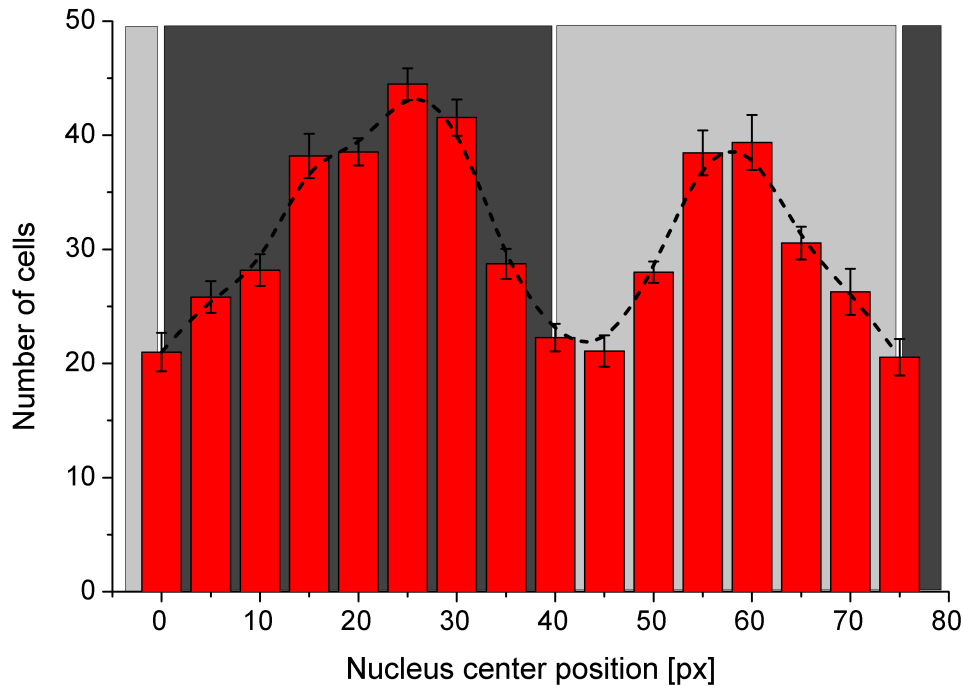


Figure 77: Summed time points of pixel analysis for spread fibroblasts between 1 h and 18 h of cell adhesion. The bars are the mean of four sample position. Error bars indicate the SD. The minima are clearly connected to the borders between two stripes with opposite polarization.

In order to visualize the kinetics of cell reorientation with time, single time points, especially in the initial cell adhesion period had to be analyzed. Because the statistical relevance for one time point was rather low, the mean number of cells per unit area around the middle of the narrow bright stripes (55, 60) and in the middle of dark stripes (15, 20, 25) was summed mean number of cells per unit area of the two borders (35,40,45 and 70, 75, 5) was summed. The ratio of stripe-center to stripe-border was plotted against the cell adhesion time (Figure 78). Again, the evaluation was conducted on all four sample positions. From the exponential fitting curves it was derived that fibroblasts responded to the periodic polarized stripes within one hour of cell adhesion. This was about the time fibroblasts needed to attach, spread and form contacts. Interestingly, between 1 h and 3 h the cells seemed to be particularly sensible to the polarization as the ratio between the center and the border was even higher than several hours later.

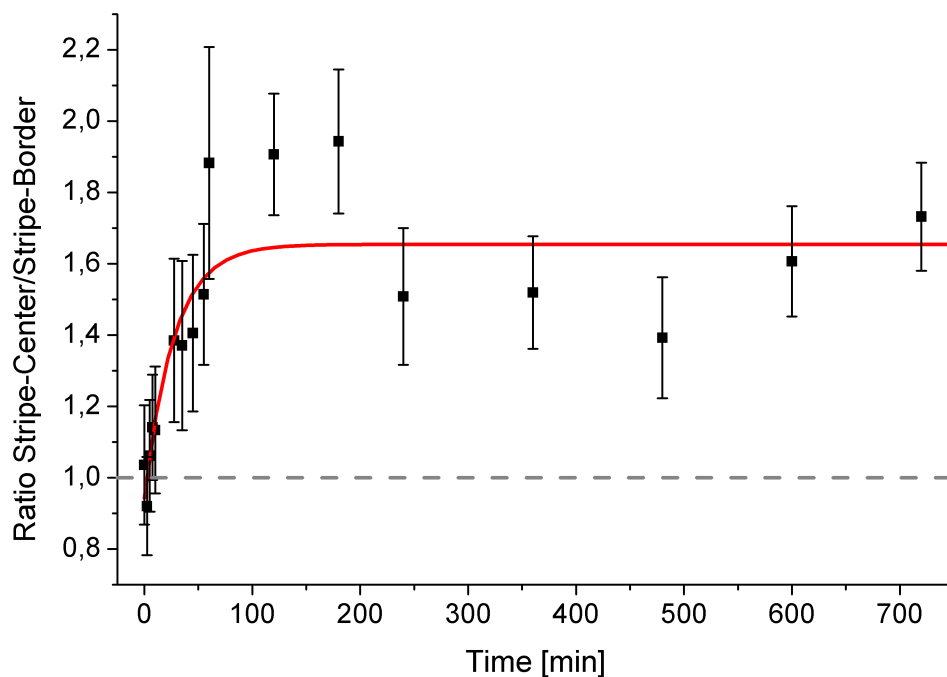


Figure 78: Kinetics of cell nucleus repositioning. Ratio of 15px bins from the middle of the stripes to the borders between the stripes. A ratio of one (gray dotted line) indicates a random distribution of nucleus. An exponential fit curve depicts the cell response behavior. The strongest response was found in the first hour.

From this finding it might be speculated that the formation of adhesion contacts and the cell response to the polarization go in hand and thus the contacts could be involved in replacement of the nucleus by cell movement or even the sensing of a polarization gradient. Still, from imaging of fibroblasts focal contacts (Figure 74) no such conclusion can be drawn as distribution of at least focal contacts is isotropic and the orientation of the elongated cells randomly.

For more clearance on the question of polarity sensing by adhesion contacts, highly motile non spreading cells KG-1a were incubated on periodically poled LiTaO<sub>3</sub> substrates. These do not form strong adhesion contacts and therefore comparing response of KG-1a to

polarization or polarization with the response of fibroblasts might reveal the sensing strategy.

KG-1a cells were seeded onto the periodically poled LiTaO<sub>3</sub> substrate preimmersed in culture medium. After seeding, the cells were imaged by time lapse microscopy for 2 h under physiological conditions inside the incubation microscope. Thermal drift caused a gentle liquid flow in one direction inside the petri dish during experiment causing the cells to move at  $\sim 2 \mu\text{m}/\text{min}$ . This flow phenomenon is quite common in a petri dish and can only be avoided in a controlled environment. Unfortunately, the substrates were not big enough to place these into the microfluidic shear force assay which was capable to keep the weakly adherent leukemia cells under controlled flow (see chapter 4.2.2 and 6.4). Nonetheless cell position pixel analysis was performed every 10 min with a 5 px binning rate as in the case of fibroblasts before. The analysis revealed a slight trend with respect to the lateral polarization position, which was found inside the error bar. This indicated that preferential position effect for KG-1a on periodically poled LiTaO<sub>3</sub>, if at all, was much smaller than for fibroblasts (Figure 79).

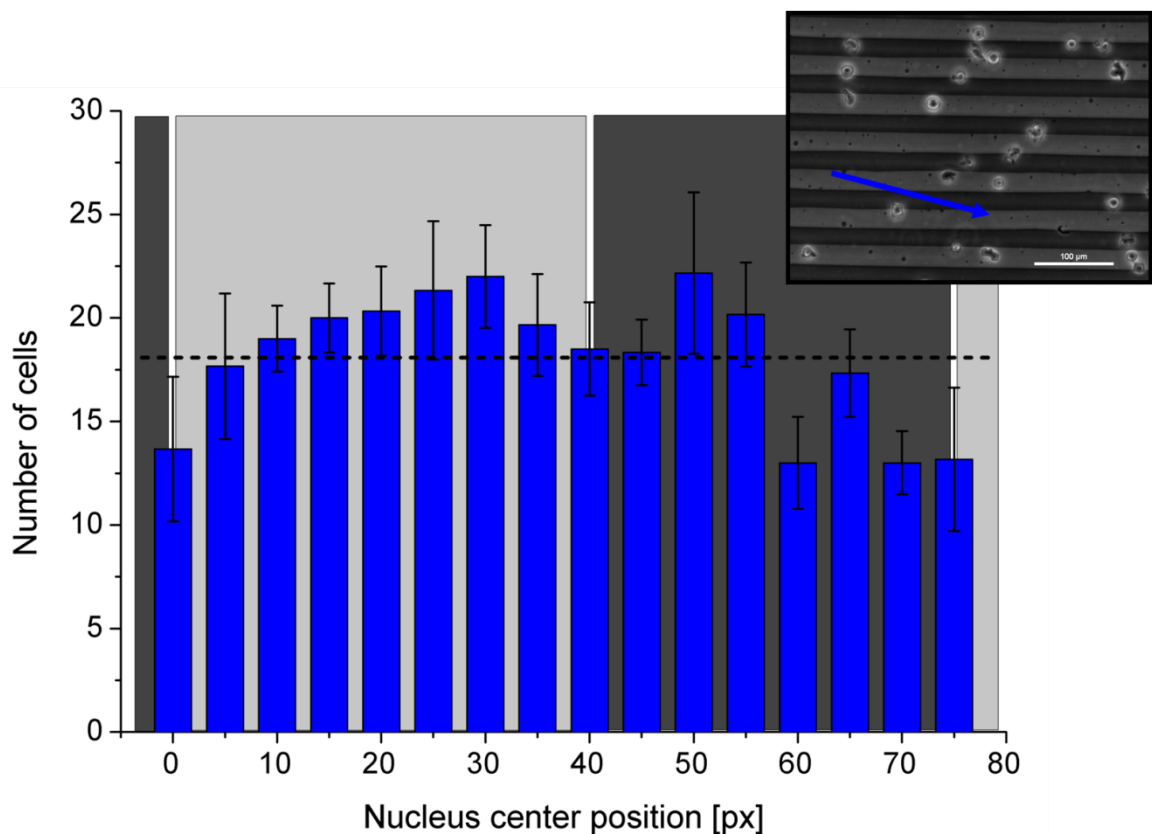


Figure 79: KG-1a leukemic cells on periodically poled LiTaO<sub>3</sub>. Cell position pixel analysis revealed no preferential adhesion site of KG-1a with respect to polarization. Insert: Microscopy image of KG-1a during movement on LiTaO<sub>3</sub>. Blue arrow indicates the liquid flow direction caused by thermal drift.

## 7.4 Discussion

Within this chapter a systematic study on the influence of surface polarization towards cell adhesion was conducted. Adhesion and spreading of fibroblasts was investigated on single poled and periodically poled LiTaO<sub>3</sub> substrates. Fibroblasts cells spread equally on single (+) and (-) poled substrates. Also, uniform spreading over (+) and (-) domain stripes was observed on periodically poled substrates. Random distribution of cell focal contacts over the domain stripes was confirmed by fluorescence microscopy imaging of long term incubated YFP-paxillin REF52 fibroblasts. These results indicate that cell adhesion and spreading process was not affected by the polarization of a substrate. In contrast to that, pixel analysis of the time lapse images revealed that during spreading fibroblasts preferably placed their nucleus in the middle of periodically poled domain stripes. Kinetic analysis revealed that the positioning of the cell nucleus took place on the same timescale as the formation of cell spreading. In the case of weakly adherent suspension cells KG-1a, which were affected by a gentle flow, the pixel analysis showed a random distribution of the nucleus. Cell contacts to the surface may play a role in sensing of surface polarization. The border between the polarization domains showed a steep gradient (see Figure 71, chapter 3.1.5) which might be sensed by cell receptors. As a consequence the cell rearranges itself so that the nucleus, which is a central component for the cell remains unaffected. That the cell does not respond to the polarity itself, but the change of polarity gradient at the border between two opposite polarization domains seems to be counterintuitive on the first sight, but a continuous positive or negative polarization can be seen as a steady environment which is not that disturbing. A simple paradigm to this is the frog in the cooking pot. If the frog is put into the pot and the water heated to boiling it will not jump out but die contrary to the frog being thrown into the hot water – it will jump out of the pot immediately. Finally, the central question in this context – how do cells probe polarity - is still unrevealed as there no receptors for polarity sensing have been reported yet.

## 8 Cell adhesion strength on nanotextured PPX-films

In past rheological work on nanotextured PPX-films showed a strong mechanical anisotropy depending on the tilting direction of the PPX columns [91]. This leads to PPX-film anisotropic wetting [224] and thus to pinning or release of water droplets by means of gravity [90] (see also chapter 2.3.3). These findings were the motivation to investigate the removal of hard spheres and fibroblast cells from tilted poly(p-xylylene) nanorods by the microfluidic shear flow assay and to quantify the influence of flow direction with respect to tilting direction on the critical shear stress needed for cell removal. Therefore a cell adhesion strength assay of REF52 fibroblasts on nanotextured PPX substrates has been conducted, where the detachment force was applied in different directions relative to the tilting direction (Figure 80).

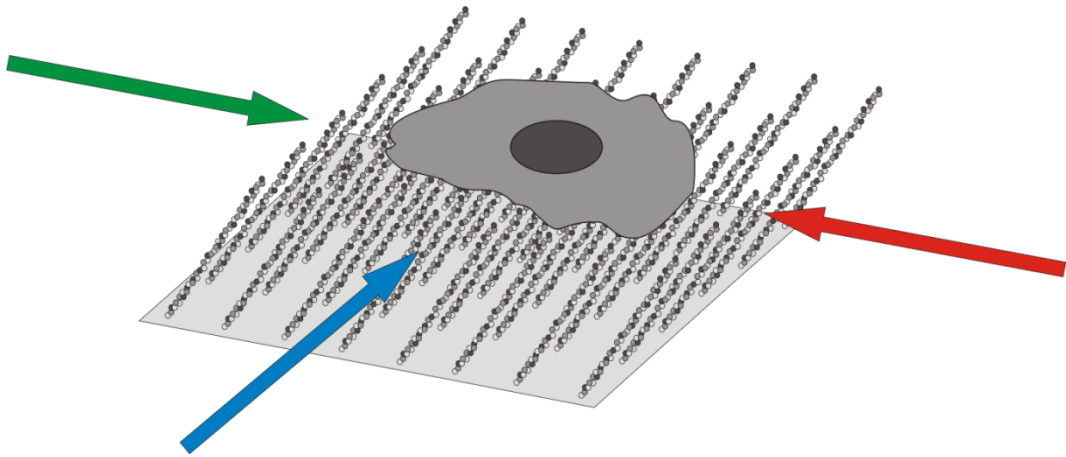


Figure 80: Shear force assay for probing cell adhesion applied “with”, “perpendicular” or “against” the tilting of the nanotextured PPX-film.

### 8.1 Characterization of nanotextured PPX-films

All nanotextured PPX were characterized by electron microscopy (Figure 81) after conduction of the experiments. The substrates were sputtered two times with carbon and SEM measurement was performed at 3 kV and working distance of 3 mm to 4 mm. The mean film height was  $h = 7.0 \mu\text{m} \pm 0.5 \mu\text{m}$  and the tilting angle  $\gamma = 45.7 \mu\text{m} \pm 1.9^\circ\mu\text{m}$ . The mean nanorod length was calculated to  $l = 9.8 \mu\text{m} \pm 0.7 \mu\text{m}$ .

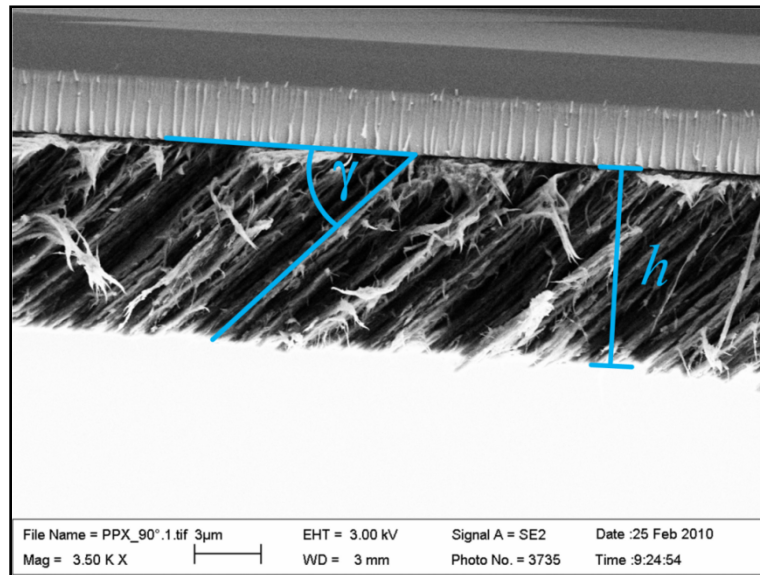


Figure 81: SEM image of a cross section PPX-film on glass substrate. Nanorod tilting angle  $\gamma$  and PPX film height  $h$  were measured for all surfaces.

## 8.2 Microsphere adhesion strength measurements on nanotextured PPX-films

Principally, it can be expected that the interesting aspect of mechanical anisotropy, as it was found for directional friction measurements using the microtribometer [91], may be addressed with a low loading force by the measurement of sphere adhesion strength on nanotextured PPX with the microfluidic shear force assay. The interaction geometry of a spherical particle with a surface, and a microtribometer tip with the surface, are comparable to each other because in proximity to the surface both present a curved body. The reduced loading force of a sphere in the microfluidic setup compared to the tip technique is expected to probe less of the elastic modulus but mainly the contribution of van der Waals interactions to the anisotropy.

PS-spheres with 10  $\mu\text{m}$  diameter were diluted with PBS to  $1 \times 10^6 / \text{mL}$  and injected into a channel with PPX substrate mounted ‘with’ the flow direction with respect to the nanorod tilting. The microfluidic shear force assay was conducted after 5 min of incubation. In order to perform the shear force assay ‘against’ the tilting on the same substrate, flow direction was reversed by swapping the inlet and outlet tubing. The shear force assay was conducted for each direction four times. The mean adhesion strength is the same for force application ‘with’ and ‘against’ nanorod tilting ( $155.5 \text{ dyn/cm}^2 \pm 4.5 \text{ dyn/cm}^2$  and  $155.6 \text{ dyn/cm}^2 \pm 1.8 \text{ dyn/cm}^2$ ) (Figure 82). Thus, no directional dependent adhesion strength for polystyrene spheres was observed. Also, the adhesion strength of PS-spheres on the textured PPX was only about half the value found on flat C12-SAM (see chapter 4.4.2), which was mainly attributed to the reduced surface contact of the sphere.

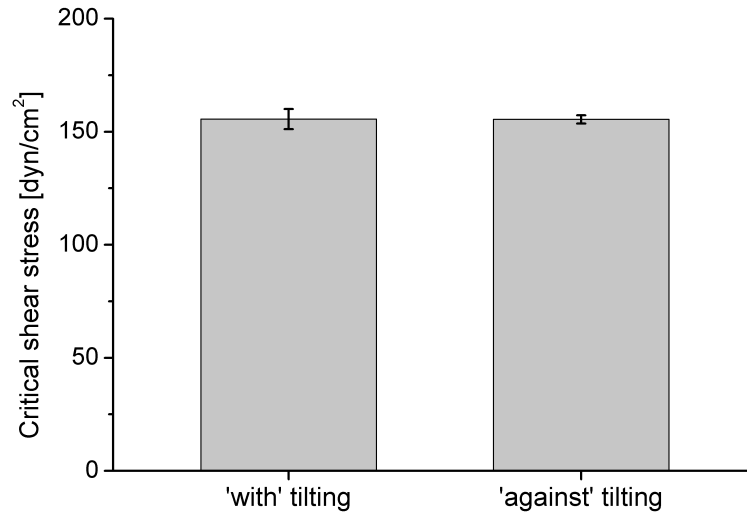


Figure 82: Mean PS-sphere adhesion strength 'with' direction of the PPX tilting and 'against' it. PS-sphere adhesion is equal for both directions of force application.

### 8.3 Cell adhesion strength measurements on nanotextured PPX-films

The finding that passive sphere attachment did not show anisotropic adhesion strength at low loading indicated that a minimal force is essential to probe surface anisotropy. Adherent cells can interact actively with the surface and cell spreading results in a much higher contact area with the substrate than the spheres. Thus, cells are likely comparable with a sessile liquid droplet on the substrate which shows anisotropic wetting on nanotextured PPX [90]. In order to investigate the surface anisotropic effect towards cell adhesion, the adhesion strength of fibroblast cells was measured with respect to the direction of force application inside the microfluidic shear force assay.

Three PPX samples were mounted in the microfluidic channel in the desired orientation (with, against, perpendicular) to measure force directional dependence of adhesion strength. Rat embryonic fibroblasts REF52 were harvested and injected into the channel and incubated for 5 h. Afterwards the microfluidic shear force assay for ~ 250 cells in each channel was carried out. The morphology of the cells appeared to be well spread, as found on a reference glass substrate in a fourth channel. The decrease of adherent cells over time was measured against the applied shear force. The weakest adherent fibroblasts were removed from the nanotextured PPX surface at shear forces exceeding 100 dyn/cm<sup>2</sup> (Figure 83). The critical shear stress was determined by four independent experiments for each tilting direction. The analysis revealed that cells were removed at higher critical shear stress if the shear force was applied 'against' and 'perpendicular' the tilting direction (705 dyn/cm<sup>2</sup> ± 63 dyn/cm<sup>2</sup> and 695 dyn/cm<sup>2</sup> ± 34 dyn/cm<sup>2</sup>, respectively), but at much lower flow 'with' nanorod tilting (465 dyn/cm<sup>2</sup> ± 48 dyn/cm<sup>2</sup>) (Figure 84). For

comparison, removal from a glass slide usually required a critical shear flows around  $700 \text{ dyn/cm}^2$  (see chapter 4.5.2 and 4.5.3).

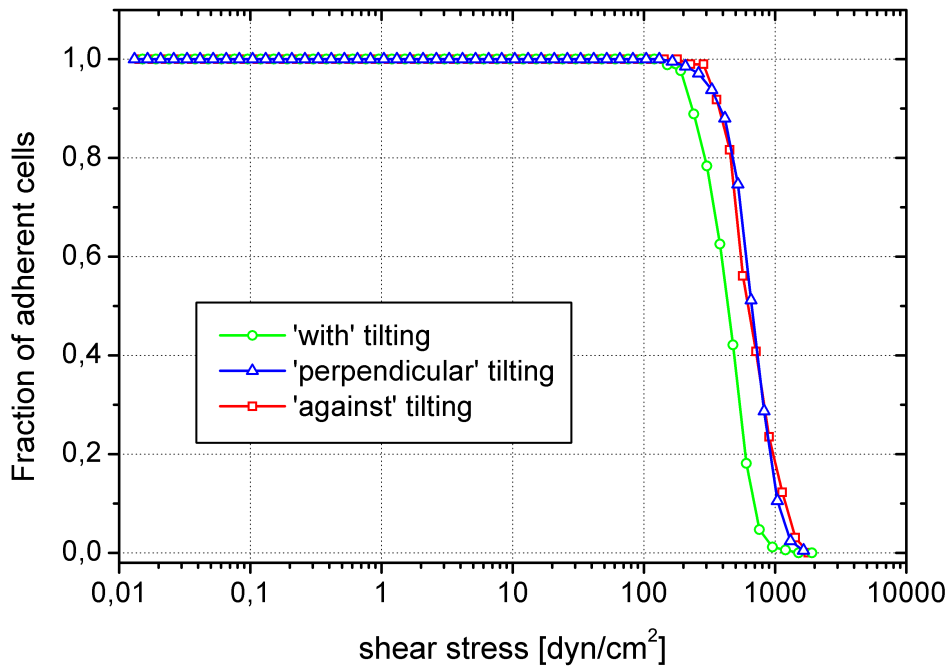


Figure 83: Exemplary detachment curve for fibroblast adhesion strength on nanotextured PPX-films. Each curve represents the detachment of  $\sim 250$  cells. The adhesion strength was higher for shear flow applied against (circles) and perpendicular (squares) tilting of PPX-films then for flow with tilting direction (triangles).

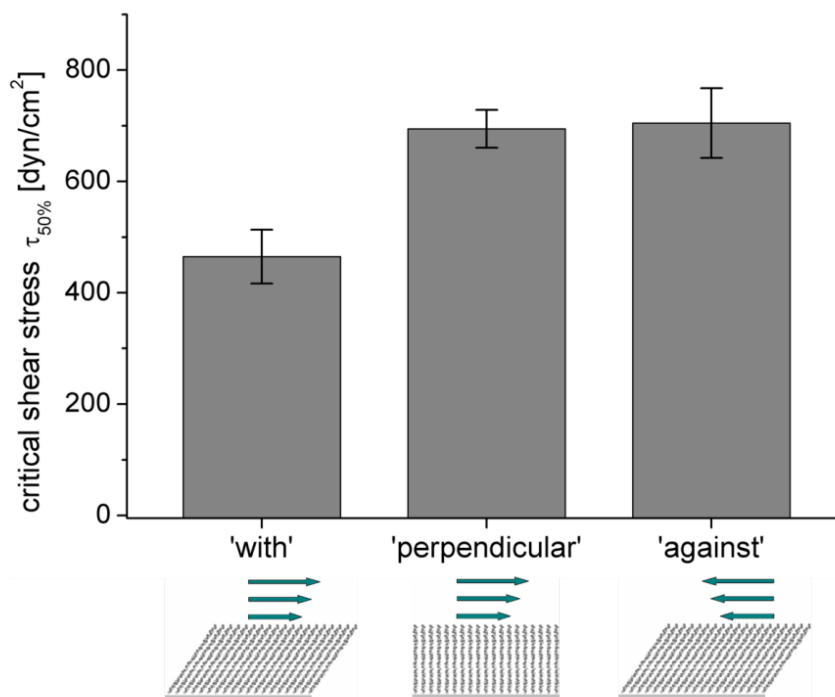


Figure 84: Adhesion strength of REF52 fibroblasts on nanotextured PPX-films. Mean measured adhesion strength out of four independent experiments. The critical shear stress necessary for cell removal against and across nanorod tilting direction is higher compared to flow into nanorod tilting direction. Error bars are the standard error.

To assure that anisotropic removal of fibroblasts from nanotextured PPX was not an effect of nanorods being damaged by the liquid flow, the PPX substrates were investigated by SEM after the experiment. SEM images of the PPX substrates revealed intact nanorods but the shear flow caused a change in surface morphology as linear faults perpendicular the nanorod tilting direction appeared (Figure 85b). These structures were not visible at the pristine surface (compare with Figure 86a) and also not outside of the flow channel (Figure 85a). The faults only appeared after a flow was applied, no matter in which direction the force resulted with respect to tilting. As expected, the faults were always perpendicular to the tilting direction.

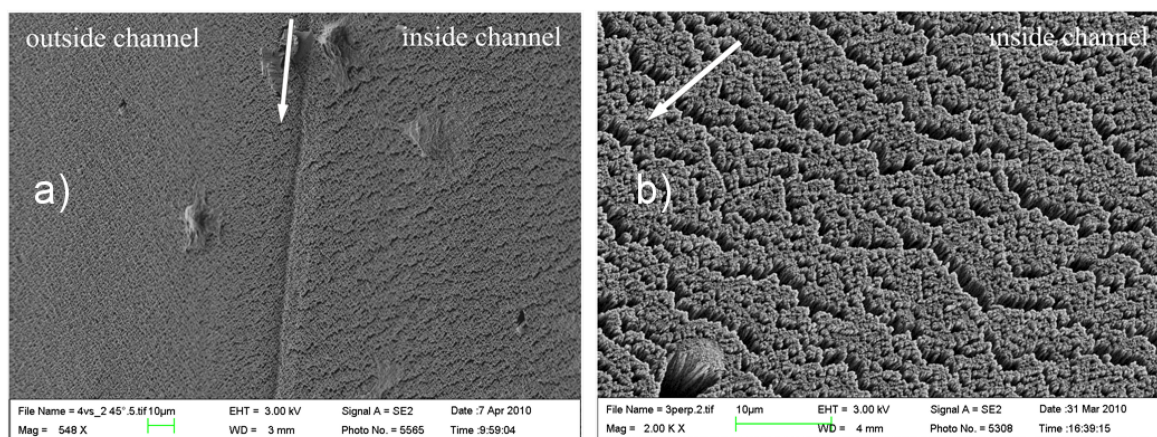


Figure 85: SEM image (500 x) of PPX surface inside and outside the former channel location (a). At higher magnification (2000 x) on the surface exposed to the channel fault defects are visible (b). The faults are, independent of the liquid flow direction but perpendicular to the nanorod tilting direction (white arrow).

#### 8.4 Cell adhesion and morphology on nanotextured PPX-films

The light microscopy images from the channel experiments did not reveal the actual cell adhesion morphology due to diffusive light scattering of the nanorods. Morphological analysis of fibroblasts on pristine nanotextured PPX were carried out by SEM analysis on rat embryonic fibroblasts which were cultured for 5h on PPX-films. The fixed and critical point dried cells were investigated with scanning electron microscopy to image cell morphology and the contacts established towards the substrate (Figure 86). Most of the cells were spread out well and established filopodia comparable to glass or polystyrene substrates (a). Images at higher magnifications (Figure 86c, e, f) visualize that some of the peripheral filopodia attached in the randomly distributed defects between the nanorods. To reveal how deep the filopodia penetrated into the defects, a sample was fractured and imaged by SEM (Figure 87). The filopodia penetrate up to 0.5  $\mu\text{m}$  inside the substrate defects as estimated from the SEM images (b, c).

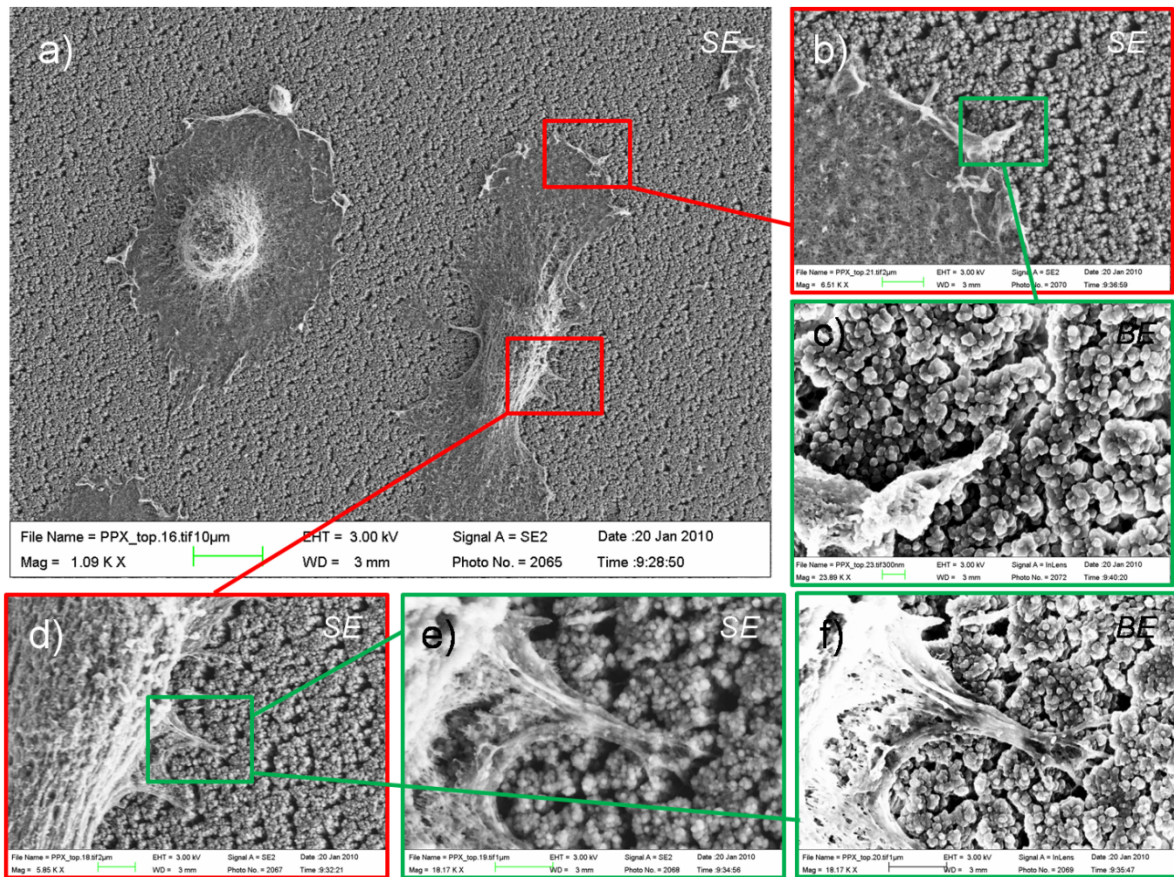


Figure 86: SEM images with backscattered and secondary electrons of REF52 fibroblasts attached to PPX substrates. Cell filopodia show attachment in the holes between the nanorods (c, e, f) at high magnifications (18000 x and 23000 x)

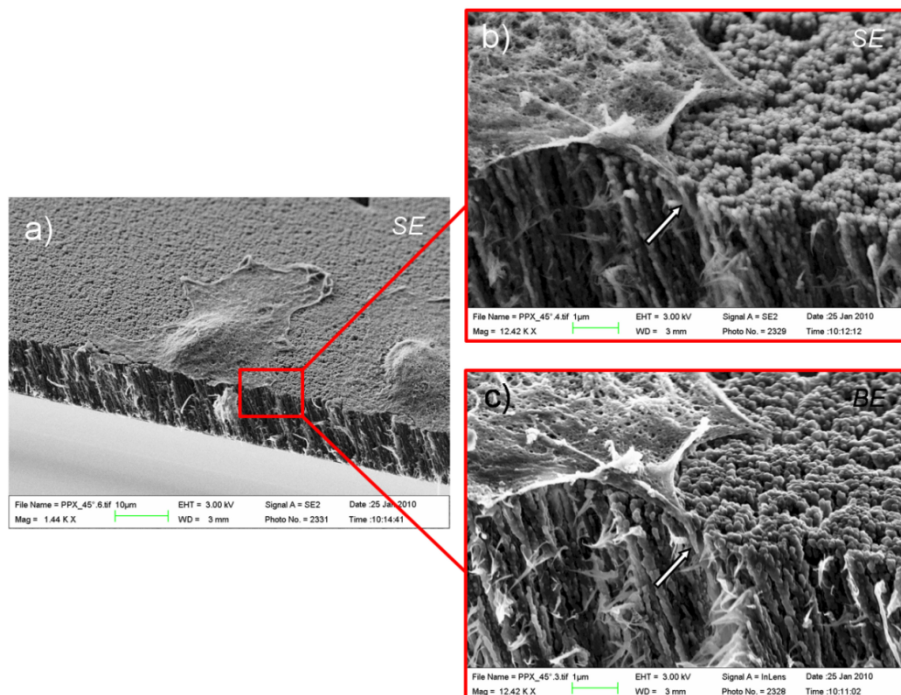


Figure 87: SEM image of REF52 fibroblasts at the edge of a cut PPX substrate (a). High magnification images (b, c) show cell filopodia (arrow) reaching  $\sim 0.5 \mu\text{m}$  deep into the holes.

## 8.5 Discussion

The ability of PPX surfaces with tilted nanostructures and anisotropic wetting properties to alter forces needed for removal of spherical particles or cells from the surfaces was investigated. In the microfluidic shear force assay it was found that the removal of PS-spheres was equal for force application ‘with’ nanorod tilting ( $155.5 \text{ dyn/cm}^2 \pm 4.5 \text{ dyn/cm}^2$ ) and ‘against’ it ( $155.6 \text{ dyn/cm}^2 \pm 1.8 \text{ dyn/cm}^2$ ). This finding emphasizes that the effect of surface anisotropy vanishes with at low loading force and thus mechanical properties of the nanorods are responsible for anisotropic resistance.

The results on the removal of actively adhering cells were different. It was shown that mammalian fibroblast cells adhered and spread well on nanotextured PPX films. The cell adhesion strength, measured by the shear force assay, showed to be dependent on the direction hydrodynamic forces were applied with respect to the nanorod tilting. As derived from the electron microscopy images, the filopodia anchored in the substrate as they were able to penetrate in between nanorods. The faults which result from initial flow in the channel experiments might have even enhanced the probability of filopodia to attach into the substrate. This leads to a possible explanation for the increased capability of the cells to withstand the fluid shear stress when flow is applied ‘against’ or ‘perpendicular’ to the tilting direction of the PPX nanorods. As shear stress was applied, forces were exerted parallel to the substrate and operate ‘with’ anchoring direction ( $46^\circ$ ) or ‘against’ it ( $134^\circ$ ) as sketched in Figure 88. This directionality of anchoring could be one reason for the reduced critical shear stress necessary to remove the cells, independent on the cells elastic modulus. If the cell is considered as an elastic body, the leading edge for detachment would form easier with the tilting direction, because against tilting direction the material need to form the edge has to be transported around the corner from the surface defect. In the case the cell is considered as a rigid object, the torque on the cell body will cause the cell to detach. Here, the filaments can easier be pulled out of the polymer when the shear force is applied ‘with’ the direction nanorod tilting.

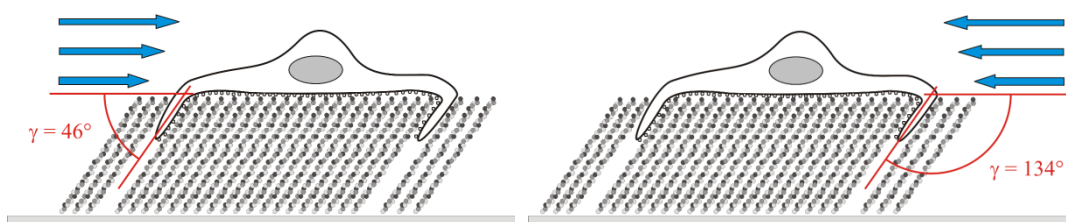


Figure 88: An artistic sketch of cell filopodia attaching in the defect holes of  $46^\circ$  tilted PPX-film. In dependence of the flow direction the angle between adhesion forces and hydrodynamic shear force varies.

A second way of interpreting the data might be connected with the compressibility of the nanorods which should cause a compression of the film when the shear flow is applied ‘with’ the tilting direction while a shear flow ‘against’ the tilting direction most likely

leads to an adverse effect. A third explanation is the previously described ratchet model which is responsible for the anisotropic wetting behavior [90] and causes a water droplet to roll towards the tilting direction of the nanorods.

The compressibility effect of the nanorods is less likely to contribute to the isotropic cell detachment. The PPX substrate is relatively stiff and the wall shear stress applied by the flow does not exceed  $1000 \text{ dyn/cm}^2 = 100 \text{ Pa}$  which is not likely to cause major nanorod deformation. Also the channel height would increase for the 'with' direction which would lower the effective shear stress and cell rather detach at higher volume flows.

The ratchet mechanism for anisotropic wetting of a water droplet on PPX occurs in the three phase system solid/liquid/air. In the present experiments solid/"solid-liquid"/liquid phases appear so the material density and tensile forces, between the media are much less. But these tensile forces, especially the presence of air pocket between the object and the surface, are essential for the ratchet mechanism. In summary it can be supposed that most probably anchoring of the fibroblasts by filopodia penetrating into the substrate is the main effect behind the force directionality dependence of cell adhesion strength on anisotropically textured PPX.

## 9 Visualization of cells using high resolution imaging

In this chapter the preparation of adherent cells for the visualization of structural features under ultrahigh vacuum conditions by X-ray imaging is described. Also first results for visualizing of the adherent cells using two different holographic imaging approaches with soft X-rays are presented. The particular strength of X-ray imaging techniques is the capability to exploit intrinsic material contrast instead of labeling cells with fluorophores to reveal ultrastructural features (see chapter 2.4).

The adherent cells were prepared, critical point dried and imaged during the preparation processes via visual light microscopy including different contrast techniques and fluorescence. Imaging of adherent biological specimen was performed in the HORST-chamber (Holographische Röntgen Streuapparatur) [225] at ultrahigh vacuum conditions in a cooperative work of Dr. R. Heine, Dr. F. Staier, T. Gorniak and T. Senkbeil. Coherent light sources for imaging were beam lines at the synchrotron radiation facility BESSY II in Berlin and the free-electron laser facility FLASH in Hamburg. Generally, holography offered the outstanding capability of gaining 3D information by recording a single 2D image only as described in detail in the thesis of R. Barth [102]. Two different experimental approaches were realized to generate a divergent light cone which is required for digital holography. The classical approach is the application of pinholes and the more recent one the utilization of zone plates which are both described in detail in the diploma thesis of T. Gorniak [226]. Technically, holographic images resulted from the acquisition and subsequent accumulation of a set of recordings from the specimen, which were then reconstructed by the mentioned coworkers.

The final goal of this work was to establish preparation concepts to conserve cellular material for X-ray imaging. Resolving ultrastructural features regarding cell adhesion which are particularly important to reveal the adhesive sites as e.g. for the anisotropic adhesion of fibroblasts on textured PPX which was described in chapter 8. There, most of the adhesion sites were located below the cell body and thus were not accessible by SEM (see chapter 8.4).

### 9.1 Preparation of adherent cells for X-ray holography studies

Adherent cell line REF52 and fluorescent clones of the H1299 cell line were cultured and harvested according to the protocol (see 3.1.6). Afterwards, according to critical point drying protocol (see 3.1.7) a few cells were seeded on 30 nm to 100 nm thin SiN membranes, which were precoated with 1 mg/ml fibrinogen. Special care was taken to seed only ~ 10 cells onto the 1 mm x 1 mm membrane to assure imaging of separated cells afterwards. After 4 h to 5 h the cells were fully spread and did not start to proliferate. The cells were then fixed with PFA and the membrane was imaged by phase contrast or

brightfield microscopy. In the case of H1299 cells also fluorescence microscopy was performed on single cells. After fixation the cell water was exchanged by ethanol and critical point drying the whole membrane was imaged with phase contrast, brightfield and reflection DIC microscopy. After X-ray imaging the samples were imaged again to reveal, if radiation damage occurred during the measurements.

## 9.2 Digital in-line holography using pinholes

Holographic imaging with pinholes was accomplished at the beamlines PG0 and PG2 at FLASH using a fundamental wavelength of 8 nm.

Imaging of REF52 fibroblasts with a 1  $\mu\text{m}$  pinhole at PG0 was accomplished by five acquisitions of 60s exposure time each and revealed an estimated resolution of  $\delta = 620$  nm. As holography obtains depth information, the reconstruction was compared to a light microscopy phase contrast image with high focal depth and thus a relatively low numerical aperture (Figure 89). The reconstruction of the central part of a fibroblast (Figure 89b) shows a good correlation of intracellular structures with optical microscopy images (Figure 89d). The strongest contrast and lowest transmission is found in the nucleus where the material density is the highest.

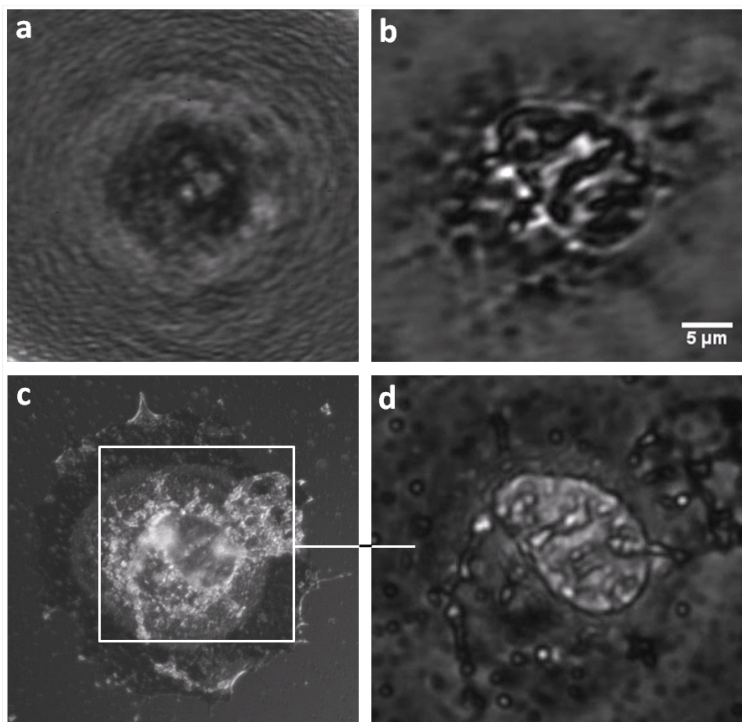


Figure 89: A REF52 fibroblast cell on a 100 nm thick SiN-membrane. (a) Hologram recorded at a wavelength of 8 nm for 5x 60 s illuminated through a 1  $\mu\text{m}$  pinhole. (b) Reconstruction of the hologram. The resolution was estimated to be 620 nm. (c) Reflection DIC microscopy image, taken with a 100x, N.A. 0.9 objective. (d) Close-up of the nucleus phase contrast image taken with a 20x Ph1, N.A. 0.45 objective.

In another experiment adherent H1299 lung carcinoma cells were imaged at the beamline PG2. The pinhole diameter was 1.2  $\mu\text{m}$  and the exposure time was 10x 1 s. The single holograms were laterally randomly displaced on the detector chip and had to be pixel shift corrected for each exposure. Still, the resolution of the reconstruction (Figure 90c) was calculated to be only 950 nm. Most likely the displacement effect was due to both the instability of the beam and experimental setup itself. Again, the reconstructed images of the cells showed high contrast (Figure 90c). The shape and some cell structural features correlate with the light microscopy phase contrast image (Figure 90a).

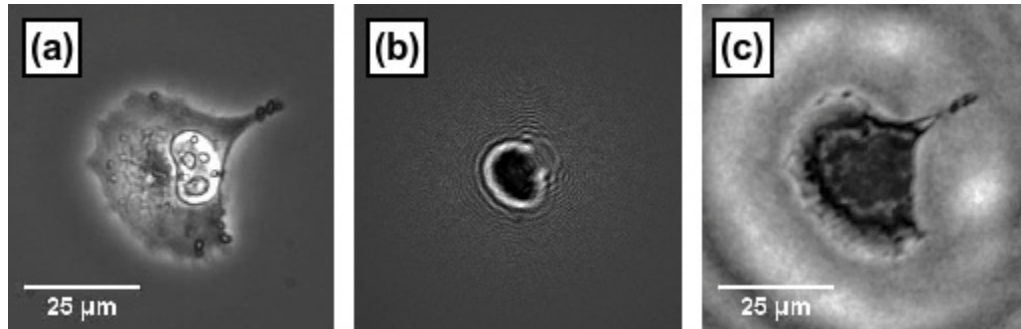


Figure 90: A H1299 lung carcinoma cell on 75 nm thick SiN-membrane. (a) Phase contrast microscopy image taken with a 20x Ph1, N.A. 0.45 objective. (b) Hologram recorded at a wavelength of 8 nm for 10x 1 s illuminated through a 1.2  $\mu\text{m}$  pinhole. (c) Reconstruction of the hologram. The resolution of the reconstruction was estimated to be 950 nm.

### 9.3 Digital in-line holography using zone plates

A recent approach in X-ray digital in-line holography is the use of zone plates to generate a divergent light cone. Zone plates are able to focus an X-ray beam to a small spot, like to a glass lens focusing visible light. The advantage of using zone plates compared to pinholes is the low beam intensity needed for imaging which results in a short acquisition time.

Lung carcinoma cells H1299 were imaged at the undulator beamline UE52SGM at BESSY II. A zone plate with a diameter of 90  $\mu\text{m}$  and an outermost zone width of 80 nm was used. 20 holograms with an exposure time of 0.5 s each were recorded and accumulated with an X-ray wavelength of 4.96 nm. For the reconstruction a resolution of  $\delta = 326 \text{ nm} \pm 90 \text{ nm}$  was measured which was mostly limited by beam incoherence. The comparison of reconstruction images (Figure 91e) with transmission light microscopy images (Figure 91c and d) of the same cell showed a strong correlation between most of the cellular features. The reconstruction of the cell nucleus (Figure 91h) revealed nucleoli which were not resolved in a high resolution DIC reflection microscopy image (Figure 91g) but it was possible to correlate this additional with the stained nucleoli which was observed by fluorescence microscopy (Figure 92).

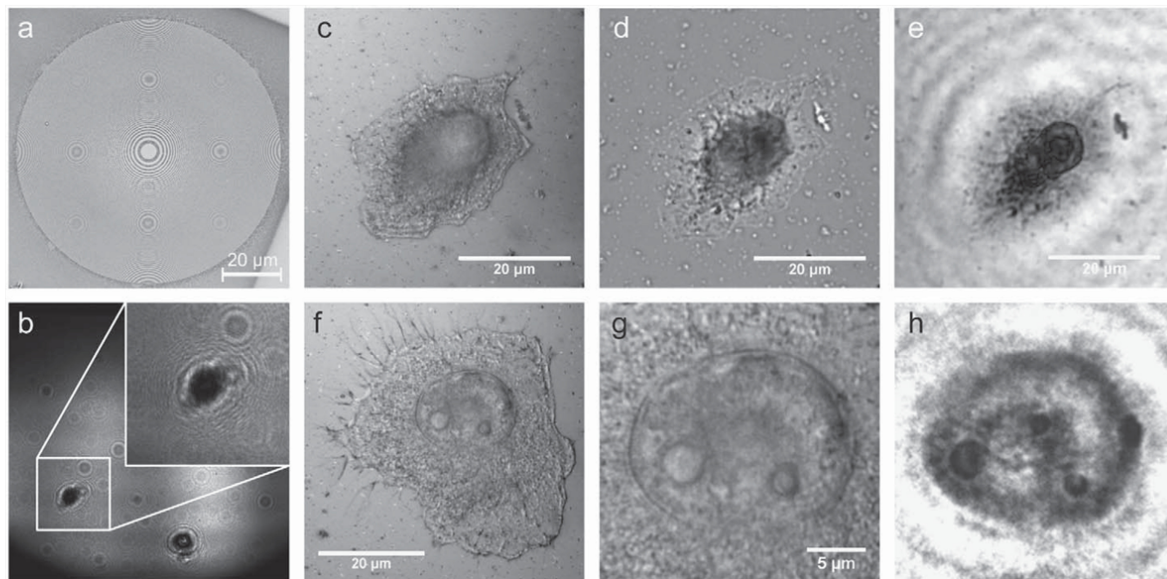


Figure 91: A H1299 lung carcinoma cell on a 75 nm thick SiN-membrane. (b) Hologram recorded at 250 eV ( $\lambda = 4.96$  nm) for 20x 0.5 s using a zone plate (a). (c, f) Reflection DIC microscopy image, taken with a 100x, N.A. 0.9 objective. (d) Same image section as (c) but taken in transmission mode. (g) Magnification of (f). (e) Reconstruction of the hologram for comparison with (c, d). (h) Reconstruction of the hologram for comparison with (g). The mean resolution in the reconstruction was estimated to be 326 nm.

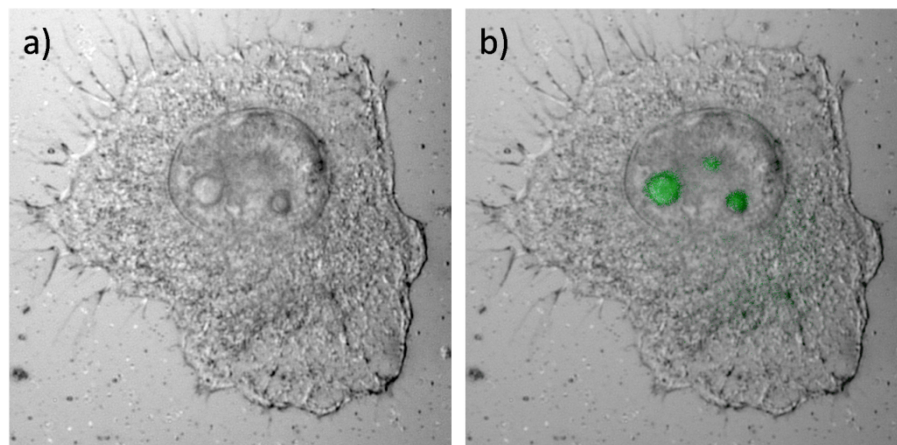


Figure 92: A H1299 cell on 75 nm thick SiN-membrane. (a) shows the same reflection DIC microscopy image, as in Figure 91h. (b) An overlay of (a) with the fluorescence microscopy image of fluorophore expressing nucleoli.

In the next step the cell nucleus was imaged with X-rays of photon energies within the water window. In the wavelength region of 2.3 nm to 4.3 nm X-rays have a significantly shorter absorption length for essential trace elements and carbon than for water [227]. Due to the resulting material contrast images of elemental distributions and their quantification can be achieved within this wavelength window. In order to measure in the water window the 3<sup>rd</sup> harmonic of the beamline PG2 at FLASH was utilized. The beam with a wavelength of 2.68 nm was focused by a 100  $\mu$ m zone plate with an outermost zone width of 35 nm some millimeters upstream of a fibroblast cell. Four holograms were recorded with an

acquisition time of 600 s each. The measured resolution for the image was  $\delta = 485 \text{ nm} \pm 88 \text{ nm}$ . The resolution limitation was mostly attributed to geometric and coherence aspects. Again, the cellular features of the reconstructed holographic image (Figure 93d) match well the corresponding features imaged by high numerical aperture objective in transmission mode of optical light microscopy (Figure 93c). In magnification images of the nucleus the different material contrast of X-rays compared to visible light becomes clear. In the visible light image (Figure 93e) four features are visible whereas in the reconstruction (Figure 93f) there is only one. This can be attributed to an unequal material composition or material density of the nucleoli.

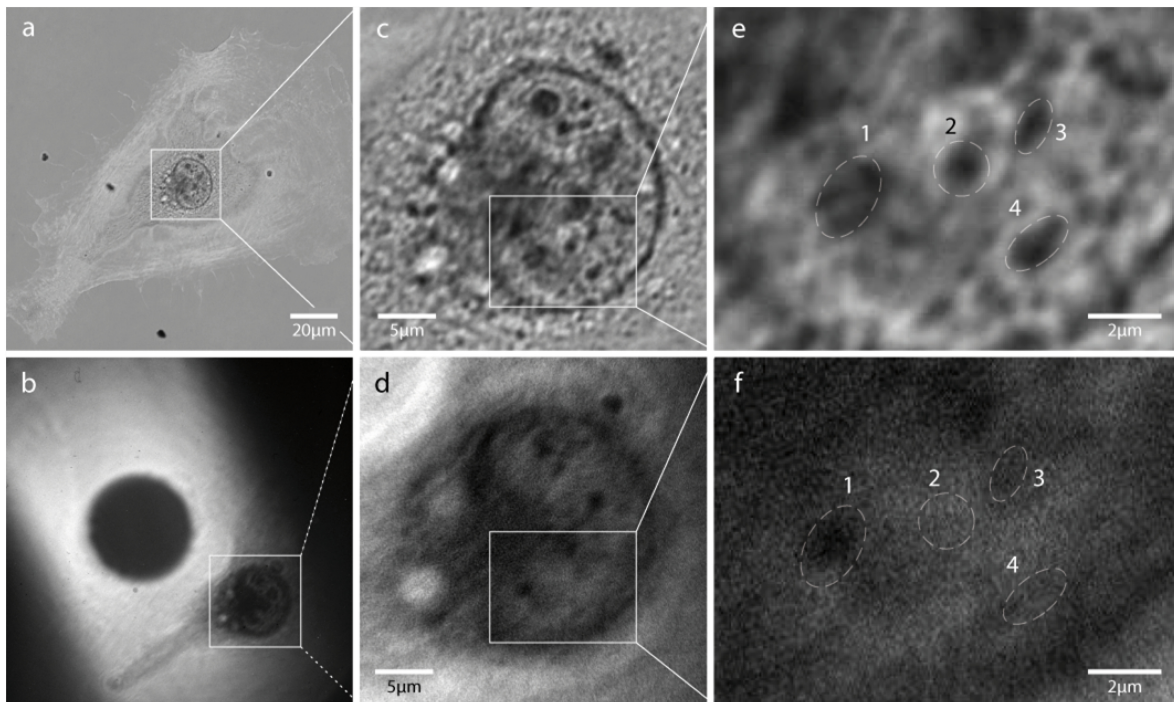


Figure 93: A REF52 fibroblast cell on 75 nm thick SiN-membrane. (a) Transmission light microscopy image taken with a 100x, N.A. 0.9 objective and its magnified images (c) and (e). (b) Hologram recorded at a wavelength of 2.68 nm for 4x 600 s trough a zone plate. (d) Reconstruction of the hologram section in (b) and its magnification in (f). Mean resolution is estimated to be 485 nm.

## 9.4 Discussion

In this work preparation protocols for X-ray imaging at ultrahigh vacuum conditions were established which show a good preservation of the cellular features. The first holographic imaging experiments of adherent cells using soft X-rays revealed image resolutions almost comparable to common transmission light microscopy, even though the overall image quality was much lower. The application of zone plates instead of pinholes led to an increased resolution of the reconstructed images which was partially due to the very low acquisition times needed because beam instabilities and sample drift were minimized. Structural components inside the nucleus were resolved and interestingly some features appeared in the reconstructed holograms which were not visible in the light microscopy

images but by fluorescence microscopy, which encourages further experiments for the correlative approach. This finding demonstrates the differing contrast generation mechanisms of visible light and X-rays, latter have a much lower probability to be scattered by the sample material. This and the fact diverse contrast techniques were used in light microscopy some features appeared in inversed contrast. Images from brightfield transmission mode microscopy matched the contrast obtained by holography most, which can be explained with the similarities of the illumination geometry. It was also shown that imaging in the water window using the 3<sup>rd</sup> harmonic is in principle possible.

Still, these results were encouraging and continuous improvement of the technique. The application of zone plates is promising to achieve higher resolution, especially if the quality of the beam by means of flux and coherence is improved and fundamental wave lengths in the water window become available. In order to take advantage of the water window the next step will be the implementation of cryo technique into the setup in order to image frozen adherent cells in their preserved native state.

## 10 Summary and Outlook

In this work a microfluidic shear force setup was build to measure cell adhesion strength. The setup had to fulfill challenging demands with respect to application flexibility, range of force application, sample throughput and robustness. These were met by a sophisticated setup design and elaborated protocols for sample preparation, experimental procedure and data evaluation. By utilizing microfluidics in form of a custom build setup housed inside an incubation microscope, the cells were put into a controlled geometrical and chemical environment which allowed long term cell adhesion for up to five days. The application of controlled shear force, by means of a well characterized liquid flow, was used to probe cell-surface interactions. The interactions could be measured quantitatively for about 300 cells experiment, which allowed direct comparison of cell adhesion strength between different kinds of substrates. Especially parallelization of the experiment increased the comparability through compensation of biological variability.

Investigations on adhesion strength of spherical microparticles demonstrated the capability to determine receptor-ligand binding strength of biotin/streptavidin system and to probe hydrophobic interactions between PS-spheres and C12-SAMs. For biological specimen experimental parameters were determined for adhesion strength measurement of fibroblast cells. The cells response to continuous flow was found to be sensible and thus the flow duration kept to a minimum, which is well below the assay times reported for this kind of setups so far. Thereafter the influence of the surface properties hydration, bioactivity, polarity and topography towards the adhesion of mammalian cells was studied systematically.

Using SAMs as a model surface, the influence of surface hydration towards cell adhesion was investigated on oligo(ethyleneglycol). The degree of hydration was tuned by varying the terminal chain length from one to six EG units. It was shown that the cell adhesion strength decreases with the factor of ten for each additional EG unit beginning from one EG. This leads to a cell adhesion resistant surface for three EG units – a result which is in line with observations for marine microorganisms. Additionally, the spreading behavior was correlated to cell adhesion strength by measurement of projected cell surface area and detachment shear stress for each cell independently. It was shown that cell adhesion strength directly increases with cell spreading on small spreading areas. For larger cell spreading areas the adhesion strength turned out to be area independent and that surface properties only determine the adhesion strength, which is in line with the zipper mechanism for cell detachment.

Another type of highly hydrated surfaces are the protein and cell repellent polysaccharides. The application of HA and AA as substrates in the microfluidic shear force assay revealed that fibroblasts adhere as weak as on EG3OH SAMs. In contrast to that, the weakly adherent blood related leukemic cell lines and HPCs expressing the CD44 showed shear stress induced adhesion and rolling on HA and cells were accumulated at shear stress

above  $0.2 \text{ dyn/cm}^2$ . Based on the onset shear stress for this cell adhesion and bond strengthening with increasing shear stress it was emphasized that the mechanism is similar to the selectin based leukocyte rolling. Even though it was not clarified that the adhesion was due to the specific interaction between CD44 cell receptor and the pure HA surface all observations pointed to these specific receptor-ligand interactions. More important is the fact that this was the first time that rolling and flow induced and regulated adhesion of hematopoietic progenitor cells on hyaluronan has been observed. The shear stress regulated adhesion on HA is especially interesting as the CD44/HA interaction plays an important role for homing and engraftment of HPCs into the bone marrow. Possibly the mechanism of HPC and leukemic cell adhesion on HA might be similar to the one discussed for selectin based leukocyte rolling in inflammatory response and thus the shear stress regulated adhesion represents a more general principle than so far anticipated. Future studies will focus on experiments with antibodies to clarify the specificity of CD44 interaction with HA and on experiments with clinical relevant primary cell material to finally reveal the importance of HA for the homing and engraftment of human hematopoietic stem cells into the bone marrow. At the bottom line these findings may be useful to develop new strategies for the enrichment of hematopoietic stem cells which are needed for the treatment of leukemia.

Besides the control of cell adhesion by receptor-ligand interactions, the impact of surface polarity towards the adhesion of mammalian cells was investigated using permanently poled ferroelectric surfaces. The adhesion and spreading of fibroblasts was investigated on single poled and periodically poled  $\text{LiTaO}_3$  substrates. Even though fibroblast cells spread equally and uniform on single (+) and (-) poled substrates and a random distribution of cell focal contacts was found, a distinct cell response was observed. It was shown that not the polarity itself, but the change of polarity at the border between two opposite polarization domains caused the fibroblasts to withdraw their nucleus from these borders. This cell response took place while the cell spread over the surface and focal adhesions were formed. Still it remains unknown if the steep polarization gradient which might be sensed by cell receptors and thus the cell rearranges itself so that the nucleus, which is a central component for the cell remains unaffected. The central question arising from this study is how do cells probe polarity gradients as there no receptors for polarity sensing have been reported yet.

Fibroblasts were also used to clarify the impact of anisotropic textured surfaces towards cell adhesion. Anisotropic textured PPX films, which were synthesized via oblique angle CVD of pyrolysed paracyclophane by collaborators, consist of densely packed nanorods which are tilted with respect to the surface normal. Even though the anisotropic surface friction and wetting has been reported for this surface, the effect vanished for force directional measurement of Ps-sphere adhesion strength. Contrary, the measurement of adhesion strength for the active adhering fibroblast cells showed force directional dependence on the anisotropic PPX. The cells were removed at similar shear stress when

force was applied against and perpendicular the nanorod tilting and about 34 % less for force applied with the tilting direction, which is in line with reports for the anisotropic wetting. The mechanism could not be described by the ratchet mechanism from the wetting theory but by the attachment of filopodia into the defects between the nanorods which was revealed by scanning electron microscopy.

The visualization of cellular features like relatively small adhesion sites to reveal cell-surface interaction as discussed for the PPX above are not accessible by common light microscopy. High resolution imaging often uses fluorophores but cell clones expressing those fluorophores are elaborate to make and chemical staining of specific cellular features needs to be avoided particularly because the staining process has a major impact onto the properties of features in this size range and staining usually occurs uniform. An alternative way to gain visual contrast without specimen treatment was developed using X-ray holography. X-rays are capable to intrinsic material contrast for biological material in the water window. The main contribution of this work was the preparation of structural preserved cell samples and subsequent visible light microscopy to correlate structural features with the X-ray microscopy images. Establishment of an optimized preparation protocol was a major task as ultrahigh vacuum condition is a prerequisite for this X-ray technique. During the conjoint work two different techniques were applied and first results showed that this technique is capable of higher resolution imaging. Especially the very recent approach using zone plates to generate a divergent wave turned out to be promising by achieving resolution below 350nm. Still, the technique is under development and especially the quality of the beam from synchrotron and free electron lasers are not high enough to access higher resolution regions. Anyhow, the progresses are promisingly fast and the adaption of cryo-prepared samples for imaging in the water window may lead to strong improvement in sample and image quality to reach the final goal of imaging ultrastructural features for cell adhesion with X-ray holography.

Concluding, in this work a sophisticated microfluidic concept was designed, build and established which is capable to probe a number of cellular properties with a high accuracy, reproducibility and throughput on a large variety of surfaces quantitatively. The results comprise significant findings for a better understanding of the interactions between cells and man made surfaces.



# 11 Appendix

## 11.1 List of Parameters

$\alpha$	opening angle	$E_B$	binding energy
$\gamma_{XY}$	surface tension	$E_e$	electron energy
$\gamma$	tilting angle	$E_{kin}$	kinetic energy
$\delta$	spatial resolution	$F$	force
$\Delta$	change in phase shift	$F_t$	tethering force
$\phi$	surface contact fraction	$g$	gravitational acceleration
$\lambda_{att}$	attenuation length	$h$	channel height
$\lambda$	wavelength	$I$	intensity
$\mu$	viscosity	$I_0$	initial intensity
$\omega$	angular rotor speed	$k$	spring constant
$\theta_Y$	Young contact angle	$l$	channel length
$\theta_W$	Wenzel contact angle	$L_e$	flow developmental length
$\theta_{CB}$	Cassie Baxter contact angle	$m_e$	electron mass
$\theta$	takeoff angle	$n$	refractive index
$\rho$	material density	$N$	number of molecules
$\rho_{surface}$	molecule surface density	$NA$	numerical aperture
$\sigma$	surface normal stress	$p$	momentum
$\tau$	shear stress	$Q$	Volume flow
$\tau_{50}$	critical shear stress	$r$	ratio of reflection coefficients
$\psi$	amplitude ratio of p, s	$r_s, r_p$	reflection coefficients
$\psi_{XPS}$	instrument work function	$R$	distance to rotational center
$A$	surface area	$R_e$	Reynolds number
$A_{eff}$	effective surface area	$R_s$	sphere radius
$c$	material concentration	$RCF$	relative centrifugal force
$d_r$	radial distance	$V$	volume
$d_{ia}$	sphere diameter	$w$	channel width
$D$	binding distance	$x$	displacement
$\epsilon$	material adsorption coefficient	$z$	surface roughness ratio

## 11.2 Name Abbreviations

AA	Alginic Acid
AFM	Atomic force microscope
BE	Backscattered Electrons
CVD	Chemical Vapor Deposition
DIC	Differential Interference Contrast
ECM	Extra Cellular Matrix
EDX	Energy Dispersive X-ray
EG	Ethylene Glycol
FCS	Fluorescence Correlation Spectroscopy
FLASH	Free electron LASer in Hamburg
HA	Hyaluronic Acid
HPC	Hematopoietic Stem Cell
LSC	Leukemic Stem Cell
PA	Pectinic Acid
PEG	Poly Ethylene Glycol
PBS	Phosphate Buffered Saline
Ph	Phase contrast
PPX	anisotropically nanotextured poly( <i>p</i> -xylylene)
PSGL-1	P-Selectin Glycoprotein Ligand-1
RGD	Amino acid sequence of Arg-Gly-Asp
SAM	Self Assembled Monolayer
LiTaO <sub>3</sub>	Lithium Tantalite
SD	Standard Deviation
SE	Secondary Electrons
SEM	Scanning Electron Microscope
VLA-4	Very Late Antigen 4
WDX	Wavelength Dispersive X-ray
X-SAM	Self Assembled Monolayer of Alkanethiol X (see 11.3)
XPS	X-ray Photoelectron Spectroscopy

### 11.3 Chemicals & Reagents

Abbreviation	Full name	Details	Company
<b>Alkanethiols</b>			
AUDT	11-Aminoundecanethiol	HS-(CH <sub>2</sub> ) <sub>11</sub> NH <sub>2</sub>	Sigma-Aldrich, Munich, Germany
C12	1-Dodecanethiol	HS-(CH <sub>2</sub> ) <sub>11</sub> -CH <sub>3</sub>	Sigma-Aldrich, Munich, Germany
EG1OH	Hydroxy(ethyleneglycol)-undecanethiolate	HS-(CH <sub>2</sub> ) <sub>11</sub> (OC <sub>2</sub> H <sub>4</sub> )OH	Prochimia Surfaces, Sopot, Poland
EG2OH	Hydroxyl-di(ethyleneglycol)-undecanethiolate	HS-(CH <sub>2</sub> ) <sub>11</sub> (OC <sub>2</sub> H <sub>4</sub> ) <sub>2</sub> OH	Prochimia Surfaces, Sopot, Poland
EG3OH	Hydroxyl-tri(ethyleneglycol)-undecanethiolate	HS-(CH <sub>2</sub> ) <sub>11</sub> (OC <sub>2</sub> H <sub>4</sub> ) <sub>3</sub> OH	Prochimia Surfaces, Sopot, Poland
EG4OH	Hydroxyl-tetra(ethyleneglycol)-undecanethiolate	HS-(CH <sub>2</sub> ) <sub>11</sub> (OC <sub>2</sub> H <sub>4</sub> ) <sub>4</sub> OH	Prochimia Surfaces, Sopot, Poland
EG5OH	Hydroxyl-penta(ethyleneglycol) -undecanethiolate	HS-(CH <sub>2</sub> ) <sub>11</sub> (OC <sub>2</sub> H <sub>4</sub> ) <sub>5</sub> OH	Prochimia Surfaces, Sopot, Poland
EG6OH	Hydroxyl-hexa(ethyleneglycol)-undecanethiolate	HS-(CH <sub>2</sub> ) <sub>11</sub> (OC <sub>2</sub> H <sub>4</sub> ) <sub>6</sub> OH	Prochimia Surfaces, Sopot, Poland
<b>Coupling reagents</b>			
AA	Alginate sodium salt from brown algae	Kat. No. 05550	Sigma-Aldrich, Munich, Germany
APTES	3-Aminopropyltriethoxysilane	H <sub>2</sub> N(CH <sub>2</sub> ) <sub>3</sub> Si(OC <sub>2</sub> H <sub>5</sub> ) <sub>3</sub>	Sigma-Aldrich, Munich, Germany
---	Dichloro-(2,2)-paracyclophane	(Cl <sub>2</sub> C <sub>6</sub> H <sub>6</sub> (CH <sub>2</sub> ) <sub>2</sub> ) <sub>2</sub>	Uniglobe-Kisco, NY, USA
EDC	<i>N</i> -(3-dimethylaminopropyl) - <i>N'</i> -ethylcarbodiimide hydrochloride	C <sub>8</sub> H <sub>17</sub> N <sub>3</sub> HCl	Sigma-Aldrich, Munich, Germany
HA	Hyaluronic acid sodium salt from <i>streptococcus equi</i>	Kat. No. 53747 (M = 1,63x10 <sup>6</sup> Da)	Sigma-Aldrich, Munich, Germany
NHS	N-Hydroxysuccinimide	C <sub>4</sub> H <sub>5</sub> NO <sub>3</sub>	Sigma-Aldrich, Munich, Germany
NHS-biotin	NHS activated biotin	Kat. No. H1759	Sigma-Aldrich, Munich, Germany
---	Styrylethyltrimethoxysilane	(H <sub>3</sub> CO) <sub>3</sub> SiC <sub>2</sub> H <sub>4</sub> C <sub>6</sub> H <sub>6</sub> C <sub>2</sub> H <sub>3</sub>	Gelest, Morrisville, PA, USA

Abbreviation	Full name	Details	Company
<b>Solvents</b>			
DMF	<i>N-N</i> -Dimethylformamide	HCON(CH <sub>3</sub> ) <sub>2</sub>	Sigma-Aldrich, Munich, Germany
EtOH	Ethanol absolute 99.9 %	C <sub>2</sub> H <sub>5</sub> OH	Sigma-Aldrich, Munich, Germany
i-propanol	2-Propanol 99.9 %	C <sub>3</sub> H <sub>7</sub> OH	Sigma-Aldrich, Munich, Germany
2% Extran	30 % alkaline Extran, diluted with Milli-Q water	Aqueous detergens	Merck KGaA, Darmstadt, Germany
HEPES	4-(2-Hydroxyethyl)piperazine-1- ethanesulfonic acid	C <sub>8</sub> H <sub>18</sub> N <sub>2</sub> O <sub>4</sub> S	Sigma-Aldrich, Munich, Germany
Milli-Q water	Deionized water filtered by a Milli- Q plus filter system	H <sub>2</sub> O	Millipore, Schwalbach, Germany
PBS	Phosphate buffered saline pH 7.4 (tablets dissolved in MilliQ)	Kat. No. 18912	Invitrogen, Karlsruhe, Germany
<b>Proteins and cell culture reagents</b>			
BSA	Bovine serum albumin	Kat. No. A7030	Sigma-Aldrich, Munich, Germany
DMEM	Dulbecco's Modified Eagle Medium, high glucose	Kat. No. 10938	Invitrogen, Karlsruhe, Germany
FBS	Fetal bovine serum	Kat. No. 16170	Invitrogen, Karlsruhe, Germany
fibrinogen	Fibrinogen from bovine plasma Type I-S, 65-85 % protein	Kat. No. F8630	Sigma-Aldrich, Munich, Germany
---	L-glutamine	Kat. No. 25030	Invitrogen, Karlsruhe, Germany
LTBMC	Long Term Bone Marrow Culture	self mixed medium	University of Heidelberg
PenStrep	Penicillin/streptomycin	Kat. No. 15140	Invitrogen, Karlsruhe, Germany
PFA	Paraformaldehyde	HO(CH <sub>2</sub> O) <sub>n</sub> H	Sigma-Aldrich, Munich, Germany
RPMI	Roswell Park Memorial Institute Media 1640	Kat. No. 31870	Invitrogen, Karlsruhe, Germany
Trypsin/ EDTA	0.05 % Trypsin-EDTA solution	Kat. No. 25300	Invitrogen, Karlsruhe, Germany

## 11.4 Materials

Name	Description	Company
Nexterion®	ultraflat polished, clean room float glass	Schott AG, Mainz, Germany
PS-spheres	Polystyrene microspheres, 10 µm	Polysciences, Eppelheim, Germany
Strepta-spheres	Streptavidin coated microspheres, 6 µm	Polysciences, Eppelheim, Germany
PDMS	poly-dimethoxysiloxane, elastomer and curing agent Sylgard 184	Dow Corning, MI, USA
EasyFlasks™	tissue culture flasks 25 cm <sup>2</sup>	Nunc, Langensfeld, Germany
UV-bulb	amalgam lamp NIQ 40/18	Heraeus, Hanau, Germany
Pattex	Powerkleber Repair Extreme	Henkel, Düsseldorf, Germany
SiN-Membrane	Silicon Nitride (Si <sub>3</sub> N <sub>4</sub> ) window on a rigid support	Silson Ltd, Northampton, England
PMMA	poly(methyl methacrylate), bulk material	---
gas metering valve	back regulated precision gas pressure valve	Pressluft Götz, Mannheim, Germany
heating cable	teflon covered and metal meshwork protected 3 mm wire	Fritz-Schwarz GmbH, Schwabach, Germany
Medium Reservoir	screw cap, GL 45, 4 port and DURAN® - pressure plus	Schott, Mainz, Germany
Luer Lock Adapter	Upchurch LuerTight (P-836 & P-836)	IDEX Health & Science LLC, Oak Harbor, USA
Multifold	Upchurch 7-Port (P-150)	IDEX Health & Science LLC, Oak Harbor, USA
Selection Valve	Valco Cheminert C25-3186	VICI AG, Schenkoon, Switzerland
PFA tubing	1/16" OD, 0.04" ID	VICI AG, Schenkoon, Switzerland
Pump-Syringe	60 mL Luer Lock, silicon rubber stamp	Becton Dickinson, Heidelberg, Germany
T-connector	2-way and 3-way Luer Lock connection	Neolab, Heidelberg, Germany

## 11.5 Bibliography

- [1] A. Rosenhahn, T. Ederth and M. E. Pettitt (2008). "Advanced Nanostructures for the Control of Biofouling: The Fp6 Eu Integrated Project Ambio." *Biointerphases* **3** (1): IR1-IR5.
- [2] A. J. Engler, M. A. Griffin, S. Sen, C. G. Bonnetmann, H. L. Sweeney and D. E. Discher (2004). "Myotubes Differentiate Optimally on Substrates with Tissue-Like Stiffness: Pathological Implications for Soft or Stiff Microenvironments." *Journal of Cell Biology* **166** (6): 877-887.
- [3] D. E. Discher, P. Janmey and Y. L. Wang (2005). "Tissue Cells Feel and Respond to the Stiffness of Their Substrate." *Science* **310** (5751): 1139-1143.
- [4] R. J. Pelham and Y. L. Wang (1997). "Cell Locomotion and Focal Adhesions Are Regulated by Substrate Flexibility." *Proceedings of the National Academy of Sciences of the United States of America* **94** (25): 13661-13665.
- [5] J. Solon, I. Levental, K. Sengupta, P. C. Georges and P. A. Janmey (2007). "Fibroblast Adaptation and Stiffness Matching to Soft Elastic Substrates." *Biophysical Journal* **93** (12): 4453-4461.
- [6] R. Mcbeath, D. M. Pirone, C. M. Nelson, K. Bhadriraju and C. S. Chen (2004). "Cell Shape, Cytoskeletal Tension, and Rhoa Regulate Stem Cell Lineage Commitment." *Developmental Cell* **6** (4): 483-495.
- [7] M. Arnold, E. A. Cavalcanti-Adam, R. Glass, J. Blummel, W. Eck, M. Kantelehner, et al. (2004). "Activation of Integrin Function by Nanopatterned Adhesive Interfaces." *Chemphyschem* **5** (3): 383-388.
- [8] E. A. Cavalcanti-Adam, T. Volberg, A. Micoulet, H. Kessler, B. Geiger and J. P. Spatz (2007). "Cell Spreading and Focal Adhesion Dynamics Are Regulated by Spacing of Integrin Ligands." *Biophysical Journal* **92** (8): 2964-2974.
- [9] C. S. Chen, M. Mrksich, S. Huang, G. M. Whitesides and D. E. Ingber (1997). "Geometric Control of Cell Life and Death." *Science* **276** (5317): 1425-1428.
- [10] B. Alberts (2008). *Molecular Biology of the Cell*. New York, Garland Science Taylor & Francis.
- [11] E. Ruoslahti (1996). "Rgd and Other Recognition Sequences for Integrins." *Annual Review of Cell and Developmental Biology* **12**: 697-715.
- [12] E. Zamir and B. Geiger (2001). "Molecular Complexity and Dynamics of Cell-Matrix Adhesions." *Journal of Cell Science* **114** (20): 3583-3590.

- 
- [13] N. A. Campbell (2000). *Biologie*. Heidelberg, Spektrum Akademischer Verlag GmbH. **2**: 1440.
- [14] B. M. Gumbiner (1996). "Cell Adhesion: The Molecular Basis of Tissue Architecture and Morphogenesis." *Cell* **84** (3): 345-357.
- [15] D. R. Critchley (2000). "Focal Adhesions - the Cytoskeletal Connection." *Current Opinion in Cell Biology* **12** (1): 133-139.
- [16] M. Cohen, D. Joester, B. Geiger and L. Addadi (2004). "Spatial and Temporal Sequence of Events in Cell Adhesion: From Molecular Recognition to Focal Adhesion Assembly." *Chembiochem* **5** (10): 1393-1399.
- [17] R. Zaidel-Bar, M. Cohen, L. Addadi and B. Geiger (2004). "Hierarchical Assembly of Cell-Matrix Adhesion Complexes." *Biochemical Society Transactions* **32**: 416-420.
- [18] R. P. McEver and R. D. Cummings (1997). "Role of Psgl-1 Binding to Selectins in Leukocyte Recruitment." *Journal of Clinical Investigation* **100** (3): 485-492.
- [19] R. Alon, D. A. Hammer and T. A. Springer (1995). "Lifetime of the P-Selectin-Carbohydrate Bond and Its Response to Tensile Force in Hydrodynamic Flow." *Nature* **374** (6522): 539-542.
- [20] E. B. Finger, K. D. Puri, R. Alon, M. B. Lawrence, U. H. Vonandrian and T. A. Springer (1996). "Adhesion through L-Selectin Requires a Threshold Hydrodynamic Shear." *Nature* **379** (6562): 266-269.
- [21] M. B. Lawrence, G. S. Kansas, E. J. Kunkel and K. Ley (1997). "Threshold Levels of Fluid Shear Promote Leukocyte Adhesion through Selectins (Cd62L,P,E)." *Journal of Cell Biology* **136** (3): 717-727.
- [22] B. T. Marshall, M. Long, J. W. Piper, T. Yago, R. P. McEver and C. Zhu (2003). "Direct Observation of Catch Bonds Involving Cell-Adhesion Molecules." *Nature* **423** (6936): 190-193.
- [23] T. Yago, V. I. Zarnitsyna, A. G. Klopocki, R. P. McEver and C. Zhu (2007). "Transport Governs Flow-Enhanced Cell Tethering through L-Selectin at Threshold Shear." *Biophysical Journal* **92** (1): 330-342.
- [24] C. Berlin, R. F. Bargatze, J. J. Campbell, U. H. Vonandrian, M. C. Szabo, S. R. Hasslen, et al. (1995). "Alpha-4 Integrins Mediate Lymphocyte Attachment and Rolling under Physiological Flow." *Cell* **80** (3): 413-422.
- [25] P. Vajkoczy, M. Laschinger and B. Engelhardt (2001). "Alpha 4-Integrin-Vcam-1 Binding Mediates G Protein - Independent Capture of Encephalitogenic T Cell Blasts to Cns White Matter Microvessels." *Journal of Clinical Investigation* **108** (4): 557-565.

- [26] S. M. Kerfoot and P. Kubes (2002). "Overlapping Roles of P-Selectin and Alpha 4 Integrin to Recruit Leukocytes to the Central Nervous System in Experimental Autoimmune Encephalomyelitis." *Journal of Immunology* **169** (2): 1000-1006.
- [27] C. E. Orsello, D. A. Lauffenburger and D. A. Hammer (2001). "Molecular Properties in Cell Adhesion: A Physical and Engineering Perspective." *Trends in Biotechnology* **19** (8): 310-316.
- [28] A. Rosenhahn, S. Schilp, H. J. Kreuzer and M. Grunze (2010). "The Role Of "Inert" Surface Chemistry in Marine Biofouling Prevention." *Physical Chemistry Chemical Physics* **12** (17): 4275-4286.
- [29] J. H. Lee, J. Kopecek and J. D. Andrade (1989). "Protein-Resistant Surfaces Prepared by PEO-Containing Block Copolymer Surfactants." *Journal of Biomedical Materials Research* **23** (3): 351-368.
- [30] S. I. Jeon, J. H. Lee, J. D. Andrade and P. G. Degennes (1991). "Protein Surface Interactions in the Presence of Polyethylene Oxide. 1. Simplified Theory." *Journal of Colloid and Interface Science* **142** (1): 149-158.
- [31] C. S. Gudipati, J. A. Finlay, J. A. Callow, M. E. Callow and K. L. Wooley (2005). "The Antifouling and Fouling-Release Performance of Hyperbranched Fluoropolymer (Hbfp)-Poly(Ethylene Glycol) (Peg) Composite Coatings Evaluated by Adsorption of Biomacromolecules and the Green Fouling Alga *Ulva*." *Langmuir* **21** (7): 3044-3053.
- [32] S. Krishnan, R. Ayothi, A. Hexemer, J. A. Finlay, K. E. Sohn, R. Perry, et al. (2006). "Anti-Biofouling Properties of Comblike Block Copolymers with Amphiphilic Side Chains." *Langmuir* **22** (11): 5075-5086.
- [33] S. Krishnan, N. Wang, C. K. Ober, J. A. Finlay, M. E. Callow, J. A. Callow, et al. (2006). "Comparison of the Fouling Release Properties of Hydrophobic Fluorinated and Hydrophilic Pegylated Block Copolymer Surfaces: Attachment Strength of the Diatom *Navicula* and the Green Alga *Ulva*." *Biomacromolecules* **7** (5): 1449-1462.
- [34] A. Statz, J. Finlay, J. Dalsin, M. Callow, J. A. Callow and P. B. Messersmith (2006). "Algal Antifouling and Fouling-Release Properties of Metal Surfaces Coated with a Polymer Inspired by Marine Mussels." *Biofouling* **22** (6): 391-399.
- [35] T. Ekblad, G. Bergstroem, T. Ederth, S. L. Conlan, R. Mutton, A. S. Clare, et al. (2008). "Poly(Ethylene Glycol)-Containing Hydrogel Surfaces for Antifouling Applications in Marine and Freshwater Environments." *Biomacromolecules* **9** (10): 2775-2783.

- [36] K. L. Prime and G. M. Whitesides (1993). "Adsorption of Proteins onto Surfaces Containing End-Attached Oligo(Ethylene Oxide): A Model System Using Self-Assembled Monolayers." *Journal of the American Chemical Society* **115** (23): 10714-10721.
- [37] S. Schilp, A. Rosenhahn, M. E. Pettitt, J. Bowen, M. E. Callow, J. A. Callow, et al. (2009). "Physicochemical Properties of (Ethylene Glycol)-Containing Self-Assembled Monolayers Relevant for Protein and Algal Cell Resistance." *Langmuir* **25** (17): 10077-10082.
- [38] E. Ostuni, R. G. Chapman, M. N. Liang, G. Meluleni, G. Pier, D. E. Ingber, et al. (2001). "Self-Assembled Monolayers That Resist the Adsorption of Proteins and the Adhesion of Bacterial and Mammalian Cells." *Langmuir* **17** (20): 6336-6343.
- [39] R. L. C. Wang, H. J. Kreuzer and M. Grunze (1997). "Molecular Conformation and Solvation of Oligo(Ethylene Glycol)-Terminated Self-Assembled Monolayers and Their Resistance to Protein Adsorption." *Journal of Physical Chemistry B* **101** (47): 9767-9773.
- [40] R. L. C. Wang, H. J. Kreuzer and M. Grunze (2000). "The Interaction of Oligo(Ethylene Oxide) with Water: A Quantum Mechanical Study." *Physical Chemistry Chemical Physics* **2** (16): 3613-3622.
- [41] H. J. Kreuzer and M. Grunze (2001). "Stretching of Single Polymer Strands: A First-Principles Theory." *Europhysics Letters* **55** (5): 640-646.
- [42] P. Harder, M. Grunze, R. Dahint, G. M. Whitesides and P. E. Laibinis (1998). "Molecular Conformation in Oligo(Ethylene Glycol)-Terminated Self-Assembled Monolayers on Gold and Silver Surfaces Determines Their Ability to Resist Protein Adsorption." *Journal of Physical Chemistry B* **102** (2): 426-436.
- [43] A. J. Pertsin, T. Hayashi and M. Grunze (2002). "Grand Canonical Monte Carlo Simulations of the Hydration Interaction between Oligo(Ethylene Glycol)-Terminated Alkanethiol Self-Assembled Monolayers." *Journal of Physical Chemistry B* **106** (47): 12274-12281.
- [44] J. Israelachvili and H. Wennerstrom (1996). "Role of Hydration and Water Structure in Biological and Colloidal Interactions." *Nature* **379** (6562): 219-225.
- [45] M. Cohen, E. Klein, B. Geiger and L. Addadi (2003). "Organization and Adhesive Properties of the Hyaluronan Pericellular Coat of Chondrocytes and Epithelial Cells." *Biophysical Journal* **85** (3): 1996-2005.
- [46] M. Morra (2005). "Engineering of Biomaterials Surfaces by Hyaluronan." *Biomacromolecules* **6** (3): 1205-1223.

- [47] M. Morra and C. Cassinelli (1999). "Non-Fouling Properties of Polysaccharide-Coated Surfaces." *Journal of Biomaterials Science-Polymer Edition* **10** (10): 1107-1124.
- [48] M. Morra and C. Cassinelli (1999). "Surface Studies on a Model Cell-Resistant System." *Langmuir* **15** (13): 4658-4663.
- [49] X. Y. Cao, M. E. Pettit, S. L. Conlan, W. Wagner, A. D. Ho, A. S. Clare, et al. (2009). "Resistance of Polysaccharide Coatings to Proteins, Hematopoietic Cells, and Marine Organisms." *Biomacromolecules* **10** (4): 907-915.
- [50] A. Chilkoti, P. H. Tan and P. S. Stayton (1995). "Site-Directed Mutagenesis Studies of the High-Affinity Streptavidin-Biotin Complex - Contributions of Tryptophan Residue-79, Residue-108, and Residue-120." *Proceedings of the National Academy of Sciences of the United States of America* **92** (5): 1754-1758.
- [51] R. Merkel, P. Nassoy, A. Leung, K. Ritchie and E. Evans (1999). "Energy Landscapes of Receptor-Ligand Bonds Explored with Dynamic Force Spectroscopy." *Nature* **397** (6714): 50-53.
- [52] F. Pincet and J. Husson (2005). "The Solution to the Streptavidin-Biotin Paradox: The Influence of History on the Strength of Single Molecular Bonds." *Biophysical Journal* **89** (6): 4374-4381.
- [53] Y. S. Lo, Y. J. Zhu and T. P. Beebe (2001). "Loading-Rate Dependence of Individual Ligand-Receptor Bond-Rupture Forces Studied by Atomic Force Microscopy." *Langmuir* **17** (12): 3741-3748.
- [54] Y. S. Lo, J. Simons and T. P. Beebe (2002). "Temperature Dependence of the Biotin-Avidin Bond-Rupture Force Studied by Atomic Force Microscopy." *Journal of Physical Chemistry B* **106** (38): 9847-9852.
- [55] L. M. Calvi, G. B. Adams, K. W. Weibrecht, J. M. Weber, D. P. Olson, M. C. Knight, et al. (2003). "Osteoblastic Cells Regulate the Haematopoietic Stem Cell Niche." *Nature* **425** (6960): 841-846.
- [56] A. Wilson and A. Trumpp (2006). "Bone-Marrow Haematopoietic-Stem-Cell Niches." *Nat Rev Immunol* **6** (2): 93-106.
- [57] D. Jiang, J. Liang and P. W. Noble (2007). "Hyaluronan in Tissue Injury and Repair." *Annual Review of Cell and Developmental Biology* **23**: 435-461.
- [58] B. Pessac and V. Defendi (1972). "Cell Aggregation: Role of Acid Mucopolysaccharides." *Science* **175**: 898-900.

- [59] S. P. Evanko, J. C. Angello and T. N. Wight (1999). "Formation of Hyaluronan- and Versican-Rich Pericellular Matrix Is Required for Proliferation and Migration of Vascular Smooth Muscle Cells." *Arteriosclerosis Thrombosis and Vascular Biology* **19** (4): 1004-1013.
- [60] A. Aruffo, I. Stamenkovic, M. Melnick, C. B. Underhill and B. Seed (1990). "Cd44 Is the Principal Cell Surface Receptor for Hyaluronate." *Cell* **61**: 1303-1313.
- [61] C. M. Isacke and H. Yarwood (2002). "The Hyaluronan Receptor, Cd44." *The International Journal of Biochemistry & Cell Biology* **34**: 718-721.
- [62] J. Lesley, R. Hyman and P. W. Kincade (1993). "Cd44 and Its Interaction with Extracellular Matrix." *Adv. Immunol.* **54**: 271-335.
- [63] J. Bajorath, B. Greenfield, S. B. Munro, A. J. Day and A. Aruffo (1998). "Identification of Cd44 Residues Important for Hyaluronan Binding and Delineation of the Binding Site." *Journal of Biological Chemistry* **273**: 338-343.
- [64] J. Lesley, N. English, V. C. Hascall, M. Tammi and R. Hyman (2002). *Hyaluronan Binding by Cell Surface Cd44*. Cambridge, U. K. , Woodhead Publishing Ltd. .
- [65] S. Ghaffari, F. Smadja-Joffe, R. Oostendorp, J. P. Levesque, G. Dougherty, A. Eaves, et al. (1999). "Cd44 Isoforms in Normal and Leukemic Hematopoiesis." *Exp Hematol* **27** (6): 978-993.
- [66] S. Goodison, V. Urquidi and D. Tarin (1999). "Cd44 Cell Adhesion Molecules." *Mol Pathol* **52** (4): 189-196.
- [67] R. Marhaba and M. Zoller (2004). "Cd44 in Cancer Progression: Adhesion, Migration and Growth Regulation." *J Mol Histol* **35** (3): 211-231.
- [68] H. Ponta, L. Sherman and P. Herrlich (2003). "Cd44: From Adhesion Molecules to Signalling Regulators." *Nature Reviews* **4**: 33-45.
- [69] R. A. Clark, R. Alon and T. A. Springer (1996). "Cd44 and Hyaluronan-Dependent Rolling Interactions of Lymphocytes on Tonsillar Stroma." *Journal of Cell Biology* **134** (4): 1075-1087.
- [70] H. C. Degrendele, P. Estess, L. J. Picker and M. H. Siegelman (1996). "Cd44 and Its Ligand Hyaluronate Mediate Rolling under Physiologic Flow: A Novel Lymphocyte-Endothelial Cell Primary Adhesion Pathway." *The Journal of Experimental Medicine* **183** (3): 1119-1130.
- [71] J. Lesley, R. Hyman, N. English, J. B. Catterall and G. A. Turner (1997). "Cd44 in Inflammation and Metastasis." *Glycoconjugate Journal* **14** (5): 611-622.

- [72] A. Nandi, P. Estess and M. Siegelman (2004). "Bimolecular Complex between Rolling and Firm Adhesion Receptors Required for Cell Arrest: Cd44 Association with Vla-4 in T Cell Extravasation." *Immunity* **20** (4): 455-465.
- [73] P. M. Wolny, S. Banerji, C. Gounou, A. R. Brisson, A. J. Day, D. G. Jackson, et al. (2010). "Analysis of Cd44-Hyaluronan Interactions in an Artificial Membrane System Insights into the Distinct Binding Properties of High and Low Molecular Weight Hyaluronan." *Journal of Biological Chemistry* **285** (39): 30170-30180.
- [74] M. H. Siegelman, H. C. Degrendele and P. Estess (1999). "Activation and Interaction of Cd44 and Hyaluronan in Immunological Systems." *Journal of Leukocyte Biology* **66** (2): 315-321.
- [75] M. Milinkovic, J. H. Antin, C. A. Hergueter, C. B. Underhill and R. Sackstein (2004). "Cd44-Hyaluronic Acid Interactions Mediate Shear-Resistant Binding of Lymphocytes to Dermal Endothelium in Acute Cutaneous Gvhd." *Blood* **103** (2): 740-742.
- [76] M. B. Lawrence and T. A. Springer (1991). "Leukocytes Roll on a Selectin at Physiologic Flow Rates: Distinction from and Prerequisite for Adhesion through Integrins." *Cell* **65** (5): 859-873.
- [77] K. Ley, C. Laudanna, M. I. Cybulsky and S. Nourshargh (2007). "Getting to the Site of Inflammation: The Leukocyte Adhesion Cascade Updated." *Nature Reviews Immunology* **7** (9): 678-689.
- [78] L. Jin, K. J. Hope, Q. Zhai, F. Smadja-Joffe and J. E. Dick (2006). "Targeting of Cd44 Eradicates Human Acute Myeloid Leukemic Stem Cells." *Nat Med* **12** (10): 1167-1174.
- [79] A. Avigdor, P. Goichberg, S. Shivtiel, A. Dar, A. Peled, S. Samira, et al. (2004). "Cd44 and Hyaluronic Acid Cooperate with Sdf-1 in the Trafficking of Human Cd34+ Stem/Progenitor Cells to Bone Marrow." *Blood* **103** (8): 2981-2989.
- [80] T. Lapidot, A. Dar and O. Kollet (2005). "How Do Stem Cells Find Their Way Home?" *Blood* **106** (6): 1901-1910.
- [81] W. Barthlott and C. Neinhuis (1997). "Purity of the Sacred Lotus, or Escape from Contamination in Biological Surfaces." *Planta* **202** (1): 1-8.
- [82] Sto-Ag. (2011). from <http://www.lotusan.de/>.
- [83] A. J. Scardino and R. De Nys (2011). "Mini Review: Biomimetic Models and Bioinspired Surfaces for Fouling Control." *Biofouling* **27** (1): 73-86.
- [84] P. Ball (1999). "Engineering - Shark Skin and Other Solutions." *Nature* **400** (6744): 507-+.

- [85] M. L. Carman, T. G. Estes, A. W. Feinberg, J. F. Schumacher, W. Wilkerson, L. H. Wilson, et al. (2006). "Engineered Antifouling Microtopographies - Correlating Wettability with Cell Attachment." *Biofouling* **22** (1): 11-21.
- [86] J. F. Schumacher, M. L. Carman, T. G. Estes, A. W. Feinberg, L. H. Wilson, M. E. Callow, et al. (2007). "Engineered Antifouling Microtopographies - Effect of Feature Size, Geometry, and Roughness on Settlement of Zoospores of the Green Alga *Ulva*." *Biofouling* **23** (1): 55-62.
- [87] J. F. Schumacher, N. Aldred, M. E. Callow, J. A. Finlay, J. A. Callow, A. S. Clare, et al. (2007). "Species-Specific Engineered Antifouling Topographies: Correlations between the Settlement of Algal Zoospores and Barnacle Cyprids." *Biofouling* **23** (5): 307-317.
- [88] J. F. Schumacher, C. J. Long, M. E. Callow, J. A. Finlay, J. A. Callow and A. B. Brennan (2008). "Engineered Nanoforce Gradients for Inhibition of Settlement (Attachment) of Swimming Algal Spores." *Langmuir* **24** (9): 4931-4937.
- [89] Y. M. Zheng, X. F. Gao and L. Jiang (2007). "Directional Adhesion of Superhydrophobic Butterfly Wings." *Soft Matter* **3** (2): 178-182.
- [90] N. A. Malvadkar, M. J. Hancock, K. Sekeroglu, W. J. Dressick and M. C. Demirel (2010). "An Engineered Anisotropic Nanofilm with Unidirectional Wetting Properties." *Nature Materials* **9** (12): 1023-1028.
- [91] E. So, M. C. Demirel and K. J. Wahl (2010). "Mechanical Anisotropy of Nanostructured Parylene Films During Sliding Contact." *Journal of Physics D-Applied Physics* **43** (4): 10.
- [92] Y. Tian, N. Pesika, H. B. Zeng, K. Rosenberg, B. X. Zhao, P. McGuiggan, et al. (2006). "Adhesion and Friction in Gecko Toe Attachment and Detachment." *Proceedings of the National Academy of Sciences of the United States of America* **103** (51): 19320-19325.
- [93] A. Mahdavi, L. Ferreira, C. Sundback, J. W. Nichol, E. P. Chan, D. J. D. Carter, et al. (2008). "A Biodegradable and Biocompatible Gecko-Inspired Tissue Adhesive." *Proceedings of the National Academy of Sciences of the United States of America* **105** (7): 2307-2312.
- [94] L. K. Ista, M. E. Callow, J. A. Finlay, S. E. Coleman, A. C. Nolasco, R. H. Simons, et al. (2004). "Effect of Substratum Surface Chemistry and Surface Energy on Attachment of Marine Bacteria and Algal Spores." *Applied and Environmental Microbiology* **70** (7): 4151-4157.
- [95] E. Ostuni, R. G. Chapman, R. E. Holmlin, S. Takayama and G. M. Whitesides (2001). "A Survey of Structure-Property Relationships of Surfaces That Resist the Adsorption of Protein." *Langmuir* **17** (18): 5605-5620.

- [96] A. Rosenhahn, J. A. Finlay, M. E. Pettit, A. Ward, W. Wirges, R. Gerhard, et al. (2009). "Zeta Potential of Motile Spores of the Green Alga *Ulva Linza* and the Influence of Electrostatic Interactions on Spore Settlement and Adhesion Strength." *Biointerphases* **4** (1): 7-11.
- [97] H. J. Kreuzer, R. L. C. Wang and M. Grunze (2003). "Hydroxide Ion Adsorption on Self-Assembled Monolayers." *Journal of the American Chemical Society* **125** (27): 8384-8389.
- [98] Y. H. M. Chan, R. Schweiss, C. Werner and M. Grunze (2003). "Electrokinetic Characterization of Oligo- and Poly(Ethylene Glycol)-Terminated Self-Assembled Monolayers on Gold and Glass Surfaces." *Langmuir* **19** (18): 7380-7385.
- [99] G. Schneider, P. Guttman, S. Heim, S. Rehbein, F. Mueller, K. Nagashima, et al. (2010). "Three-Dimensional Cellular Ultrastructure Resolved by X-Ray Microscopy." *Nature Methods* **7** (12): 985-U116.
- [100] D. Shapiro, P. Thibault, T. Beetz, V. Elser, M. Howells, C. Jacobsen, et al. (2005). "Biological Imaging by Soft X-Ray Diffraction Microscopy." *Proceedings of the National Academy of Sciences of the United States of America* **102** (43): 15343-15346.
- [101] H. D. Jiang, C. Y. Song, C. C. Chen, R. Xu, K. S. Raines, B. P. Fahimian, et al. (2010). "Quantitative 3d Imaging of Whole, Unstained Cells by Using X-Ray Diffraction Microscopy." *Proceedings of the National Academy of Sciences of the United States of America* **107** (25): 11234-11239.
- [102] R. Barth (2008). "Digital in-Line X-Ray Holographic Microscopy with Synchrotron Radiation." Institute of Physical Chemistry, University of Heidelberg. **PhD Thesis**.
- [103] H. N. Chapman, A. Barty, M. J. Bogan, S. Boutet, M. Frank, S. P. Hau-Riege, et al. (2006). "Femtosecond Diffractive Imaging with a Soft-X-Ray Free-Electron Laser." *Nature Physics* **2** (12): 839-843.
- [104] G. Genoud, O. Guilbaud, E. Mengotti, S. G. Pettersson, E. Georgiadou, E. Pourtal, et al. (2008). "Xuv Digital in-Line Holography Using High-Order Harmonics." *Applied Physics B-Lasers and Optics* **90** (3-4): 533-538.
- [105] K. V. Christ and K. T. Turner (2010). "Methods to Measure the Strength of Cell Adhesion to Substrates." *Journal of Adhesion Science and Technology* **24** (13-14): 2027-2058.
- [106] L. S. Channavajjala, A. Eidsath and W. C. Saxinger (1997). "A Simple Method for Measurement of Cell-Substrate Attachment Forces: Application to Hiv-1 Tat." *Journal of Cell Science* **110**: 249-256.

- [107] C. D. Reyes and A. J. Garcia (2003). "Engineering Integrin-Specific Surfaces with a Triple-Helical Collagen-Mimetic Peptide." *Journal of Biomedical Materials Research Part A* **65A** (4): 511-523.
- [108] E. Giacomello, J. Neumayer, A. Colombatti and R. Perris (1999). "Centrifugal Assay for Fluorescence-Based Cell Adhesion Adapted to the Analysis of Ex Vivo Cells and Capable of Determining Relative Binding Strengths." *Biotechniques* **26** (4): 758-+.
- [109] D. R. Mcclay, G. M. Wessel and R. B. Marchase (1981). "Intercellular Recognition: Quantitation of Initial Binding Events." *Proceedings of the National Academy of Sciences of the United States of America* **78** (8): 4975-4979.
- [110] L. Y. Koo, D. J. Irvine, A. M. Mayes, D. A. Lauffenburger and L. G. Griffith (2002). "Co-Regulation of Cell Adhesion by Nanoscale Rgd Organization and Mechanical Stimulus." *Journal of Cell Science* **115** (7): 1423-1433.
- [111] M. M. Lotz, C. A. Burdsal, H. P. Erickson and D. R. Mcclay (1989). "Cell-Adhesion to Fibronectin and Tenascin - Quantitative Measurements of Initial Binding and Subsequent Strengthening Response." *Journal of Cell Biology* **109** (4): 1795-1805.
- [112] J. R. Capadona, D. M. Collard and A. J. Garcia (2003). "Fibronectin Adsorption and Cell Adhesion to Mixed Monolayers of Tri(Ethylene Glycol)- and Methyl-Terminated Alkanethiols." *Langmuir* **19** (5): 1847-1852.
- [113] S. M. Cutler and A. J. Garcia (2003). "Engineering Cell Adhesive Surfaces That Direct Integrin Alpha(5)Beta(1) Binding Using a Recombinant Fragment of Fibronectin." *Biomaterials* **24** (10): 1759-1770.
- [114] B. G. Keselowsky, D. M. Collard and A. J. Garcia (2003). "Surface Chemistry Modulates Fibronectin Conformation and Directs Integrin Binding and Specificity to Control Cell Adhesion." *Journal of Biomedical Materials Research Part A* **66A** (2): 247-259.
- [115] G. M. Harbers and K. E. Healy (2005). "The Effect of Ligand Type and Density on Osteoblast Adhesion, Proliferation, and Matrix Mineralization." *Journal of Biomedical Materials Research Part A* **75A** (4): 855-869.
- [116] O. Thoumine and J. J. Meister (2000). "Dynamics of Adhesive Rupture between Fibroblasts and Fibronectin: Microplate Manipulations and Deterministic Model." *European Biophysics Journal with Biophysics Letters* **29** (6): 409-419.
- [117] O. Thoumine, P. Kocian, A. Kottelat and J. J. Meister (2000). "Short-Term Binding of Fibroblasts to Fibronectin: Optical Tweezers Experiments and Probabilistic Analysis." *European Biophysics Journal with Biophysics Letters* **29** (6): 398-408.

- [118] N. Walter, C. Selhuber, H. Kessler and J. P. Spatz (2006). "Cellular Unbinding Forces of Initial Adhesion Processes on Nanopatterned Surfaces Probed with Magnetic Tweezers." *Nano Letters* **6** (3): 398-402.
- [119] C. C. Wu, H. W. Su, C. C. Lee, M. J. Tang and F. C. Su (2005). "Quantitative Measurement of Changes in Adhesion Force Involving Focal Adhesion Kinase During Cell Attachment, Spread, and Migration." *Biochemical and Biophysical Research Communications* **329** (1): 256-265.
- [120] C. Selhuber-Unkel, T. Erdmann, M. Lopez-Garcia, H. Kessler, U. S. Schwarz and J. P. Spatz (2010). "Cell Adhesion Strength Is Controlled by Intermolecular Spacing of Adhesion Receptors." *Biophysical Journal* **98** (4): 543-551.
- [121] G. Bell (1978). "Models for the Specific Adhesion of Cells to Cells." *Science* **200** (4342): 618-627.
- [122] A. Yamamoto, S. Mishima, N. Maruyama and M. Sumita (2000). "Quantitative Evaluation of Cell Attachment to Glass, Polystyrene, and Fibronectin- or Collagen-Coated Polystyrene by Measurement of Cell Adhesive Shear Force and Cell Detachment Energy." *Journal of Biomedical Materials Research* **50** (2): 114-124.
- [123] Y. J. Kim, J. W. Shin, K. D. Park, J. W. Lee, N. Yui, S. A. Park, et al. (2003). "A Study of Compatibility between Cells and Biopolymeric Surfaces through Quantitative Measurements of Adhesive Forces." *Journal of Biomaterials Science-Polymer Edition* **14** (12): 1311-1321.
- [124] C. H. Chang, J. D. Liao, J. J. J. Chen, M. S. Ju and C. C. K. Lin (2006). "Cell Adhesion and Related Phenomena on the Surface-Modified Au-Deposited Nerve Microelectrode Examined by Total Impedance Measurement and Cell Detachment Tests." *Nanotechnology* **17** (10): 2449-2457.
- [125] C. C. Wang, Y. C. Hsu, F. C. Su, S. C. Lu and T. M. Lee (2009). "Effects of Passivation Treatments on Titanium Alloy with Nanometric Scale Roughness and Induced Changes in Fibroblast Initial Adhesion Evaluated by a Cytodetacher." *Journal of Biomedical Materials Research Part A* **88A** (2): 370-383.
- [126] T. A. Horbett, J. J. Waldburger, B. D. Ratner and A. S. Hoffman (1988). "Cell-Adhesion to a Series of Hydrophilic-Hydrophobic Copolymers Studied with a Spinning Disk Apparatus." *Journal of Biomedical Materials Research* **22** (5): 383-404.
- [127] A. J. Garcia, P. Ducheyne and D. Boettiger (1997). "Quantification of Cell Adhesion Using a Spinning Disc Device and Application to Surface-Reactive Materials." *Biomaterials* **18** (16): 1091-1098.

- [128] A. J. Garcia, F. Huber and D. Boettiger (1998). "Force Required to Break Alpha(5)Beta(1) Integrin-Fibronectin Bonds in Intact Adherent Cells Is Sensitive to Integrin Activation State." *Journal of Biological Chemistry* **273** (18): 10988-10993.
- [129] N. D. Gallant, J. R. Capadona, A. B. Frazier, D. M. Collard and A. J. Garcia (2002). "Micropatterned Surfaces to Engineer Focal Adhesions for Analysis of Cell Adhesion Strengthening." *Langmuir* **18** (14): 5579-5584.
- [130] M. H. Lee, C. S. Adams, D. Boettiger, W. F. Degrado, I. M. Shapiro, R. J. Composto, et al. (2007). "Adhesion of Mc3t3-E1 Cells to Rgd Peptides of Different Flanking Residues: Detachment Strength and Correlation with Long-Term Cellular Function." *Journal of Biomedical Materials Research Part A* **81A** (1): 150-160.
- [131] A. J. Garcia, J. Takagi and D. Boettiger (1998). "Two-Stage Activation for Alpha(5)Beta(1) Integrin Binding to Surface-Adsorbed Fibronectin." *Journal of Biological Chemistry* **273** (52): 34710-34715.
- [132] D. D. Deligianni, N. D. Katsala, P. G. Koutsoukos and Y. F. Missirlis (2001). "Effect of Surface Roughness of Hydroxyapatite on Human Bone Marrow Cell Adhesion, Proliferation, Differentiation and Detachment Strength." *Biomaterials* **22** (1): 87-96.
- [133] A. S. Goldstein and P. A. Dimilla (1998). "Comparison of Converging and Diverging Radial Flow for Measuring Cell Adhesion." *Aiche Journal* **44** (2): 465-473.
- [134] A. Rezanian and K. E. Healy (1999). "Integrin Subunits Responsible for Adhesion of Human Osteoblast-Like Cells to Biomimetic Peptide Surfaces." *Journal of Orthopaedic Research* **17** (4): 615-623.
- [135] A. Rezanian and K. E. Healy (1999). "Biomimetic Peptide Surfaces That Regulate Adhesion, Spreading, Cytoskeletal Organization, and Mineralization of the Matrix Deposited by Osteoblast-Like Cells." *Biotechnology Progress* **15** (1): 19-32.
- [136] T. Sordel, F. Kermarec-Marcel, S. Garnier-Raveaud, N. Glade, F. Sauter-Starace, C. Pudda, et al. (2007). "Influence of Glass and Polymer Coatings on Cho Cell Morphology and Adhesion." *Biomaterials* **28** (8): 1572-1584.
- [137] A. S. Goldstein and P. A. Dimilla (2002). "Effect of Adsorbed Fibronectin Concentration on Cell Adhesion and Deformation under Shear on Hydrophobic Surfaces." *Journal of Biomedical Materials Research* **59** (4): 665-675.
- [138] G. A. Truskey and J. S. Pirone (1990). "The Effect of Fluid Shear-Stress Upon Cell-Adhesion to Fibronectin-Treated Surfaces." *Journal of Biomedical Materials Research* **24** (10): 1333-1353.

- [139] T. G. Vankooten, J. M. Schakenraad, H. C. Vandermei and H. J. Busscher (1992). "Development and Use of a Parallel-Plate Flow Chamber for Studying Cellular Adhesion to Solid-Surfaces." *Journal of Biomedical Materials Research* **26** (6): 725-738.
- [140] H. Lu, L. Y. Koo, W. C. M. Wang, D. A. Lauffenburger, L. G. Griffith and K. F. Jensen (2004). "Microfluidic Shear Devices for Quantitative Analysis of Cell Adhesion." *Analytical Chemistry* **76** (18): 5257-5264.
- [141] J. S. Burmeister, J. D. Vraný, W. M. Reichert and G. A. Truskey (1996). "Effect of Fibronectin Amount and Conformation on the Strength of Endothelial Cell Adhesion to Hema/Ema Copolymers." *Journal of Biomedical Materials Research* **30** (1): 13-22.
- [142] Y. Xiao and G. A. Truskey (1996). "Effect of Receptor-Ligand Affinity on the Strength of Endothelial Cell Adhesion." *Biophysical Journal* **71** (5): 2869-2884.
- [143] S. Usami, H. H. Chen, Y. H. Zhao, S. Chien and R. Skalak (1993). "Design and Construction of a Linear Shear-Stress Flow Chamber." *Annals of Biomedical Engineering* **21** (1): 77-83.
- [144] K. Christ, K. Williamson, K. Masters and K. Turner (2010). "Measurement of Single-Cell Adhesion Strength Using a Microfluidic Assay." *Biomedical Microdevices* **12** (3): 443-455.
- [145] J. H. Lee, S. K. Lee, G. Khang and H. B. Lee (2000). "The Effect of Fluid Shear Stress on Endothelial Cell Adhesiveness to Polymer Surfaces with Wettability Gradient." *Journal of Colloid and Interface Science* **230** (1): 84-90.
- [146] Y. Q. Wan, J. Yang, J. L. Yang, J. Z. Bei and S. G. Wang (2003). "Cell Adhesion on Gaseous Plasma Modified Poly-(L-Lactide) Surface under Shear Stress Field." *Biomaterials* **24** (21): 3757-3764.
- [147] R. Kapur and A. S. Rudolph (1998). "Cellular and Cytoskeleton Morphology and Strength of Adhesion of Cells on Self-Assembled Monolayers of Organosilanes." *Experimental Cell Research* **244** (1): 275-285.
- [148] A. Ulman (1996). "Formation and Structure of Self-Assembled Monolayers." *Chemical Reviews* **96** (4): 1533-1554.
- [149] J. C. Love, L. A. Estroff, J. K. Kriebel, R. G. Nuzzo and G. M. Whitesides (2005). "Self-Assembled Monolayers of Thiolates on Metals as a Form of Nanotechnology." *Chemical Reviews* **105** (4): 1103-1169.
- [150] W. Senaratne, L. Andruzzi and C. K. Ober (2005). "Self-Assembled Monolayers and Polymer Brushes in Biotechnology: Current Applications and Future Perspectives." *Biomacromolecules* **6** (5): 2427-2448.

- [151] D. G. Castner and B. D. Ratner (2002). "Biomedical Surface Science: Foundations to Frontiers." *Surface Science* **500** (1-3): 28-60.
- [152] M. E. Callow, J. A. Callow, L. K. Ista, S. E. Coleman, A. C. Nolasco and G. P. Lopez (2000). "Use of Self-Assembled Monolayers of Different Wettabilities to Study Surface Selection and Primary Adhesion Processes of Green Algal (Enteromorpha) Zoospores." *Applied and Environmental Microbiology* **66** (8): 3249-3254.
- [153] S. Krishnan, C. J. Weinman and C. K. Ober (2008). "Advances in Polymers for Anti-Biofouling Surfaces." *Journal of Materials Chemistry* **18** (29): 3405-3413.
- [154] G. Albert (1996). "Herstellung Und Charakterisierung Polykristalliner Goldschichten Zur Verwendung in Der Nanolithographie." Institute of Physical Chemistry, University of Heidelberg. **Master Thesis**.
- [155] S. Schilp, A. Kueller, A. Rosenhahn, M. Grunze, M. E. Pettitt, M. E. Callow, et al. (2007). "Settlement and Adhesion of Algal Cells to Hexa (Ethylene Glycol)-Containing Self-Assembled Monolayers with Systematically Changed Wetting Properties." *Biointerphases* **2** (4): 143-150.
- [156] M. Cetinkaya, S. Boduroglu and M. C. Demirel (2007). "Growth of Nanostructured Thin Films of Poly (P-Xylylene) Derivatives by Vapor Deposition." *Polymer* **48** (14): 4130-4134.
- [157] W. J. Dressick, C. S. Dulcey, J. H. Georger, G. S. Calabrese and J. M. Calvert (1994). "Covalent Binding of Pd Catalysts to Ligating Self-Assembled Monolayer Films for Selective Electroless Metal-Deposition." *Journal of the Electrochemical Society* **141** (1): 210-220.
- [158] M. C. Demirel, S. Boduroglu, M. Cetinkaya and A. Lakhtakia (2007). "Spatially Organized Free-Standing Poly(P-Xylylene) Nanowires Fabricated by Vapor Deposition." *Langmuir* **23** (11): 5861-5863.
- [159] G. R. Meseck (2010). "Wechselwirkung Von Zellen Und Bakterien Mit Immobilisierten Polysacchariden." Institute of Physical Chemistry, University of Heidelberg. **Diploma Thesis**.
- [160] A. Albersdorfer and E. Sackmann (1999). "Swelling Behavior and Viscoelasticity Ultrathin Grafted Hyaluronic Acid Films." *European Physical Journal B* **10** (4): 663-672.
- [161] W. Wang and M. W. Vaughn (2008). "Morphology and Amine Accessibility of (3-Aminopropyl) Triethoxysilane Films on Glass Surfaces." *Scanning* **30** (2): 65-77.
- [162] Z. Grabarek and J. Gergely (1990). "Zero-Length Crosslinking Procedure with the Use of Active Esters." *Analytical Biochemistry* **185** (1): 131-135.

- [163] R. A. Stile, T. A. Barber, D. Castner, G. and K. E. Healy (2002). "Sequential Robust Design Methodology and X-Ray Photoelectron Spectroscopy to Analyze the Grafting of Hyaluronic Acid to Glass Substrates." *Journal of Biomedical Materials Research* **61** (3): 391-398.
- [164] J. H. Scofield (1976). "Hartree-Slater Subshell Photoionization Cross-Sections at 1254 and 1487 Ev." *Journal of Electron Spectroscopy and Related Phenomena* **8** (2): 129-137.
- [165] J. N. Hanson, B. J. Rodriguez, R. J. Nemanich and A. Gruverman (2006). "Fabrication of Metallic Nanowires on a Ferroelectric Template Via Photochemical Reaction." *Nanotechnology* **17** (19): 4946-4949.
- [166] Z. Z. Zhang, P. Sharma, C. N. Borca, P. A. Dowben and A. Gruverman (2010). "Polarization-Specific Adsorption of Organic Molecules on Ferroelectric Linbo3 Surfaces." *Applied Physics Letters* **97** (24).
- [167] A. Gruverman, O. Auciello and H. Tokumoto (1998). "Imaging and Control of Domain Structures in Ferroelectric Thin Films Via Scanning Force Microscopy." *Annual Review of Materials Science* **28**: 101-123.
- [168] W. Wagner, F. Wein, C. Roderburg, R. Saffrich, A. Diehlmann, V. Eckstein, et al. (2008). "Adhesion of Human Hematopoietic Progenitor Cells to Mesenchymal Stromal Cells Involves Cd44." *Cells Tissues Organs* **188** (1-2): 160-169.
- [169] B. R. Franza, Jr., K. Maruyama, J. I. Garrels and H. E. Ruley (1986). "In Vitro Establishment Is Not a Sufficient Prerequisite for Transformation by Activated Ras Oncogenes." *Cell* **44** (3): 409-418.
- [170] E. Zamir, B. Z. Katz, S. Aota, K. M. Yamada, B. Geiger and Z. Kam (1999). "Molecular Diversity of Cell-Matrix Adhesions." *Journal of Cell Science* **112** (11): 1655-1669.
- [171] A. Sigal, R. Milo, A. Cohen, N. Geva-Zatorsky, Y. Klein, I. Alaluf, et al. (2006). "Dynamic Proteomics in Individual Human Cells Uncovers Widespread Cell-Cycle Dependence of Nuclear Proteins." *Nature Methods* **3** (7): 525-531.
- [172] H. P. Koeffler, R. Billing, A. J. Lusic, R. Sparkes and D. W. Golde (1980). "An Undifferentiated Variant Derived from the Human Acute Myelogenous Leukemia Cell Line (Kg-1)." *Blood* **56** (2): 265-273.
- [173] H. P. Koeffler (1983). "Induction of Differentiation of Human Acute Myelogenous Leukemia Cells: Therapeutic Implications." *Blood* **62** (4): 709-721.
- [174] R. Gallagher, S. Collins, J. Trujillo, K. Mccredie, M. Ahearn, S. Tsai, et al. (1979). "Characterization of the Continuous, Differentiating Myeloid Cell Line (HI-60) from a Patient with Acute Promyelocytic Leukemia." *Blood* **54** (3): 713-733.

- [175] H. Koefler and D. Golde (1980). "Human Myeloid Leukemia Cell Lines: A Review." *Blood* **56** (3): 344-350.
- [176] H. Asou, S. Tashiro, K. Hamamoto, A. Otsuji, K. Kita and N. Kamada (1991). "Establishment of a Human Acute Myeloid Leukemia Cell Line (Kasumi-1) with 8;21 Chromosome Translocation." *Blood* **77** (9): 2031-2036.
- [177] A. Weiss, R. L. Wiskocil and J. D. Stobo (1984). "The Role of T3 Surface Molecules in the Activation of Human T Cells: A Two-Stimulus Requirement for IL 2 Production Reflects Events Occurring at a Pre-Translational Level." *J Immunol* **133** (1): 123-128.
- [178] W. Wagner, F. Wein, C. Roderburg, R. Saffrich, A. Faber, U. Krause, et al. (2007). "Adhesion of Hematopoietic Progenitor Cells to Human Mesenchymal Stem Cells as a Model for Cell-Cell Interaction." *Exp Hematol* **35** (2): 314-325.
- [179] T. Young (1805). "An Essay on the Cohesion of Fluids." *Philosophical Transactions of the Royal Society of London* **95**: 65-87.
- [180] R. N. Wenzel (1936). "Resistance of Solid Surfaces to Wetting by Water." *Industrial & Engineering Chemistry* **28** (8): 988-994.
- [181] A. B. D. Cassie and S. Baxter (1944). "Wettability of Porous Surfaces." *Trans. Faraday. Soc* **40**: 546-551.
- [182] H. G. Tompkins (2006). *A User's Guide to Ellipsometry*. San Diego, CA, Academic Press Inc.
- [183] D. A. Shirley (1972). "High-Resolution X-Ray Photoemission Spectrum of the Valence Bands of Gold." *Physical Review B* **5** (12): 4709.
- [184] N. Meyerbröcker (2009). "Elektronenstrahlinduzierte Vernetzung Und Chemische Modifizierung Selbstaggregierender Monoschichten Von 4'-Cyano-1,1'-Biphenylthiol Auf Gold(111)-Oberflächen." Institute of Physical Chemistry, University of Heidelberg. **Diploma Thesis**.
- [185] P. J. Goodhew, J. Humphreys and R. Beanland (2001). *Electron Microscopy and Analysis*. London, Taylor & Francis.
- [186] Y. N. Xia and G. M. Whitesides (1998). "Soft Lithography." *Annual Review of Materials Science* **28**: 153-184.
- [187] T. Vilker, D. Janasek and A. Manz (2004). "Micro Total Analysis Systems. Recent Developments." *Analytical Chemistry* **76** (12): 3373-3385.
- [188] A. Khademhosseini, R. Langer, J. Borenstein and J. P. Vacanti (2006). "Microscale Technologies for Tissue Engineering and Biology." *Proceedings of the National Academy of Sciences of the United States of America* **103** (8): 2480-2487.

- [189] E. W. K. Young and C. A. Simmons (2009). "Macro- and Microscale Fluid Flow Systems for Endothelial Cell Biology." *Lab on a Chip* **10** (2): 143-160.
- [190] J. C. McDonald, D. C. Duffy, J. R. Anderson, D. T. Chiu, H. K. Wu, O. J. A. Schueller, et al. (2000). "Fabrication of Microfluidic Systems in Poly(Dimethylsiloxane)." *Electrophoresis* **21** (1): 27-40.
- [191] S. K. Sia and G. M. Whitesides (2003). "Microfluidic Devices Fabricated in Poly(Dimethylsiloxane) for Biological Studies." *Electrophoresis* **24** (21): 3563-3576.
- [192] D. Huh, W. Gu, Y. Kamotani, J. B. Grotberg and S. Takayama (2005). "Microfluidics for Flow Cytometric Analysis of Cells and Particles." *Physiological Measurement* **26** (3): R73-R98.
- [193] L. Marcotte and A. Tabrizian (2008). "Sensing Surfaces: Challenges in Studying the Cell Adhesion Process and the Cell Adhesion Forces on Biomaterials." *Irbm* **29** (2-3): 77-88.
- [194] C. D. Reyes and A. J. Garcia (2003). "A Centrifugation Cell Adhesion Assay for High-Throughput Screening of Biomaterial Surfaces." *Journal of Biomedical Materials Research Part A* **67A** (1): 328-333.
- [195] K. A. Athanasiou, B. S. Thoma, D. R. Lanctot, D. Shin, C. M. Agrawal and R. G. Lebaron (1999). "Development of the Cytodetachment Technique to Quantify Mechanical Adhesiveness of the Single Cell." *Biomaterials* **20** (23-24): 2405-2415.
- [196] S. F. Li and S. C. Chen (2003). "Polydimethylsiloxane Fluidic Interconnects for Microfluidic Systems." *Ieee Transactions on Advanced Packaging* **26** (3): 242-247.
- [197] E. W. K. Young, A. R. Wheeler and C. A. Simmons (2007). "Matrix-Dependent Adhesion of Vascular and Valvular Endothelial Cells in Microfluidic Channels." *Lab on a Chip* **7**: 1759-1766.
- [198] W. M. Deen (1998). "Analysis of Transport Phenomena." *Oxford University Press, New York*.
- [199] D. P. Gaver and S. M. Kute (1998). "A Theoretical Model Study of the Influence of Fluid Stresses on a Cell Adhering to a Microchannel Wall." *Biophysical Journal* **75** (2): 721-733.
- [200] R. K. Shah, A. L. London and F. M. White (1980). "Laminar Flow Forced Convection in Ducts." *Journal of Fluids Engineering* **102** (2): 256-257.
- [201] (2008/2009). *Crc Handbook of Chemistry and Physics*, CRC Press.
- [202] T. Yago, J. H. Wu, C. D. Wey, A. G. Klopocki, C. Zhu and R. P. McEver (2004). "Catch Bonds Govern Adhesion through L-Selectin at Threshold Shear." *Journal of Cell Biology* **166** (6): 913-923.

- 
- [203] J. Israelachvili (1991). *Intermolecular & Surface Forces*. London, Academic Press.
- [204] W. W. Minuth, R. Strehl and K. Schumacher (2002). *Von Der Zellkultur Zum Tissue Engineering*. Lengerich, Pabst Science Publishers.
- [205] D. Riveline, E. Zamir, N. Q. Balaban, U. S. Schwarz, T. Ishizaki, S. Narumiya, et al. (2001). "Focal Contacts as Mechanosensors: Externally Applied Local Mechanical Force Induces Growth of Focal Contacts by an Mdia1-Dependent and Rock-Independent Mechanism." *Journal of Cell Biology* **153** (6): 1175-1185.
- [206] R. Paul, P. Heil, J. P. Spatz and U. S. Schwarz (2008). "Propagation of Mechanical Stress through the Actin Cytoskeleton toward Focal Adhesions: Model and Experiment." *Biophysical Journal* **94** (4): 1470-1482.
- [207] Y. S. J. Li, J. H. Haga and S. Chien (2005). "Molecular Basis of the Effects of Shear Stress on Vascular Endothelial Cells." *Journal of Biomechanics* **38** (10): 1949-1971.
- [208] C. F. Dewey, Jr., S. R. Bussolari, M. A. Gimbrone, Jr. and P. F. Davies (1981). "The Dynamic Response of Vascular Endothelial Cells to Fluid Shear Stress." *Journal of Biomechanical Engineering* **103** (3): 177-185.
- [209] R. P. Franke, M. Grafe, H. Schnittler, D. Seiffge, C. Mittermayer and D. Drenckhahn (1984). "Induction of Human Vascular Endothelial Stress Fibres by Fluid Shear Stress." *Nature* **307** (5952): 648-649.
- [210] C. G. Galbraith, R. Skalak and S. Chien (1998). "Shear Stress Induces Spatial Reorganization of the Endothelial Cell Cytoskeleton." *Cell Motility and the Cytoskeleton* **40** (4): 317-330.
- [211] M. Masuda and K. Fujiwara (1993). "The Biased Lamellipodium Development and Microtubule-Organizing Center Position in Vascular Endothelial-Cells Migrating under the Influence of Fluid-Flow." *Biology of the Cell* **77** (3): 237-245.
- [212] B. Zhu, T. Eurell, R. Gunawan and D. Leckband (2001). "Chain-Length Dependence of the Protein and Cell Resistance of Oligo(Ethylene Glycol)-Terminated Self-Assembled Monolayers on Gold." *Journal of Biomedical Materials Research* **56** (3): 406-416.
- [213] K. L. Prime and G. M. Whitesides (1993). "Adsorption of Proteins onto Surfaces Containing End-Attached Oligo(Ethylene Oxide) - a Model System Using Self-Assembled Monolayers." *Journal of the American Chemical Society* **115** (23): 10714-10721.

- [214] S. Herrwerth, W. Eck, S. Reinhardt and M. Grunze (2003). "Factors That Determine the Protein Resistance of Oligoether Self-Assembled Monolayers - Internal Hydrophilicity, Terminal Hydrophilicity, and Lateral Packing Density." *Journal of the American Chemical Society* **125** (31): 9359-9366.
- [215] M. P. Arpa-Sancet (2011). "Adhesion Strength of Murine Bacteria *Cobetia Marina* on Self Assembled Monolayers with Tuneable Hydration." Institute of Physical Chemistry, University of Heidelberg. **PhD work in progress.**
- [216] H. Koeffler, R. Billing, A. Lysis, R. Sparkes and D. Golde (1980). "An Undifferentiated Variant Derived from the Human Acute Myelogenous Leukemia Cell Line (Kg-1)." *Blood* **56** (2): 265-273.
- [217] U. Schneider, H.-U. Schwenk and G. Bornkamm (1977). "Characterization of Ebv-Genome Negative "Null" And "T" Cell Lines Derived from Children with Acute Lymphoblastic Leukemia and Leukemic Transformed Non-Hodgkin Lymphoma." *International Journal of Cancer* **19** (5): 621-626.
- [218] C. Zhu, T. Yago, J. Z. Lou, V. I. Zarnitsyna and R. P. McEver (2008). "Mechanisms for Flow-Enhanced Cell Adhesion." *Annals of Biomedical Engineering* **36** (4): 604-621.
- [219] D. G. Jackson (2009). "Immunological Functions of Hyaluronan and Its Receptors in the Lymphatics." *Immunological Reviews* **230**: 216-231.
- [220] R. Hyman, J. Lesley and R. Schulte (1991). "Somatic-Cell Mutants Distinguish Cd44 Expression and Hyaluronic-Acid Binding." *Immunogenetics* **33** (5-6): 392-395.
- [221] A. Avigdor, P. Goichberg, S. Shivtiel, A. Dar, A. Peled, S. Samira, et al. (2004). "Cd44 and Hyaluronic Acid Cooperate with Sdf-1 in the Trafficking of Human Cd34+ Stem/Progenitor Cells to Bone Marrow." *Blood* **103** (8): 2981-2989.
- [222] K. Kitamura, Y. Furukawa, K. Niwa, V. Gopalan and T. E. Mitchell (1998). "Crystal Growth and Low Coercive Field 180 Degrees Domain Switching Characteristics of Stoichiometric Litao3." *Applied Physics Letters* **73** (21): 3073-3075.
- [223] Y. Yun and E. I. Altman (2007). "Using Ferroelectric Poling to Change Adsorption on Oxide Surfaces." *Journal of the American Chemical Society* **129** (50): 15684-15689.
- [224] S. Boduroglu, M. Cetinkaya, W. J. Dressick, A. Singh and M. C. Demirel (2007). "Controlling the Wettability and Adhesion of Nanostructured Poly-(P-Xylylene) Films." *Langmuir* **23** (23): 11391-11395.

- [225] F. Staier (2009). "Entwicklung, Bau Und Test Einer Uhv Röntgenstreuammer Für Die Digitale in-Line Holographie." Institute of Physical Chemistry, Universität Heidelberg. **PhD Thesis**.
- [226] T. Gorniak (2009). "Digitale Röntgenholographie Mit Lochblenden Und Fresnelschen Zonenplatten Bei Bessy Und Flash." Institute of Physical Chemistry, University of Heidelberg. **Diploma Thesis**.
- [227] (2011). "X-Ray Attenuation Length." from [http://henke.lbl.gov/optical\\_constants/atten2.html](http://henke.lbl.gov/optical_constants/atten2.html).

## 11.6 Financial Support

The work described in this thesis was supported by:

- BMBF project 05KS4VH1
- BMBF project 05KS7VH1
- ONR grant N00014-08-1-1116
- 6th framework EU integrated project AMBIO

## 11.7 List of publications related to this work

### Published articles

- A. Rosenhahn, F. Staier, T. Nisius, D. Schafer, R. Barth, C. Christophis, et al. (2009). "Digital in-Line Holography with Femtosecond Vuv Radiation Provided by the Free-Electron Laser Flash." *Optics Express* **17** (10): 8220-8228.
- A. P. Mancuso, T. Gorniak, F. Staler, O. M. Yefanov, R. Barth, C. Christophis, et al. (2010). "Coherent Imaging of Biological Samples with Femtosecond Pulses at the Free-Electron Laser Flash." *New Journal of Physics* **12**: 14.
- C. Christophis, M. Grunze and A. Rosenhahn (2010). "Quantification of the Adhesion Strength of Fibroblast Cells on Ethylene Glycol Terminated Self-Assembled Monolayers by a Microfluidic Shear Force Assay." *Physical Chemistry Chemical Physics* **12** (1-7): 4498-4504.
- R. Heine, T. Gorniak, T. Nisius, C. Christophis, M. E. Pettitt, F. Staier, et al. (2011). "Digital in-Line X-Ray Holography with Zone Plates." *Ultramicroscopy* **In Press**.

### Accepted articles

- C. Christophis, I. Taubert, G. Meseck, M. Schubert, M. Grunze, A. D. Ho and A. Rosenhahn; "Shear stress regulates adhesion and rolling of CD44-expressing leukemic and hematopoietic progenitor cells on hyaluronan"; *Biophysical Journal*, **accepted 2011**.
- T. Gorniak, R. Heine, A. P. Mancuso, F. Staier, C. Christophis, M. E. Pettitt, et al.; "X-ray holographic microscopy with zone plates applied to biological samples in the water window using 3rd harmonic radiation from the free-electron laser FLASH", *Optics Express*, **accepted 2011**.

### Articles in preparation

- C. Christophis, K. Sekeroglu, M. Grunze, A. Rosenhahn and M. C. Demirel; „Fibroblast Adhesion on Microfluidic Devices Coated with Unidirectional Nanofilms”, **in preparation**.
- C. Christophis, P. Dowben, [...], M. Grunze, A. Rosenhahn; „Adherent cells avoid polarization gradients on periodically poled LiTaO<sub>3</sub> ferroelectrics”, **in preparation**.

## Danksagung

Mein großer Dank gilt Prof. Dr. Michael Grunze für die Möglichkeit meine Doktorarbeit in seiner Gruppe anzufertigen und die dadurch resultierende Möglichkeit auch mit vielen Forschern auf internationaler Ebene in Kontakt zu treten.

Auch Prof. Dr. Joachim P. Spatz danke ich ganz herzlich – nicht nur für die Übernahme des Zweit-Gutachtens, sondern auch für die Großzügigkeit, Zellkultur und bestimmte Geräte mitbenutzen zu dürfen.

Ein besonderes Dankeschön gilt Dr. Axel Rosenhahn für die Bereitschaft mich in seinem Labor aufzunehmen und dafür zu sorgen, dass zum Trotz allgegenwertiger administrativer Schikanen mein Konto am Ende des Monats stets aufgefüllt wurde.

An dieser Stelle danke ich den vielfältigen und fruchtbaren Kooperationen:

Prof. Dr. Melik C. Demirel (Pennsylvania State University, USA)

Prof. Dr. Peter A. Dowben (Universität Nebraska, Lincoln, USA)

Prof. Dr. Hans J. Kreuzer (Dalhousie Universität, Halifax, Kanada)

Prof. Dr. Anthony D. Ho und Isabel Taubert (Medizin V, Universität Heidelberg)

Georg R. Meseck (jetzt Universität Zürich, Schweiz)

Dr. Dirk P. Herten und Jessica Balbo (BioQuant, Uni Heidelberg)

Die HORST-Crew, Dr. Ruth Heine, Florian Staier und Thomas Gorniak

Auch danke ich recht herzlich Allen, die mich wissenschaftlich unterstützt haben. Besonders hervorheben möchte ich:

Reinhold Jehle, ohne den die eine oder andere Idee und CAD-Zeichnung so wohl nicht Realität geworden wäre und natürlich die Feinmechanik Werkstatt um Klaus Schmitt bzw. Günter Meinusch, ohne die auch die besten Konstruktionszeichnungen nichts anderes als reine Theorie geblieben wären. Christina Leinweber, Dr. Matthias Heydt, Isabel Thomé, Dr. Marcus Abel, Sigrid Riese und Nikolaus Meyerbröcker danke ich besonders für die fachliche Kommunikation und technische Unterstützung.

Für das Korrekturlesen meiner Arbeit bedanke ich mich bei Christina Leinweber, Sebastian Weiße, Isabel Thomé, Svenja Stuppy, Tobias Senkbeil, Thomas Gorniak, Dr. Ruth Heine und besonders bei Dr. Axel Rosenhahn für die zahlreichen Anregungen.

Der gesamten Arbeitsgruppe Rosenhahn danke ich sehr für die netten Pausen, so manche Grill-Session, die gemütlichen Weihnachtsfeiern und die schöne Zeit hier in Heidelberg. Auch vielen Dank an die gesamte Gruppe von Prof. Grunze und Prof. Spatz für die netten und spontanen Schwätzchen. Danke an das nichtwissenschaftliche Personal - besonders

Benjamin Scherke und Swetlana Duchnay, die es immer geschafft haben administrative Hürden in einem Bruchteil der dafür vorgesehenen Zeit zu überwinden.

Auch sollen hier meine essenziellen Utensilien nicht unerwähnt bleiben: Danke an das Brita® Filter System, die Kaffeemaschine inklusive deren Bediener und Kaffeepulver-Spender und natürlich an die Institutsdusche. Für solide Nahrung danke ich dem Unishop und dem Käse-Brezel-Bäcker.

Zum Schluss danke ich den wichtigsten Menschen - meinen Freunden und meiner Familie. Vielen Dank an meine Eltern, meine Brüder und meine Großeltern für die finanzielle und moralische Unterstützung.

Am meisten aber, haben mich meine langjährigen „Mitbewohner“ unterstützt. Vielen Dank an die „kleinen“ Kätzchen Kata und Foulani und an das „große“ Kätzchen – meine Kerstin. Ohne euch wäre die vergangene Zeit nicht halb so schön gewesen... und die kommende erst recht nicht.